Spring 2004

# Fabrication, characterization, and chemical sensing of silicon dioxide microcantilevers

Yanjun Tang
*Louisiana Tech University*

# FABRICATION, CHARACTERIZATION, AND CHEMICAL

# SENSING OF SILICON DIOXIDE MICROCANTILEVERS

By

Yanjun Tang, B. S.

A Dissertation Presented in Partial Fulfillment of the
Requirements for the Degree of
Doctor of Philosophy in Engineering

COLLEGE OF ENGINEERING AND SCIENCE
LOUISIANA TECH UNIVERSITY

May 2004

UMI Number: 3126552

INFORMATION TO USERS

The quality of this reproduction is dependent upon the quality of the copy
submitted. Broken or indistinct print, colored or poor quality illustrations and
photographs, print bleed-through, substandard margins, and improper
alignment can adversely affect reproduction.

In the unlikely event that the author did not send a complete manuscript
and there are missing pages, these will be noted. Also, if unauthorized
copyright material had to be removed, a note will indicate the deletion.

# UMI®

UMI Microform 3126552

Copyright 2004 by ProQuest Information and Learning Company.

All rights reserved. This microform edition is protected against
unauthorized copying under Title 17, United States Code.

ProQuest Information and Learning Company
300 North Zeeb Road
P.O. Box 1346
Ann Arbor, MI 48106-1346
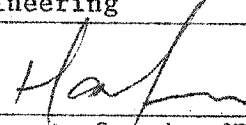
# LOUISIANA TECH UNIVERSITY

## THE GRADUATE SCHOOL

_____May 6, 2004_____
Date

We hereby recommend that the dissertation prepared under our supervision

by _____Yanjun Tang_____

entitled_____Fabrication, Characterization, and Chemical Sensing_____

_____of Silicon Dioxide Microcantilevers_____

be accepted in partial fulfillment of the requirements for the Degree of

Doctor of Philosophy in Engineering

_____
Supervisor of Dissertation Research

_____
Head of Department

Ph.D. in Engineering
Department

Recommendation concurred in:

_____

_____

_____

_____    Advisory Committee

Approved:

_____
Director of Graduate Studies

_____
Dean of the College

Approved:

_____
Dean of the Graduate School

GS Form 13
(5/03)

# ABSTRACT

The objective of this work is to design and fabricate an advanced silicon dioxide microcantilever sensor and to investigate chemical and biological sensing by microtechnology.

Microcantilever sensor technology has many advantages including fast response time, lower cost of fabrication, the possibility of sensor arrays with small overall dimensions, the ability to explore microenvironments, and improved portability for field applications. For all of these advantages, microcantilever chemical and biological sensors have drawn more and more attention.

So far, all other microcantilevers were designed and fabricated for AFM applications. We developed a novel $SiO_2$ microcantilever especially for chemical and biological sensor applications. First of all, a round tip was added at the end of the microcantilever to ease laser beam injection and 2 $\mu$m in thickness was designed to reduce noise disturbance in chemical or biological sensing. Secondly, the $SiO_2$ microcantilever induces much larger deflection compared with the commonly used Si microcantilever due to the $SiO_2$'s lower Young's modulus. The $SiO_2$ microcantilever thus has much higher sensitivity than the commonly used Si microcantilevers. So, for the chemically specific reaction between $SiO_2$ and HF, it is feasible to detect femtomolar concentrations of hydrogen fluoride using $SiO_2$ microcantilever.

Silicon plasma dry etching was employed to release the $SiO_2$ cantilever from bulk silicon. The spring constant of the cantilevers was measured to be 0.104 N/m.

A fabricated $SiO_2$ microcantilever was used to detect femtomolar concentrations of hydrogen fluoride (HF), a decomposition component of nerve agents.

Also, a SU-8 polymer microcantilever was made by microfabrication techniques. Besides optical detection of microcantilever deflection in a microcantilever sensor system, another detection method known as piezoresistive detection was also developed. A piezoresistive microcantilever was successfully designed and fabricated.

The microcantilever was also developed to monitor impulses. In related research, a superhydrophobic perfluorocarbon nanoneedle surface was successfully synthesized. The water contact angle of this perfluorocarbon surface was measured at 179.8°, which is a record-high contact angle. This research aims at developing microcantilevers with one side covered by superhydrophobic film. In microcantilever surface modification, usually in solution, one surface is fully modified while another side keeps integrated. Maximum differential surface stress is then induced. The superhydrophobic surface was synthesized for this purpose.

## APPROVAL FOR SCHOLARLY DISSEMINATION

The author grants to the Prescott Memorial Library of Louisiana Tech University the right to reproduce, by appropriate methods, upon request, any or all portions of this Dissertation. It is understood that "proper request" consists of the agreement, on the part of the requesting party, that said reproduction is for his personal use and that subsequent reproduction will not occur without written approval of the author of this Dissertation. Further, any portions of the Dissertation used in books, papers, and other works must be appropriately referenced to this Dissertation.

Finally, the author of this Dissertation reserves the right to publish freely, in the literature, at any time, any or all portions of this Dissertation.

Author _Yanjun Tang_

Date _05/13/04_

# TABLE OF CONTENTS

# LIST OF TABLES

# LIST OF FIGURES

# ACKNOWLEDGMENT

I would like to express my sincere gratitude and thanks to my advisor, Dr. Frank Ji, who has instructed me in the scientific method and honest attitude, and co-advisor, Dr. Kody Varahramyan, for his discussion and support. Their invaluable advice, continuous guidance, encouragement, and assistance are necessary for completion of this dissertation. Special acknowledgements are extended to Mr. Ji Fang, Dr. Tabbetha Dobbins, and Dr. Sinedy Sit for their advice and serving as advisory committee members of this dissertation.

The author would like to thank Dr.Karen Xu and all other faculties and staffs at Institute for Micromanufacturing for their help and support on the processing. Much gratitude is extended to Xiaodong Yan, Ke Liu, Min Wang and all my research group colleagues for their valuable discussion, support, and contributions.

I thank God for His grace, charity, and guidance. Finally, I dedicate this dissertation to my wife Ms. Li Cheng and my sweetest daughter Grace whose love and encouragement accompanied me through this research.

# CHAPTER ONE

# INTRODUCTION

## 1.1 Microcantilever

### 1.1.1 Concept of a Microcantilever

Generally, a microcantilever is a long, thin, flexible beam with different shapes. Usually it is V-shaped or rectangular shaped (Figure1-1)[5]. The typical dimensions of a microcantilever are 0.2-2 μm thick, 20-100 μm wide, and 100-500 μm long. The typical materials for fabricating mcirocantilevers are silicon, silicon nitride [1] or silicon dioxide [2]. Other materials have also been applied for this purpose recently, including plastic materials, complex metals, polymer, and piezoelectric materials [3~4]. More and more new types of microfabrication are being developed by microcantilever research teams all around the world (Figure 1-2). Because of the variety of transduction mechanisms, a great deal of interest has been generated in cantilevers for different physical, chemical, and biological sensors.
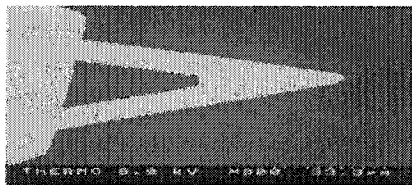
Figure 1-1 A commercial available silicon microcantilever.

1
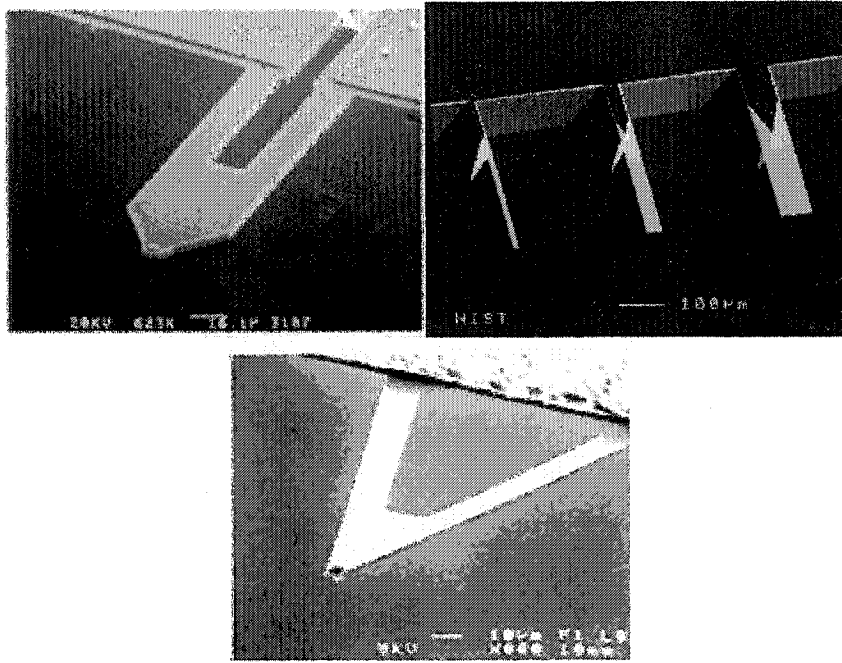
Figure 1-2 Different shapes of microcantilevers.

## 1.1.2. Application of Microcantilever

1.1.2.1 Original Applications. In 1986, the microcantilever was first introduce by Nining *et al.* and used as a scanning probe in the atomic force microscope (AFM) or scanning force microscope (SFM) [6]. Both AFM and SFM are important tools for nanoscience. In both, the principle is based on the fact that the spring constant of cantilever (<<1N/m) is much less than the equivalent spring constant on the surface of the sample. Thus, structures of several nanometers in height will be subjected to an almost constant force. The force on the tip created by the proximity to the sample surface will cause the deflection in the cantilever. (Figure 1-3) As for the measurable distance ($10^{-4}$Å), the force can be as small as $10^{-18}$ N and sensitive enough to penetrate the regime of interatomic force [6]. Obviously, it is a new kind of tool to exploit this level of sensitivity. AFM can measure the topography of a sample surface in nanoscale. Figure 1-4 shows an example of an AFM measurement image.
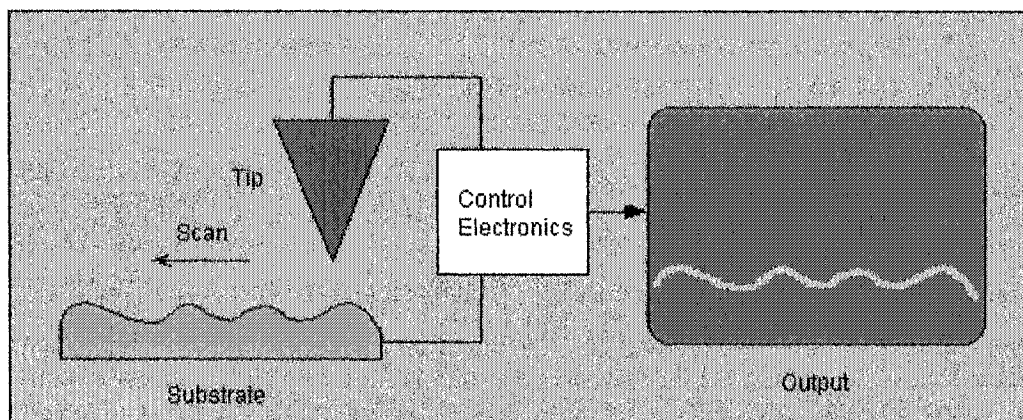
Figure 1-3 Schematic representation of the mcirocantilever tip work in AFM.
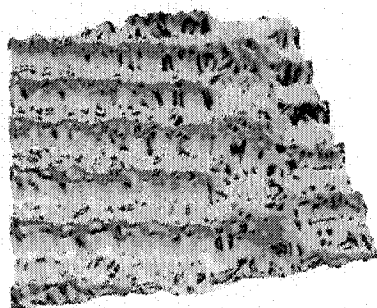


Figure 1-4 AFM measurement image.

The sub-nanometer deflection of microcantilever can be detected by several methods [3] [6, 7], such as a piezoresistive circuit in the stressed region of the cantilever, capacitive defection, and optical method (laser-beam deflection method). Today, the most commonly used method for monitoring the cantilever displacement is the optical deflection technique. This technique is used in current microcantilever sensor research. In the optical method, a laser beam is introduced onto the cantilever and reflected off its backside, and the displacement of cantilever can be measured by detecting the reflection of the weak laser beam. The reflected beam projects on a position sensitive detector (PSD) and monitors the deflection of cantilever in a very precise solution. When used in the AFM, a piezoresistive circuit is used to measure the microcantilever deflection, the

microcantilever scans over the sample surface. The computer analyzes those signals recorded on PSD, and a three-dimensional topography image of the sample surface can be given out.
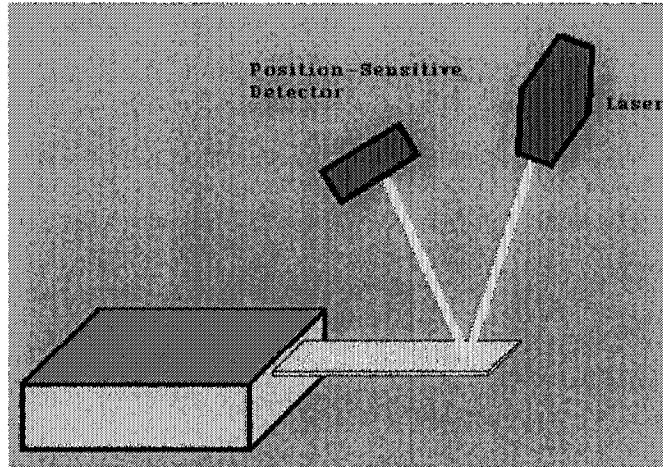


(a)
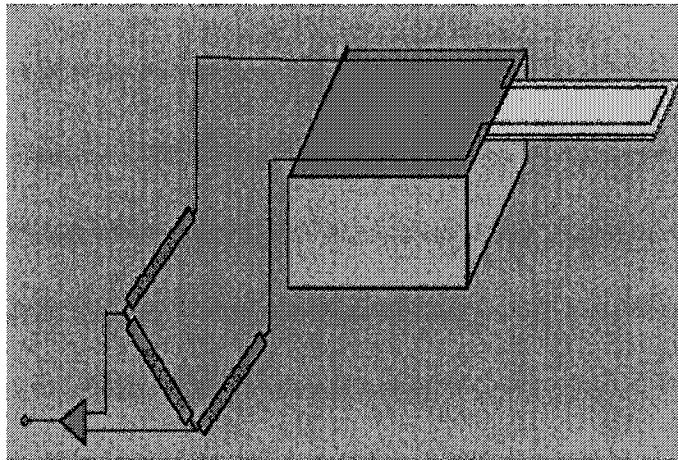


(b)
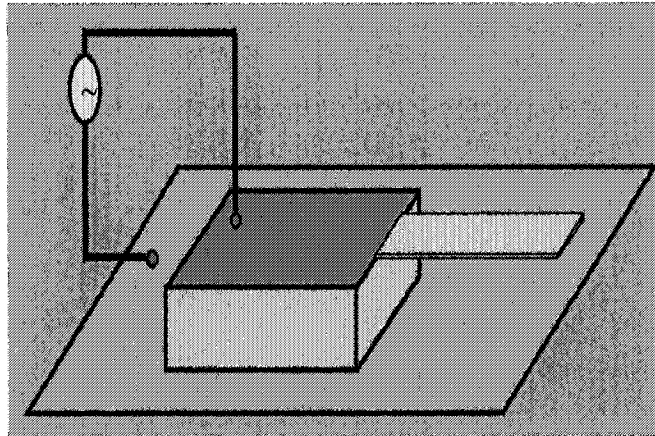
(c)

Figure1-5 Submicron deflection measurement by different
methods (a) Optical (b) Piezoresistive (c) Capacitive.

<u>1.1.2.2 Microcantilever Sensors.</u> In 1994, two research teams, one from Oak Ridge

National Laboratory and the other from IBM Zurich, used the same mechanism of

microcantilever in AFM to develop a new family of sensors. According to their studies,

the AFM cantilever could function as a microcalorimeter. Femtojoule sensitivity can be

achieved, and this achievement shows a great improvement over more traditional

approaches. After that, many research works have been done, and the researchers were

able to show that microcantilevers are a new platform for variety of physical, chemical

and biological sensors. Now, it has become one major device of many

Micro-Electro-Mechanical Systems (MEMS) and Micro-Optical-Elector-Mechanical

Systems (MOEMS). In AFM, the force is applied at a single point (the tip), while recently

the thermally or chemically generated stresses over the whole cantilever surface have

been taken advantage for measuring extremely small bending moments.

Among the beginning applications performed by microcantilever sensors, the most

important one is for the detecting local temperature changes associated with chemical and

physical processes on the cantilever surface. This application took advantage of the extremely low heat capacity of the micromachined suspended bi-material structure and the subnanometer accuracy of cantilever deflection. Due to the heat capacity difference, the bimetallic microcantilevers can exhibit static deflection as a result of thermal effects [8-9]. With an optical cantilever readout, the device had the potential to detect 1pJ if thermal energy and $10^{-5}K$ temperature difference [10].

Resonance responses of the cantilever were recently discovered to exist when cantilever undergoes changes due to adsorption or changes in environment [11]. There are four types of such resonance are of potential application, which are frequency, bending, Q-factor, and amplitude. All these four resonance responses can be simultaneously and sensitively monitored by many techniques. Each of these modes is associated with different transduction scenarios. Presently, microcantilevers have been applied to test the changes in the following areas: the mass increase due to molecular adsorption [1][12~13]; the changes in humidity [14]; viscosity [15]; pressure, density and temperature [8], flow rate; pH[18]; and the presence of radiation [15]. In the detection of specific compounds, cantilevers with selective coatings similar to those used with other transducers and chemical separation techniques have shown specificity to volatile organic compounds, ionic species, proteins, and oligonucleotides. Combined with principal component and artificial neural network analyses, the polymer-modified cantilever was successfully implemented as an artificial nose. Notable discriminating power was observed for alcohol mixtures and certain natural flavors [16]. Most recently, the potential uses of cantilever in bisensors, biomicroelectromechanical systems, proteomids, and genomics are recent

intriguing trends in tech development of biomedical analyses.

Due to their characterized properties, the microcantilever sensors have many unique features and advantages:

- Sensitivity—is the most important and outstanding achievement of this kind of sensor. Resonance frequency changes can be applied for exploring the impressive mass sensitivity. By measuring shifts in the resonance frequencies of microcantilevers, the researchers were able to show that the sensitivity of cantilevers to minute quantities of adsorbed molecule was superior to that of traditional quartz crystal microbalance (QCM) and surface acoustic wave (SAW) transducers. The experiment has shown mercury vapors adsorbed from air onto a gold-coated cantilever caused pronounced shifts in the microcantilever resonance frequency and could be used to detect $10^{-12}$g of mass changes.

Ultra small spring constants make the cantilever highly sensitive to stress differentials between the substrate and coating layer. It has reported the sensitivity of parts-per-trillion (ppt) for both liquid or gas state detection. The sensitivity for $Cs^+$ can reach as low as $10^{-10}M^{[17]}$. The coating method has achieved a sensitivity for mercury vapor detection at $20 \times 10^{-9}g/m^{3[13]}$, which is a significant improvement compared with the sensitivity of $3 \times 10^{-6}M$ of the currently commercial mercury sensor. In another important application area, when the coating method is used as a biological sensor, the sensitivity level is much higher than the standard for clinical requirement. In DNA hybridization detection, even one oligonucletotide mismatch can be distinguished[18].

- Wide application availability – The same platform can be used to detect a wide variety of chemical and biological materials as well as physical parameters by

appropriated modification of the cantilever element. In addition, the sensor platform works easily in air, under liquid and in vacuum.

• Multiple application – Microcantilevers are extremely small, thus the entire sensor (lever, transducer, and electrical detection) could fit in a volume less than few millimeters. Several hundred cantilevers can be put onto a single silicon chip, and the way to measure the deflection of all simultaneously with a single low-power laser or light emitting diode have been developed.

• Selectivity—The specific surface can be developed by coating different molecules on it and then designed selectivity can be achieved[19].

With these advantages, the newly developed microcantilever sensor will provide a revolutionary progress in the sensor technology.

## 1.2 Review of Microcantilever Biological and Chemical Sensors

Due to the faster response time, lower cost of fabrication, the possibility of sensor arrays with small overall dimensions, the ability to explore microenvironments, and improved portability for field applications, microcantilever chemical and biological sensors have been drawn more and more attention. The microcantilever chemical, and biological sensors are briefly summarized in this section.

### 1.2.1 Microcantilever Chemical Sensors

Microcantilevers have been developed for chemical detection with high sensitivity. Microcantilever chemical sensors can be used to detect chemical agents either in gas phase or in solution.

1.2.1.1 Vapor Sensors. Microcantilevers have been used as a new detection platfom for measuring trace gases. Both resonance frequency and deflection can be used for the detection of vapors in air. Coated by different thin film materials, such as metal, hydrogel, polymer, or zeolite, etc. microcantilever vapor sensors are used to detect variety of trace vapors, including $H_2$[32], $Hg$[33], $VOC$[34-36], $Freon$[37], explosive[38-39]. Thin film materials were widely used in the fields of microtechnolgy and now nanotechnology. Mechanical properties such as the Young's modulus are of great interest in designing fabrication processes. A variety of methods have already been developed using the elastic properties of thin films.

1.2.1.2 Sensors for Analytes in Solutions. When a uniform surface stress is applied to an isotropic material it either increases (compressive stress) or decreases (tensile stress) the surface area. If this stress is not compensated by an equal stress on the opposite side of the microcantilever, it will cause a bending of the entire structure with a constant radius of curvature. The untreated, opposite side is essentially passive with respect to the chemically treated side creating a situation that produces a differential stress, thus aiding in chemical detection. So far, the sensors developed for analytes in solutions include $Cs^{+[40]}$, $CrO_4^{2+[41]}$, $Ca^{2+[42]}$, $Hg^{2+[43]}$.

1.2.2 Microcantilever Biosensors

Biosensors have attracted considerable interest in the last few years since the monitoring of a specific substance is central in many applications ranging from clinic analysis to environmental control and many industrial processes. Biosensors offer many advantages in comparison to many conventional analytical approaches in terms of

simplicity and lower detection limits. The simplicity of many biosensor formats often allows for their use by untrained person. For example, patients can monitor glucose within blood or urine from home. Or alternatively, a patient's glucose can be monitored within a doctor's surgery, thus negating the need for samples to be returned to pathology laboratories or other centralized clinical biochemistry laboratory facilities. One of the greatest advantages that biosensors frequently enjoy is their specificity due to their exploitation of biological molecules such as enzymes or antibodies. Analyses *via* biosensors may frequently be performed without the need for formal training, and for this reason many human sources of error may often be eliminated. MC-based biosensors offer new, exciting opportunities in developing microscopic biomedical analysis systems with unique characteristics. Current MC-based biosensors can be generally grouped into the following types: DNA based sensor, antibody based sensor and enzyme based sensors [32-33]

## 1.3 Research Objective

With the overview of microcantilever biological and chemical sensors, it is of great interest to continuously develop new microcantilever sensor to exploit its potential in biological and chemical sensing. Besides current microcantilever sensor technology, efforts aim at developing microcantilever sensors in new materials and novel structures to employ new technology in chemical and biological detection.

In this dissertation, microfabrication technology was developed to fabricate novel microcantilever sensors, including $SiO_2$ microcantilevers, polymer microcantilevers, and

piezoresistive microcantilever to promote microcantilever sensing in addition to current technology. Fabricated microcantilevers were used for chemical and biological detection.

## 1.4 Organization of This Dissertation

Chapter one, as an introduction, describes the brief overview concept, history and application of microcantilever, followed by a operation mechanism. Chapter two describes fabrication of microcantilever sensors. Chapter three describes characterization of microcantilevers. Chapter four describes experiment equipment and procedures. Chapter five investigates the detection of HF. Chapter six investigates impulse monitoring using microcantilever sensors. Chapter seven details related research work. And, chapter eight is the conclusion and future work.

## 1.5 Operation Mechanism

Experimental results have indicated that surface effects due to adsorption or changes in environment have significant influence on the sensitivity of the microcantilever devices and its resonance characters [11]. Depending on the measured parameter (deflection or frequency), the mode of cantilever operation can be either static or dynamic. Both the theories and models have developed for the application in physical, chemical, and biological fields in recent years such as mechanical theory and characterization and electrical theory and characterization.

## 1.5.1 Frequency Mode

Microcantilever operating in a frequency mode are essentially mechanical oscillators. Simple classical models can be used to evaluate it quite rigorously. For an oscillating cantilever[34-36]:

$$f = \frac{1}{2\pi}\sqrt{\frac{K}{m^*}}$$ (1.1)

$$m^* = \frac{3}{8}\rho WtL$$

$$\text{or} \quad m^* = nm_b$$

$k$ is the spring constant of the cantilever. L and W are the cantilever's length and width, $\rho$ is density, and $m^*$ is the effective mass of the microcantilever. The effective mass $m^*$ is proportional to the geometrical dimensions, length(L), width (W), and thickness (t) of the cantilever sensor. Also, $m^*$ can be related to the mass of the beam, $m_b$, through the geometric parameter n.

There are three main mechanisms related to the resonating cantilever: adsorbate-induced mass loading, damping caused by the viscosity of the media, and environmentally induced elasticity changes in microcantilever material. In many sensing applications, cantilever oscillations are insignificantly damped by the medium in which the mcirocantilever resides, or by the a coating on its surface. Under these conditions, the analyte mass binding to the cantilever can be straight forwardly related to a shift in the cantilever resonance frequency, f, from $f_0$ to $f_1$[20]:

$$\frac{1}{f_1^2} - \frac{1}{f_0^2} = \frac{\Delta m}{4\pi^2 k}$$ (1.2)

$\Delta m$ is the additional suspended mass; $k$ is the cantilever spring constant.

From this equation, a high fundamental frequency is required to achieve appreciable mass sensitivity. For nanoscale cantilever with fundamental frequencies of $10^5$-$10^6$Hz, the single-molecule layer ($10^{-21}$g) mass sensitivity can be predicted.

## 1.5.2 Static Bending Mode

The static bending mode was used in the majority of the more recent studies on microcantilever sensors. In the absence of external gravitational, magnetic, and electrostatic forces, deflection of the cantilever is unambiguously related to asymmetric, out-of plane (differential) mechanical stress generated in the cantilever. By confining the adsorption to one side of the cantilever, since the mass on the surface has been changed, there will be an adsorption-induced differential stress on the cantilever, and the cantilever is sensitive enough to respond to this stress change. The device can be made to undergo bending.

There are different coatings that provide the chemical response of cantilever working in a static bending model. Usually, three distinctive models have been considered. The first model is most adequate when interactions between the cantilever and its environment are purely surface confined. The second one is applicable when a microcantilever is modified with an analytic permeable coating that is much thicker than a monolayer. The third model is relevant to structure (heterogeneous) interfaces and coating. Among them, the first model has received much detailed research.

Adsorbate-induced deflection can be accurately described by the Stoney's formula [31-38].

$$\frac{1}{R} = 6\frac{(1-v)}{Et^2}\delta s \qquad (1.3)$$

Where R is the radius of curvature for the cantilever, v and E are Poisson's ratio and

Young's modulus for the substrate, respectively, t is the thickness of the cantilever and δs

is the film stress change. This equation can also be written as the following in terms of Z,

the displacement of the cantilever at the free end point, and L, the length of the cantilever.

Figure 1-6 gives the simulation of their detail.

$$Z = 3\frac{(1-v)}{Et^2}L^2\delta s \qquad (1.4)$$
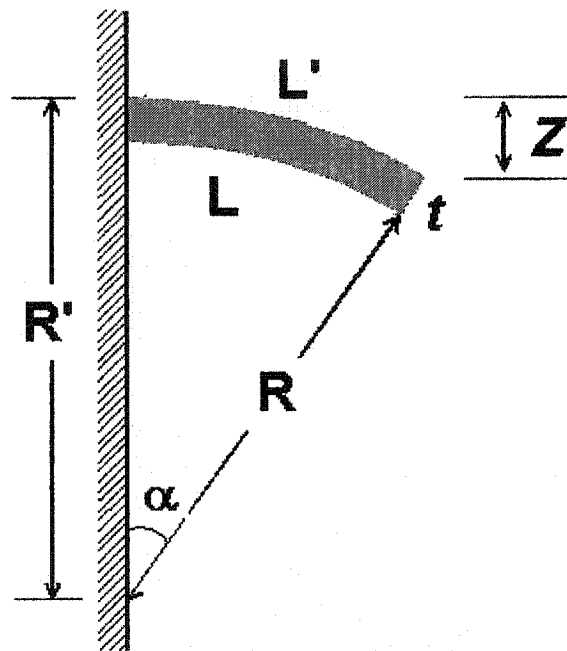


Figure 1-6 Diagram of Microcantilever.

### 1.5.3 Derivation of Stoney's Equation

The bending of microcantilever beam is induced by surface stress. To derive how the

surface stress cause the bending of whole beam, a system is reasonably assumed as shown

in Figure 1-7. In this system, the surface film on a substrate beam is under biaxial

compressive stress $\sigma_{surface}$.
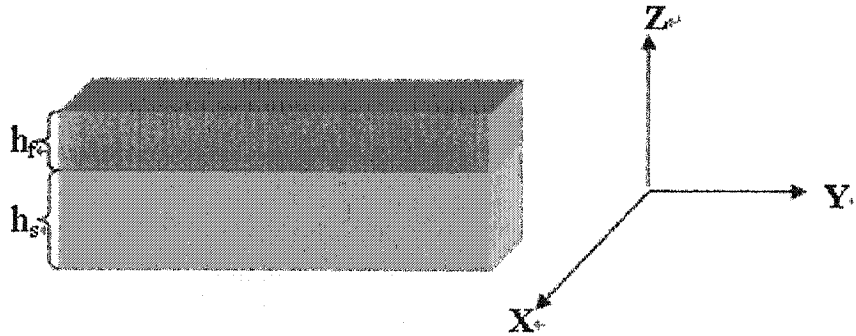
Figure 1-7 Film under uniform biaxial compressive surface stress. $H_f$ is the thickness of surface film, while $h_s$ is the thickness of substrate beam. They both are much smaller than length of beam.
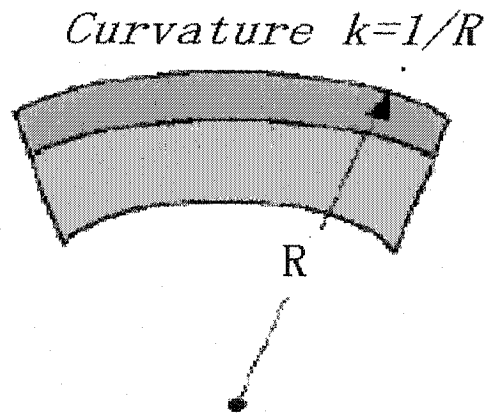


Figure 1-8 Deformation of beam. R is the radius for beam bending.

Assumptions in this derivation:

(i) Homogeneous and isotropic elastic materials

(ii) Small deformation ( $R \gg h_s \gg h_f$ )

(iii) The curvature of bending is the same in both substrate and film

(iv) Perfect adhesion

(v) Ignore edge effects

(vi) Uniform mismatch strain

(vii) The stress is plane stress i.e. $\sigma_{zz}=0$

(viii) Do not consider the effect of defects such as misfit dislocations etc.

Consider the free-body of film and substrate Figure 1-9(b), each interfacial set of forces can be replaced by the statically equivalent combination of a force and moment; $F_f$ and $M_f$ in the film, $F_s$ and $M_s$ in the substrate, where $F_f = F_s$. Force $F_f$ gives rise to the film stress. The moments are responsible for the bowing of the film/substrate composite. Maintenance of mechanical equilibrium therefore requires that the bending moment (M) vanish on any film/substrate cross section, and it implies equality of the clockwise and counterclockwise moments, a condition expressed by:

$$\frac{(h_f + h_s)F_f}{2} = M_f + M_s$$

(1.5)



(a)                                    (b)
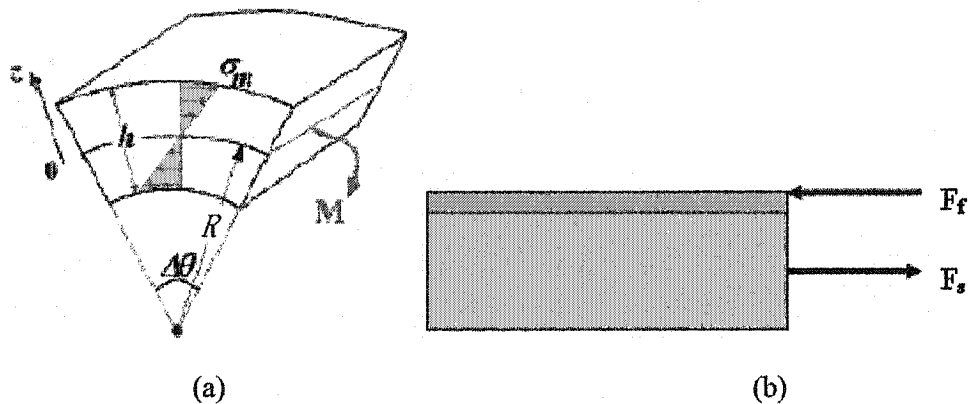
Figure 1-9 Stress analysis.

Now, consider an isolated beam bent by moment M as indicated in Figure 1-9(a). This figure demonstrates the stress distribution across the cross-section of the beam. The deformation is assumed to consist entirely of the extension or contraction of longitudinal beam by an amount proportional to their distance from the central or neutral axis, which remains unstrained in the process. The stress distribution reflects this by varying linearly across the section from maximum tension to maximum compression ($\sigma_m$) at the outer

beam fibers. In terms of the beam radius of curvature R and angle θ subtended, Hooke's

law yields

$$\sigma_m = \frac{E\left[(R + h/2)\Delta\theta - R.\Delta\theta\right]}{R.\Delta\theta} = \pm\frac{Eh}{2R} \tag{1.6}$$

$$\sigma(z) = \sigma_m \cdot \frac{z}{h/2} \tag{1.7}$$

where E is Young's modulus for film and substrate.

Corresponding to this stress distribution is the bending moment across the beam

section with $w$( uniaxial, $w$ depends on Y).

$$M = 2\int_0^{h/2} \sigma_m w\left(\frac{z}{h/2}\right)z\,dz = \sigma_m w h^2 / 6 = Eh^3 w(x)/12R \tag{1.8}$$

Extend this result to the substrate and film, we have

$$M_f = \frac{E_f h_f^3 w}{12R} \quad \text{and} \quad M_s = \frac{E_s h_s^3 w}{12R} \tag{1.9}$$

Consider biaxial-stress distributions in films, rather than the uniaxial stresses assumed for

ease of derivation, we replace $E_f$ by $E_f/1$-$v_f$, and replace $E_s$ by $E_s/1$-$v_s$, with ν the Poisson's

ratio. Substitute these terms in Equation (1.5), for any cross section, we have

$$\frac{(h_f + h_s)F_f}{2} = \frac{E_f h_f^3 w}{12R(1 - V_f)} + \frac{E_s h_s^3 w}{12R(1 - V_s)} \tag{1.10}$$

Because $h_s$>>$h_f$, the film stress $\sigma_{surface}$ can be given by

$$\sigma_{surface} = \frac{F_f}{h_f w} = \frac{E_s h_s^2}{6R(1 - V_s)h_f} \tag{1.11}$$

Thus the film/substrate bending radius can be expressed as the Stoney's equation:

$$R = \frac{E_s h_s^2}{6\sigma_{surface}(1 - V_s)h_f} \tag{1.12}$$

For the cantilever described in Figure 1-6, Stoney's equations are expressed as:

$$\frac{1}{R} = 6\frac{(1-\nu)}{Et^2}\delta s$$

<div style="text-align: right">(1.13)</div>

$$\Delta Z = \left(\frac{3\left(1-\upsilon\right)L^2}{Et^2}\right)\delta s$$

<div style="text-align: right">(1.14)</div>

where R is the radius of curvature for the cantilever, $\nu$ and E are Poisson's ratio and

Young's modulus for the substrate, respectively, L and t are the length and thickness of

the cantilever and $\delta s$ it the film stress change. This equation can also be written in terms

of Z, the displacement of the cantilever at the free end point.

1.5.4 Piezoresistive Microcantilevers

When a piezoresistive material such as doped silicon is strained, its electrical

conductivity is changed. The change in the resistivity can be most conveniently measured

by using a Wheatstone bridge. Piezoresistive microcantilevers are ideal for detecting the

changes in surface stress due to cantilever deflection upon binding of biochemical agents;

they do not require external detection devices, they do not require

tedious alignment, and they can be made to fit in an integrated electromechanical system.

Because strain measurement requires detecting relatively small changes in resistance,

the Wheatstone bridge circuit is almost always used. The Wheatstone bridge circuit

consists of four resistive elements with a voltage excitation supply applied to the ends of

the bridge. Piezoresistive microcantilevers occupy one arm of the bridge, with any

remaining positions filled with fixed resistors. Figure 1.10 shows a Wheatstone bridge
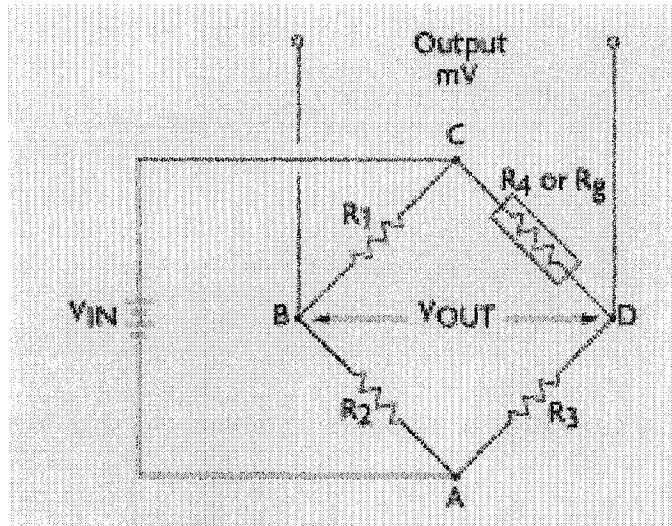
circuit.

Figure 1-10 Wheatstone bridge circuit.

In Wheatstone bridge, the output voltage is calculated as:

$$V_{out} = V_{in}\left(\frac{R_1}{R_1 + R_2} - \frac{R_4}{R_4 + R_3}\right)$$ (1.15)

When the ratio of $R_1$ to $R_2$ equals the ratio of $R_4$ to $R_3$, the measured voltage $V_{out}$ is 0

V. This condition is referred to as a balanced bridge. In the piezoresistive microcantilever

sensor, the piezoresistive microcantilever is taken as $R_4$ (Figure1-11). The resistance

values on the microcantilever changes, causing a change in the voltage at $V_{out}$.
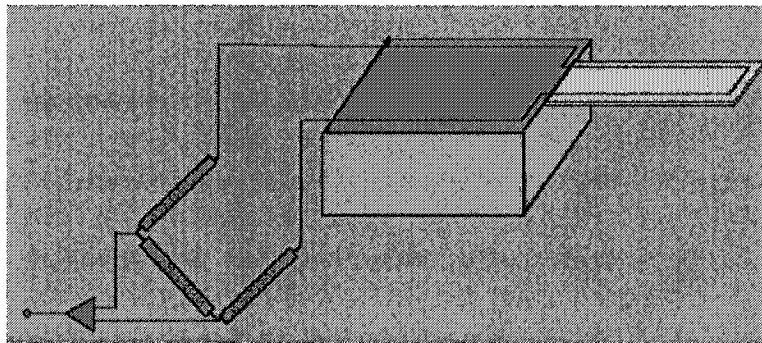


Figure 1-11 Configuration of piezoresistive microcantilever sensor

The fractional change in resistance ($\Delta R/R$) of a piezoresistive cantilever is described by

the following expression

$$\frac{\Delta R}{R} = \beta \frac{3\pi L(1-v)}{t}(\sigma_1 - \sigma_2)$$

(1.16)

where $\beta$ is the piezoresistive coefficient, $\sigma_1$ is the longitudinal stress, $\sigma_2$ is the transverse stress, $t$ is thickness of cantilever, $v$ is Poisson's ratio, which is a factor that adjusts for the thickness of the piezoresistor. From Equation 1.6, the ratio ($\Delta R/R$) is proportional to differential stress ($\sigma_1 - \sigma_2$). Differential stress distribution over a cantilever surface depends on the geometric factors of the layers and the chemo-mechanical forces between the biomolecules and the capture or hybridization layers. Therefore, the deflection signal can be increased by maximizing differential stress ($\sigma_1 - \sigma_2$) by changing the geometric factors.

# CHAPTER TWO

# FABRICATION OF MICROCANTILEVER SENSORS

Based on microfabrication technology, novel microcantilever biosensor and chemical sensors were developed using the microfabrication and nanofabrication facilities in the Institute for Micromanufacturing of Louisiana Tech University. $SiO_2$ microcantilever sensors, piezoresistive microcantilevers, and polymer microcantilever were successfully developed in IfM and used to detect extremely low concentration of chemical and biological agents with ultra high sensitivity. Also, a potentially valuable polymer panel sensor was studied. In this chapter, basic microfabrication technology will be introduced. The facilities and processes related to microcantilever sensor development will be introduced.

## 2.1 Introduction to Microfabrication Technology

Microfabrication or micromachining ( also micro-manufacturing) in the narrow sense comprises the use of a set of manufacturing tools based on batch thin and thick film

21

fabrication techniques commonly used in the electronics industry. In the broader sense, microfabrication describes one of many precision engineering disciplines that takes advantage of serial direct write technologies, as well as of more traditional precision machining methods, enhanced or modified for creating small three-dimensional (3D) structures with dimensions ranging from subcentimeters to submicrometers, involving sensors, actuators, or there microcomponents and microsystems. [9]

Microfabrication starts with photolithography. Photolithography is the process of transferring a pattern from a mask to the substrate. The goal is to expose parts of the wafer to the subsequent processing step while protecting the rest of the wafer. This is done through a sequence of steps: application of photoresist, selective photo exposure through a mask, and developing that removes exposed photoresist from the desired regions.

By a photolithography process, a photomask pattern is transferred onto the surface of solid material, such as silicon, silicon dioxide, metal layer, etc. A pattern can be transferred either by wet etching or by dry etching.

The following is the typical 10-step photolithography process (Figure 2-1)[40]:
Photolithography steps:

1. Wafer surface preparation

    Wafer surface preparation step is used to remove organic contaminants and drive off any moisture in order to improve uniform spreading and adhesion.

2. Photoresist apply

    This step applies a uniform coating of photoresist by spin coating.

3. Softbake step

The softbake step drives off solvents, improves adhesions, and anneals away stress that was introduced during the spin process.

4. Alignment and exposure

Precious alignment of photomask to wafer and exposed to photo light in order to dissolve (positive) or cure (negative) the photoresist.

5. Development step

In this step the exposed (positive) or unexposed (negative) photoresist is removed to leave the desired mask pattern.

6. Hardbake step

Like the softbake this step is used to further remove solvents, improve adhesion, and increase the etch resistance of the resist.

7. Development inspection

Check the developed pattern. Make sure the pattern on photoresist layer has been completely and clearly developed but not over-developed.

8. Etch step

Either by wet etching or dry etching, the pattern of photomask is finally transferred onto thin film layer.

9. Photoresist removal

Photoresist is removed from wafer surface.

10. Inspection

Final inspection of the pattern on thin film using optical microscope.

| | | | |
|---|---|---|---|
| 1. | Surface preparation | Clean and dry wafer surface | |
| 2. | Photoresist apply | Apply a thin layer of photoresist to the wafer | |
| 3. | Softbake | Partial evaporation of photoresist solvents to promote adhesion | |
| 4. | Alignment and exposure | Precise alignment of mask to wafer and exposure to u.v. light. Negative resist is polymerized | |
| 5. | Development | Removal of unpolymerized resist | |
| 6. | Hard bake | Final evaporation of solvents | |
| 7. | Develop inspection | | |
| 8. | Etch | | |
| 9. | Photoresist removal | | |
| 10. | Final inspection | | |

Figure 2-1 10-step photolithography process.

Photolithography is the basic process in microfabrication technology. New developments in lithography largely determine which direction the IC industry and Si-based microfabrication will take in the coming years. There are different lithography techniques, and there is a never-ending pursuit to optimize lithography for future use.

Microfabrication seeks high features and high aspects by subtractive (etching) or additive (deposition) techniques. Dry etching is an important subtractive pattern transfer method in integrated circuit (IC) fabrication. Recent progress in deep directional etching as well as environmental concerns helped push dry etching to the foreground in micromachining application as well. Microfabrication also covers variable tools and processes, such as thin film deposition, wet bulk micromachining, and LIGA (the newest microfabrication tool based on deep etch x-ray lithography, electrodeposition). In this chapter, microfabrication facilities and processes related to microcantilever sensor research development are introduced. All processes were performed in the cleanroom of Institute for Micromanufacturing, Louisiana Tech University.

## 2.2 Microfabrication Facilities and Process at the Institute for Micromanufacturing

### 2.2.1 Photoresist Spin Coating

Spin coating is generally regarded as the best way to deposit a uniform coating for many applications such as photoresist coating and dielectric/insulating layer coating. It gives optimal coverage with minimum material usage. This deposition technique is extremely desirable because the process is simple, safe, and inexpensive. In practice, spin coating involves four stages as shown in Figure2-2[41]. In the first stage, gravitational forces dominate. The surface is first wetted with excess polymer solution. In the second stage, rotational forces dominate. Film uniformity is often not present at this stage. In the third stage, viscous forces dominate. The film continues to get thinner but at a slower rate, and excess liquid continues to be expelled. In the final stage, evaporative forces dominate.

Eventually, the film's thickness begins to stabilize as the evaporation of the solvent causes the viscosity of the liquid to rise sharply and overcome the centrifugal forces. What remains is an extremely thin and uniform film that is ready to be further processed.
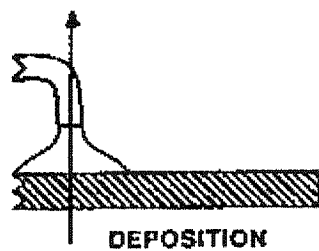


(a) First stage of spin-coating.         (b) Second stage of spin-coating.
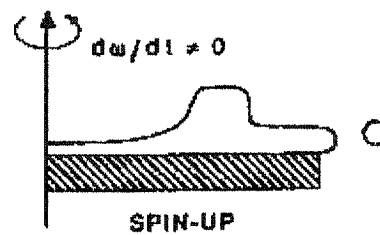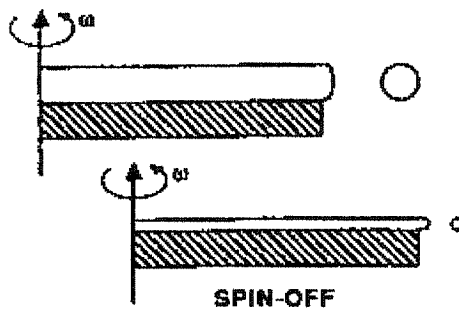


(c) Third stage of spin-coating.         (d) Fourth stage of spin-coating.
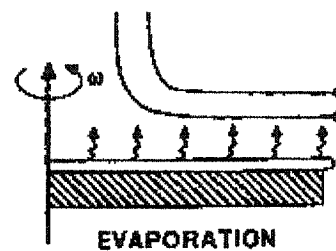
Figure 2-2 Four stages of spin-coating process.

Figure2-2 shows the Brewer Science Cee Model 100 Spin Coating system, by which photoresist was spun on substrate in Institute for Micromanufacturing.
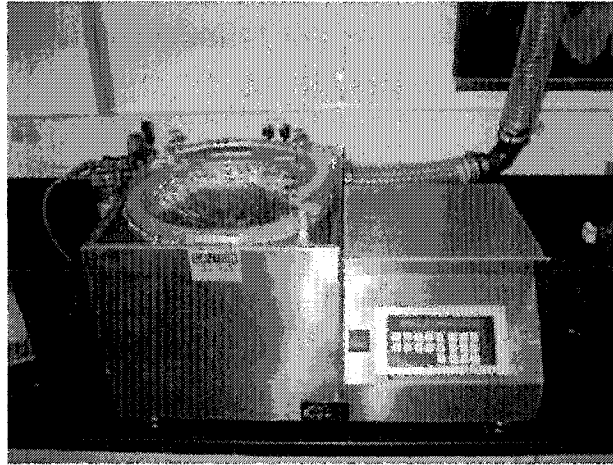
Figure 2-3 Brewer Science Cee Model 100 Spin Coating System.

2.2.2 Pattern Alignment and EV Mask Aligner

In order to fabricate IC devices it is necessary to accurately align patterns already present on a chip to the next pattern in the lithography sequence. The instrument used for this purpose is called a Mask Aligner, for the obvious reason that it aligns a mask to a pattern already on the chip; it also exposes this pattern in the photoresist after the alignment is complete. In photolithography, mask alignment is probably the most challenging and time-consuming step in processing. A mask aligner must serve two purposes: first, it must provide a means to align a pattern on a chip to the pattern on a mask; and second, it must then expose this pattern. Electronic Vision Dual-side Mask Aligner (EV Aligner, Figure2-4) use a rigid frame that the mask while it moves (ideally) only in the vertical direction (z-axis). A separate wafer chuck that holds the chip so that it can rotate about the z-axis ([[theta]] axis)and move in the horizontal plane (x-y plane). A very small gap is set between the chip and mask, and a microscope is used to examine the mask pattern and alignment marks on the chip simultaneously. The x-y and [[theta]] adjustments are then used to bring the two patterns into alignment. After alignment, the

mask and chip are pressed together by using a vacuum, which applies about 14 pounds per square inch of pressure to them. A timer is used to open a shutter, allowing a UV lamp to expose the photoresist.

The most difficult step is the alignment of chip to mask. In industry, special alignment marks and automated pattern recognition are used to perform this step. We must perform the process manually, however. The technique that will allow to achieve precise alignment in a relatively short time is called split-field alignment. The mask aligner microscope actually has two objective lenses, side-by-side. When in the split-field mode, an image which is split in half is viewed, with the left image corresponding to one location on the chip, and the right half corresponding to another location about one inch away. By adjusting the separation of the objective lenses there will occur the same type of alignment marks at two widely separated points on the chip(Figure 2-5). The [[theta]] and x-y translators are then used to move the chip until both of these areas are in view. At that point, the under chip is aligned.

## 2.2.3 Reactive Plasma Etching

Silicon plasma dry etching is a novel anisotropic silicon etch process which overcomes the limitations of other techniques and is fast becoming recognized as an enabling technology for a wide range of applications in MEMS fabrication.[42]

Figure 2-4 Electronic Version Mask Aligner.
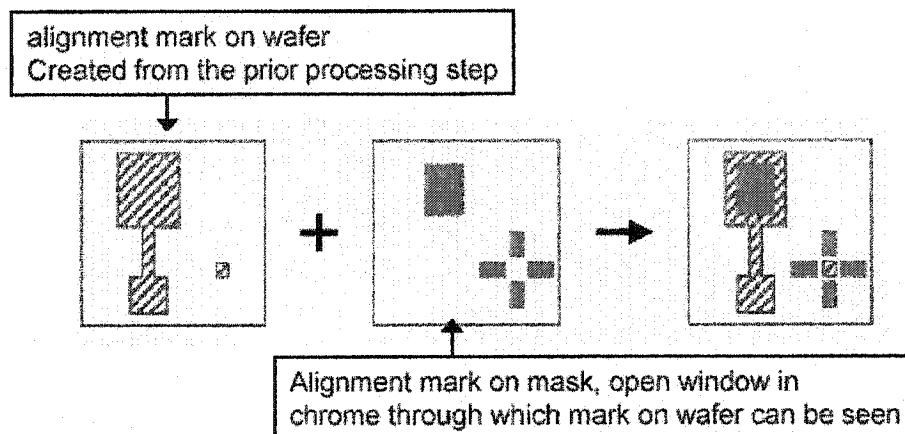


Figure 2-5 Mask alignment.

Integrated circuit fabrication processes that use reactive plasmas are commonplace in today's semiconductor production lines. The term reactive plasma is meant to describe a discharge in where ionization and fragmentation of gases take place and produce chemically active species, frequently oxidizers and/or reducing agents. Such plasmas are reactive both in the gas phase and with solid surfaces to which they are exposed. Then these interactions are used to form volatile products so that material is removed or etched

from surfaces that are not masked by lithographic patterns. The technique is known as reactive plasma etching. [43]

Reactive plasma was used in semiconductor factories in the early 1970s. Reactive plasmas etch the area that is not masked by lithographic patterns into the surface with no lateral material removal under the mask, and therefore replicating the lithographic patterns onto substrates.

Plasma is thought of as a collection of electrons, singly and multiply charged positive and negative ions along with neutral atoms, and molecules and molecular fragments. The charged particles result from the interaction of the initially introduced gas with an applied electric field. Upon the initially applied electric potential, the ionization of a neutral gas molecule, perhaps by photoionization or field emission, will occur. The released electron is then accelerated toward the positive electrode, or anode, and along the way undergoes a series of collisions. Elastic collisions simply deflect the electron, but many types of the inelastic collisions can occur that serve to further ionize or excite neutral species in the plasma. For example, electron collisions such as

$$\text{Dissociative attachment} \qquad e+AB \rightarrow A^-+B^++e \qquad (2.1)$$

$$\text{Dissociation} \qquad e+AB \rightarrow e+A+B \qquad (2.2)$$

$$\text{or Ionization} \qquad e+A \rightarrow A^++2e \qquad (2.3)$$
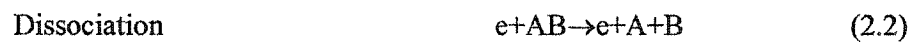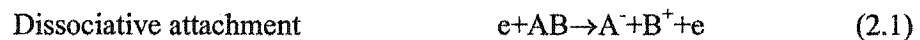
occur, resulting in atoms and molecules or molecular fragments in various states of ionization. Some of these collisions yield more electrons, which raise the state of ionization or the density of the plasma. Additional electrons are generated by secondary emissions from energetic positive ions colliding with the negative electrode or cathode.

Inelastic electron collisions can also cause neutrals and ions to be raised to excited electronic states that later decay by photoemission. These interactions cause the characteristic plasma glow.

An often quoted example of plasma chemistry that has been only qualitatively explained but has a significant impact on semiconductor processing is that of $CF_4$-$O_2$ plasma.[42] In Inductive Coupling Plasma (ICP) system, electric potential is applied by inductive coupling (Radio Frequency, RF) coil. (Figure 2-6 )
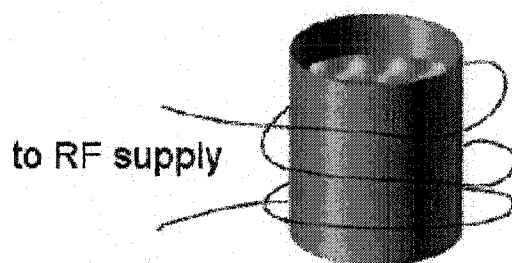


Figure 2-6 Inductive coupling potential.

When $CF_4$ is used as the feed gas, plasma is generated by $CF_4$ gas in RF potential,

$$SF6 + e- \rightarrow SxFy+ + SxFy. + F. +e^- \qquad (2.4)$$
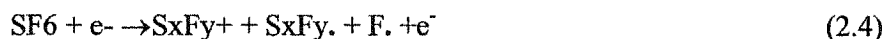
Now, the F can proceed with the silicon etching by adsorption followed by product formation and desorption as a gas (g) :

$$Si + F. \rightarrow Si\text{-}nF \qquad (2.5)$$

$$Si\text{-}nF + ion\ energy \rightarrow SiFx\ (ads) \qquad (2.6)$$

$$SiFx\ (ads) + ion\ energy \rightarrow SiFx\ (g) \qquad (2.7)$$
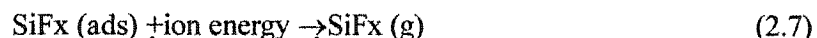
These equations indicate the mechanism that F uses to etch silicon. The dissocialized ion F chemically reacts with silicon to form the transmission compound Si-nF, then Si-nF is bombarded by ion energy and forms volatile $SiFx_{(g)}$. Silicon is thus etched by gaseous

removal. The ion flux provides the directionality and hence controls the anisotropy of the etch. (Figure 2-7)
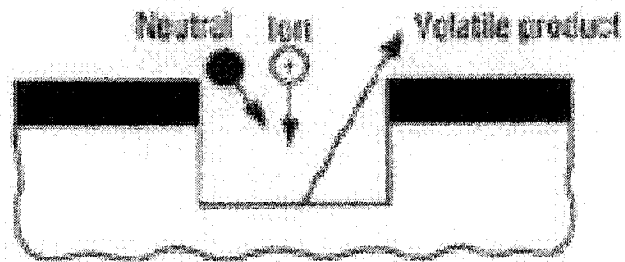


Figure 2-7 Silicon plasma dry etching.

The ICP system in IfM is Alcatel 601E ICP system (Figure 2-8). The feed gas is ionized by the mechanism indicated by equations 2.1-2.3. in the inductive coupling potential (Figure 2-9). The potential is applied by radio frequency (RF) field.



Figure 2-8 Alcatel 601 E ICP system.
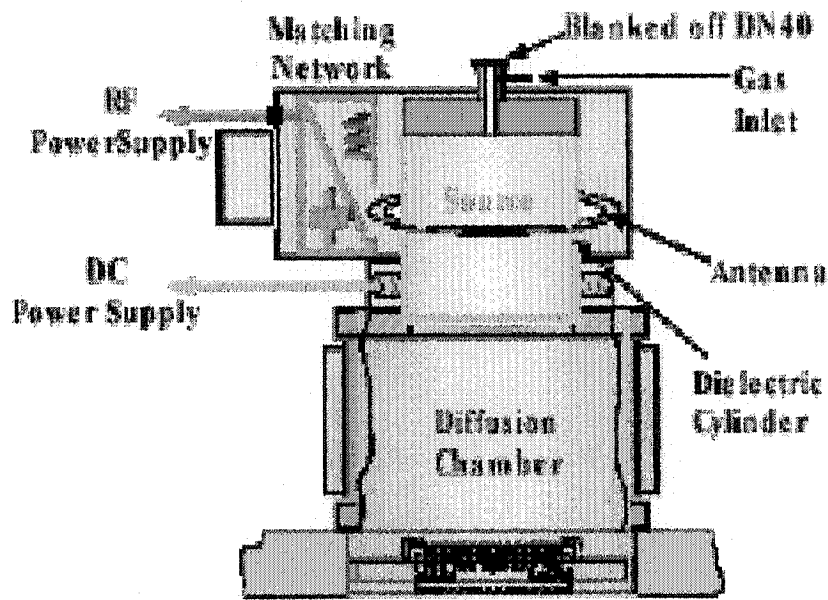
Figure 2-9 The inductive coupling plasma system in
Alcatel 601 E ICP system.

As shown by equations 2.5-2.7, plasma dry etching is comprised of chemical and

physical etching occuring simultaneously. Although in physical etching, the ion flux

provides the directionality and hence controls the anisotropy of etch, the chemical etch

indicated by equation 2.5 is basically uniform in all directions, and form an undercutting

profile beneath masking photoresist instead of a vertical side wall (Figure 2-10).
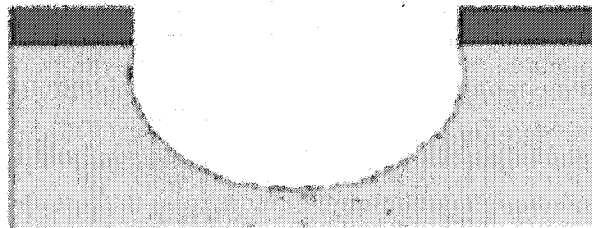


Figure 2-10 Undercutting etching in plasma dry etch.

Due to the inability of all of the aforementioned techniques to meet the goals for the majority of MEMS dry etch applications, novel plasma dry etching processing called Advanced Silicon Etch (ASE) [42] has been developed. ASE now provides a unique processing capabilities. The ASE process is based on the technique invented by Lärmer and Schilp, [42] and uses a variant of the sidewall passivation technique. Rather than the sidewall protection being an integral part of the process, here the passivation is deliberately segregated by using sequentially alternating etching and deposition steps. In this advanced silicon etching process, firstly, a sidewall passivation polymer is deposited and subsequently the polymer and silicon are etched from the base of the trench to allow the etching to proceed directionally in this way.

The principle of the ASE process can be illustrated by comparing a simple reaction model with that for the $SF_6/O_2$. In our process, the deposition and etch precursors are CF4 and SF6, respectively. In this case, firstly the deposition precursor gas is dissociated by the plasma to form ion and radical species (equation 2.8), which undergo polymerisation reactions to result in the deposition of a polymeric layer (Equation 2.9)

$$CF_4 + e- \rightarrow CF_x + CF_{x\cdot} + F_{\cdot} + e- \tag{2.8}$$

$$nCF_{x\cdot} \rightarrow nCF_{2(ads)} \rightarrow nCF_{2(f)} \tag{2.9}$$
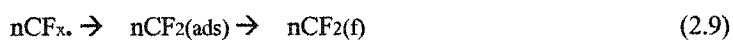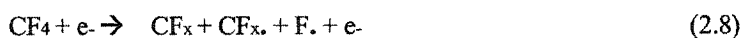
This passivating layer nCF2(f) is deposited on the surfaces of the silicon and the mask during this first step, as shown schematically in Figure2-11(a). Here the subscript (f) is used to emphasise the deposition of the passivation film. The gases are then switched to allow etching. During this subsequent etch step, the SF6 firstly dissociates as in equation 2.4. Next, the fluorine radicals must remove the surface passivation [Figure 2-11(b)].

$$nCF_2(f) + F \cdot \rightarrow \quad \text{ion energy} \rightarrow \quad CF_x(ads) \rightarrow \quad CF_x(g) \qquad (2.10)$$
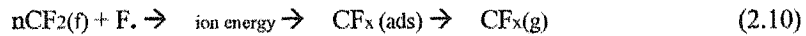
before the silicon etching can proceed as in equations 2.5-2.7. Figure 2-11(c) shows this schematically. After this step, the deposition step is repeated to begin the cycle again. Here the directionality of the etch is controlled by the ion bombardment in its role of aiding the removal of the surface polymer.

Judicious chemistry selection is required to finely control this balance between the etching and the deposition. The deposited polymer must have good conformity, offer adequate sidewall passivation protection, and be readily removed by the etching plasma. Polymeric layers meet most of these needs, particularly since they need only low levels of surface ion bombardment in the presence of a reactive chemical in order to be completely removed from the surface. In this way, low self bias potentials allow the directionality of the etch to be easily controlled (which permits high selectivity to standard photoresists without compromising anisotropy). Etch precursor gases for this type of technique need to liberate high concentrations of chemical etchant to allow relatively high net processing rates taking the discrete deposition steps into account. Suitable candidates include NF3, SF6, etc. Polymeric deposition precursors may be based on a range of appropriate fluorocarbon chemistries such as CHF3, C2F6 and higher molecular weight gases with a higher C:F ratio.
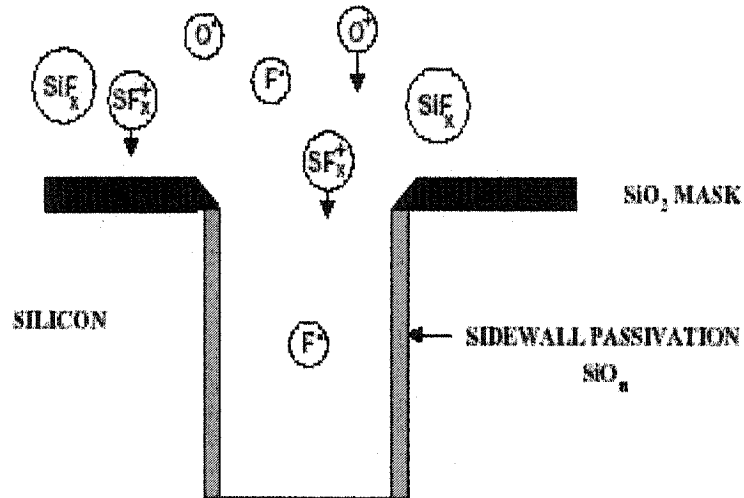
(a) Passivating layer nCF2(f) is deposited on the
surfaces of the silicon and the mask.
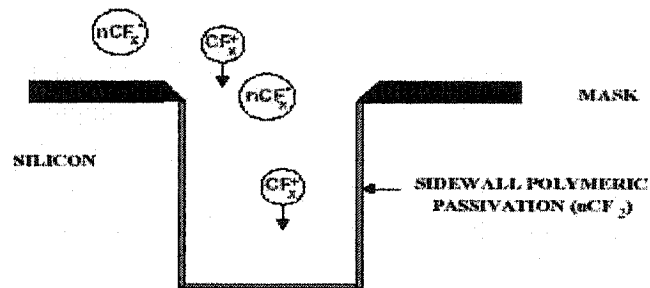


(b) Fluorine radicals remove the surface passivation.
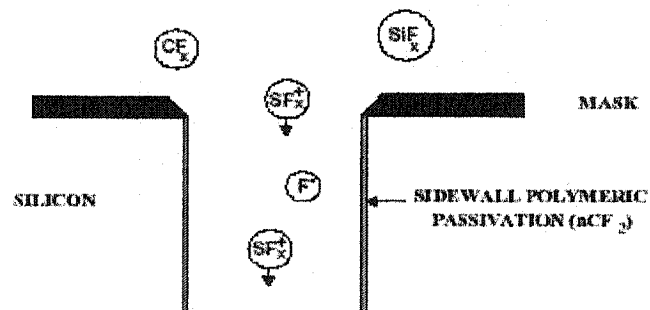


(c) Fluorine radicals etch silicon.
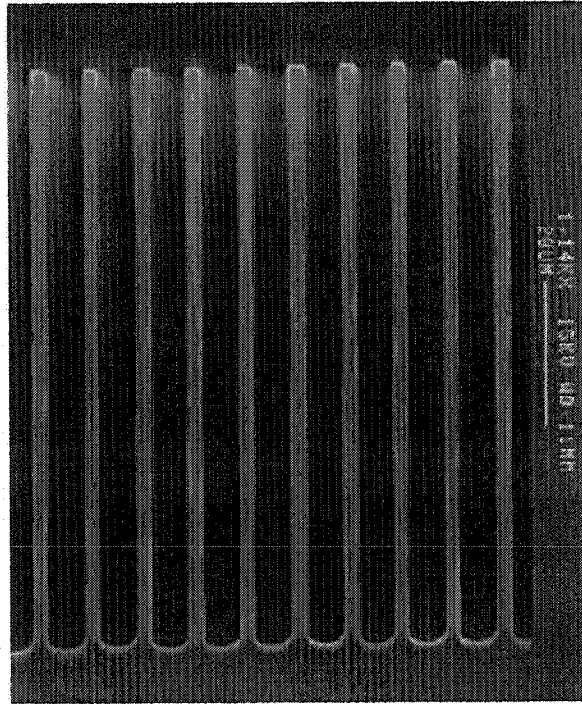
(d) Microscopy image of deep silicon trenches etched
by advanced silicon etch process.

Figure 2-11 Deep silicon plasma dry etch and result.

In Alcatel ICP system, a processing recipe called Bosch big was successfully developed for deep plasma silicon dry etch with good vertical sidewall. The deposition and passivation precursors are $SF_6$ and $C_4F_8$, respectively. The flow rate for the two precursors are 300 sccm and 50 sccm, respectively. The alternative processing duration for the two precursors are 7 seconds and 3 seconds respectively. The bias is 300W. And the temperature is controlled at 20°C by liquid nitrogen at backside of the wafer, since low temperature gives higher etch rate. Figure 2-11 shows deep silicon trenches etched by Bosch big silicon dry etch process. The depth is 80 μm, 4.5 μm space and 2.5 μm line widths. It shows that deep vertical sidewall profile can be obtained by ICP plasma dry etching.

## 2.2.4 Metallization and Lift-off

2.2.4.1 Metallization In VLSI technology, conductive film, very often metal films are required to be deposited on devices to provide interconnection between contacts on devices and between the outside worlds. This technology is called metallization. There are two types of deposition processes that are useful. The first one is called chemical vapor deposition (CVD). And the other one is called physical vapor deposition (PVD). In PVD, deposition of films by thermal evaporation is the simplest method. In the evaporation method, a film is deposited by the condensation of the vapor on a substrate, which is maintained at a lower temperature than that of the vapor. All metal vaporizes when heated to sufficiently high temperatures. Several methods, such as resistive, inductive or radio frequency (RF) electron gun is very commonly used to vaporize metals. The other method of PVD deposition method is sputtering deposition, which is used in IfM for metal film deposition. So, the latter method will be much more detailed in this section.

Sputtering is a technology where the material is released from the source at a much lower temperature than evaporation. The substrate is placed in a vacuum chamber with the source material, named a target, and an inert gas (such as argon) is introduced at low pressure. A gas plasma is struck using an RF power source, causing the gas to become ionized. The ions are accelerated towards the surface of the target, causing atoms of the source material to break off from the target in vapor form and condense on all surfaces including the substrate. As for evaporation, the basic principle of sputtering is the same for all sputtering technologies. The differences typically relate to the manner in which the

ion bombardment of the target is realized. A schematic diagram of a typical RF sputtering system is shown in the figure below. (Figure 2-12)

Within the sputtering process, gas ions out of a plasma are accelerated towards a target consisting of the material to be deposited. Material is detached ('sputtered') from the target and afterwards deposited on a substrate in the vicinity.
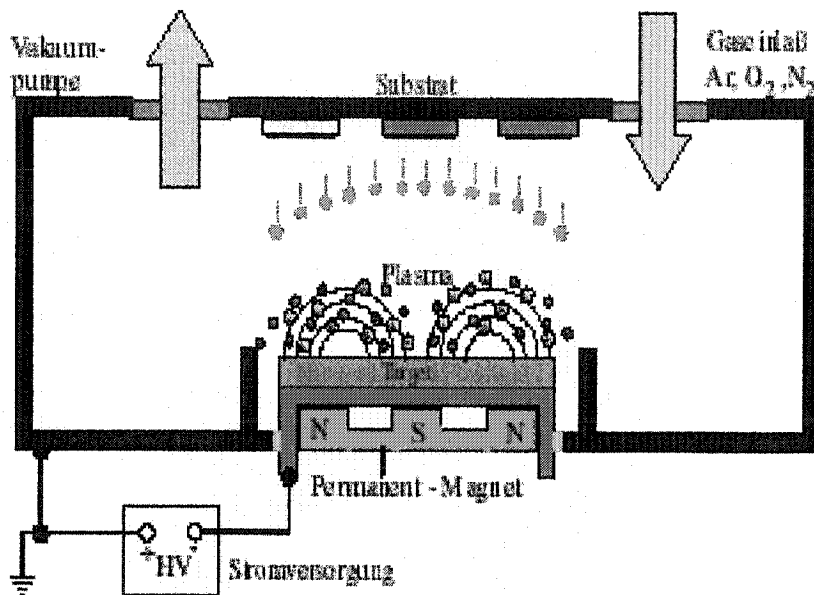


Figure 2-12 A typical RF sputtering system.

To enable the ignition of a plasma, usually argon is fed into the chamber up to a pressure between 0.5~12Pa. By natural cosmic radiation there are always some ionized $Ar^+$ and $Ar^-$ ions available. In the dc-sputtering a negative potential U up to some hundred Volts is applied to the target. As a result, the Ar-ions are accelerated towards the target and set the material free; on the other hand, they produce secondary electrons. These electrons cause a further ionization of the gas. The gas pressure p and the electrode distance d determine a break-through voltage UD from which on a self sustaining glow discharge starts, following the equation UD = A · pd/(ln(pd) + B) with empirical materials

constants A and B. The ionization probability rises with an increase in pressure, and hence the number of ions and the conductivity of the gas also increase. The break-through voltage drops. For a sufficient ionization rate a stable burning plasma results, from which a sufficient amount of ions is available for the sputtering of the material.

To increase the ionization rate by emitted secondary electrons even further, a ring magnet below the target is used in the magnetron sputtering. The electrons in its field are trapped in cycloids and circulate over the targets surface. By the longer dwell time in the gas they cause a higher ionization probability and hence form a plasma ignition at pressures, which can be up to one hundred times smaller than for conventional sputtering. On the one hand higher deposition rates can be realized thereby. On the other hand fewer collisions occur for the sputtered material on the way to the substrate because of the lower pressure, and therefore the kinetic energy at the impact on the substrate is higher (see also below). The electron density and hence the number of generated ions is highest, where the B-field is parallel to the substrate surface. The highest sputter yield happens on the target area right below this region. An erosion zone is formed that follows the form of the magnetic field. The bombardment of a non-conducting target with positive ions would lead to a charging of the surface and subsequently to a shielding of the electrical field. The ion current would decrease to zero. Therefore, the dc-sputtering is restricted to conducting materials, like metals or doped semiconductors. There are two ways to produce dielectric films: in rf-sputtering (radio frequency) and reactive sputtering. In one phase ions are accelerated towards the target surface and sputter material. In the other phase charge neutrality is achieved. In this way, sputtering of non-conducting materials is

also possible. Alternatively, for reactive sputtering other gases like oxygen or nitrogen are fed into the sputter chamber additionally to the argon, to produce oxidic or nitridic films. In this research, thin layer of metal film was coated by sputtering techniques.

2.2.4.2 Lift-off "Lift-off" is a simple, easy method for patterning films that are deposited. A pattern is defined on a substrate using photoresist. A film, usually metallic, is blanket-deposited all over the substrate, covering the photoresist and areas in which the photoresist has been cleared. During the actual lifting-off, the photoresist under the film is removed with solvent, taking the film with it, and leaving only the film that was deposited directly on the substrate.

Depending on the type of lift-off process used, patterns can be defined with extremely high fidelity and for very fine geometries. Lift-off, for example, is the process of choice for patterning e-beam written metal lines. Because film sticks only where photoresist is cleared, the defect modes are opposite what one might expect for etching films (for example, particles lead to opens, scratches lead to shorts in metal lift-off).

Any deposited film can be lifted-off, provided

•During film deposition, the substrate does not reach temperatures high enough to burn the photoresist.

•The film quality is not absolutely critical. Photoresist will outgas very slightly in vacuum systems, which may adversely affect the quality of the deposited film.

•Adhesion of the deposited film on the substrate is very good.

•The film can be easily wetted by the solvent.

•The film is thin enough and/or grainy enough to allow solvent to seep underneath.

•The film is not elastic and is thin and/or brittle enough to tear along adhesion li.

Standard photoresist processing is the easiest method, because it involves only one mask step, and the photolithography is completely standard. The main disadvantage of this method is that film is deposited on the sidewall of the photoresist and will generally continue to adhere to the substrate following resist removal. This sidewall may peel off in subsequent processing, resulting in particulates and shorts, or it may flop over and interfere with etches or depositions that follow.

Prior to film deposition, particularly for sputtering or evaporation processes, a post-develop bake is recommended. This will drive off excess solvent so that there will be less outgassing during the film deposition. However, bake should not occur too long or at too high a temperature, otherwise the resist will reflow slightly.

The film should be deposited as usual. Lift-off can be accomplished by immersing sample in acetone. The length of time for lift-off will depend on the film quality (generally, the higher the film quality, the more impermeable it is, and the longer it will take to lift-off). Depending on how robust the film and substrate are, sidewalls from deposited film can be removed using a gentle swipe of a clean-room swab or a directed stream of acetone from a squeeze bottle. As a rule, keep the substrate immersed in acetone until all the film has been lifted-off, and there are no traces of film particulates -- once particles dry on the substrate, they are notoriously difficult to remove.

(a)

(b)

(c)

(d)

(e)
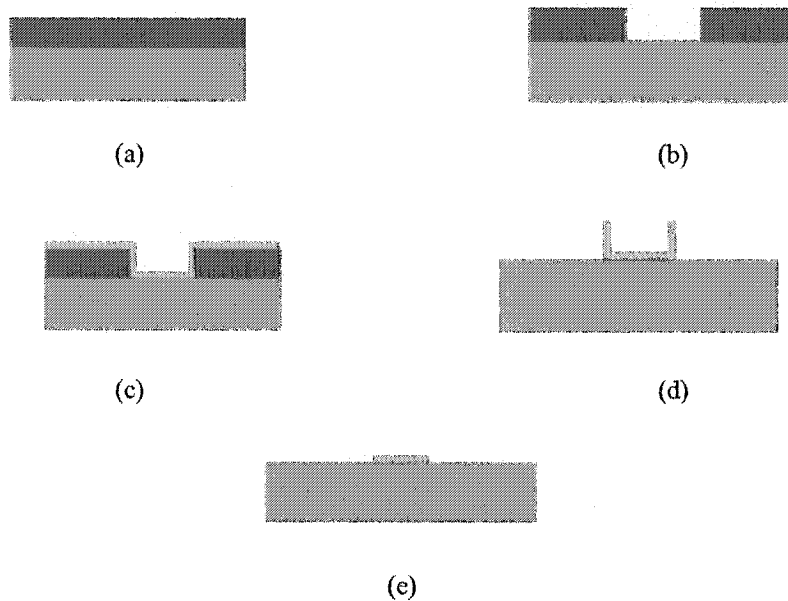
Figure 2-13 Standard photoresis processing lift-off (a) Substrate
with photoresist (b) Exposure and development(c) Film
deposition (d) Lift-off (e) Polish.

The main disadvantage of this method is that film is deposited on the sidewall of the photoresist and will generally continue to adhere to the substrate following resist removal. This sidewall may peel off in subsequent processing, resulting in particulates and shorts, or it may flop over and interfere with etches or depositions that follow.

In order to bypass the disadvantage in standard photoresist processing lift-off and and develop a controllable, repeatable liftoff, a variety of processes have been developed in order to modify the positive resist profile or to develop complex double and triple layer structures whose primary goal is to create a undercut profile. IBM, in the summer of 1980, introduced the first single layer lift-off process that employed profile modification. The photoresist is exposed normally and soaked in an aromatic solvent, typically chlorobenzene. The penetration of the solvent into the resist is controlled by the soaking time. The previously exposed areas, where penetrated, tend to dissolve slower than the un-penetrated areas under normal development. Thus, if the unpenetrated resist is

over-developed, an undercut structure is obtained. This process proved in the long run to have small process latitude and to be very expensive to implement. The poor process latitude appears to be a function of the sensitivity of the resist structure to a wide variety of variables. These variables include exposure energies, developer concentrations, temperature, and time and especially trace impurities in the chlorobenzene. A small variation in any of these variables tended to be catastrophic.

A advanced photoresist LOR lift-off processing was employed in our fabrication. MicroChem's line of LOR lift-off resists are based on the polydimethylglutarimide (PMGI) platform and are well suited for a variety of critical and non-critical level lift-off processes. Used in combination with conventional positive resists, LORs are available in a wide range of film thicknesses and undercut rates. LORs address the process requirements for Giant Magnetorostitant (GMR) and MR heads, wireless devices, opto-electronics such as semiconductor lasers and detectors, MEMS and many other microelectronic applications requiring easy process tuning, high yields and superb deposition linewidth control.

Merits of LOR lift-off photoresist:

• Finely tuned undercuts

• Does not intermix with imaging resists (no scum)

• Excellent adhesion to Si, NiFe, GaAs, InP and many other III-V and II-VI materials

• Simple bi-layer processing without extra flood exposure, develop, amine treatment or toxicchemical soak steps

• Formulations for deposition processes up to 5 μm

1. Coat and prebake LOR

2. Coat and prebake imaging resist

3. Expose imaging resist

4. Develop resist and LOR. LOR develops isotropically, creating a bi-layer reentrant sidewall profile

5. Deposit film. The re-entrant profile ensures discontinuous film deposition.

6. Lift-off bi-layer resist stack, leaving only desired film.
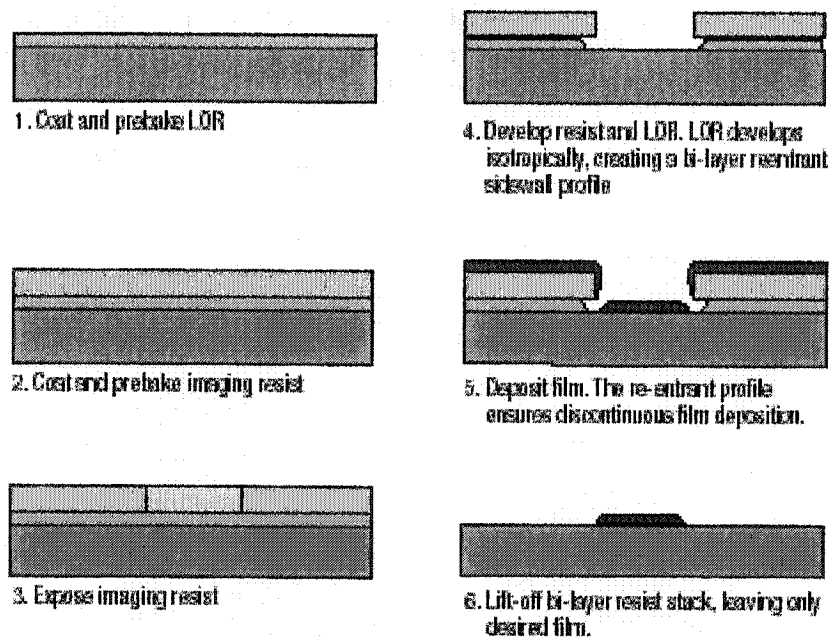
Figure 2-14 LOR lift-off process.

The LOR line of resists include two series:

• LOR A series have relatively low dissolution rates and offer superb undercut control. They are ideally suited for thin-film processes with .26N metal-ion-free developers such as Shipley's CD-26 and TOK's NMD-3.

• LOR B series have relatively high dissolution rates, which makes them ideally suited for thick-film processes. They are optimized for metal-ion-bearing developers such as AZ 400K 1:4, as well as low normality metal-ion-free developers such as Shipley's MF-319.

A LOR photoresist lift-off process is described in Figure 2.16.

1. Coat and prebake LOR

2. Coat and prebake imaging resist

3.Expose imaging photoresist.

4. Develop resist and LOR. LOR develops isotropically, creating a bi-layer reentrant sidewall profile

5. Deposit film. The re-entrant profile ensures discontinuous film deposition.

6.Lift-off biolayer photoresist stack, only leaving desired film.

## 2.2.5 SU-8 Micropatterning

Polymer molding has been used in microfabrication for microdevices. Microsensors have developed by SU-8 molding. SU-8 is a high contrast, epoxy based photoresist designed for micromachining and other microelectronic applications, where a thick chemically and thermally stable image is desired. The exposed and subsequently cross-linked portions of the film are rendered insoluble to liquid developers. SU-8 has very high optical transparency above 360nm, which makes it ideally suited for imaging near vertical sidewalls in very thick films. SU-8 is best suited for permanent applications where it is imaged, cured and left in place.

A normal process (Figure 2-16) is spin coat, soft bake, expose, post expose bake (PEB) and develop. A controlled hard bake is recommended to further cross-link the imaged SU-8 structures when they will remain as part of the device. The entire process should be optimized for the specific application. A baseline process is given here to be used as a starting point.
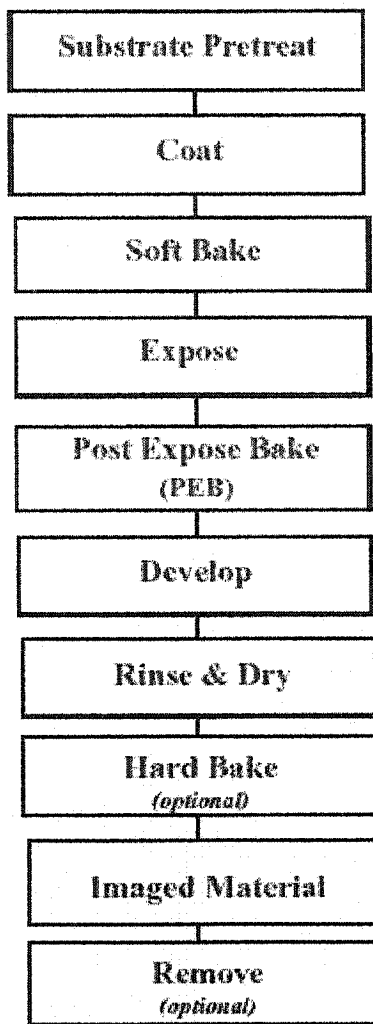
Figure 2-15 SU-8 photoresist process.

<u>Substrate Pretreatment</u> To obtain maximum process reliability, substrates should be clean and dry prior to applying the SU-8 resist. Start with a solvent cleaning, or a rinse with a acid, followed by a DI water rinse. Where applicable, substrates should be subjected to a piranha etch / clean ($H_2SO_4$ & $H_2O_2$). To dehydrate the surface, bake at 200°C for 5 minutes on a hotplate. For applications that require electroplating and subsequent removal of SU-8, apply MicroChem's OmniCoat prior to processing SU-8.

Table 2-1 SU-8 thickness vs. spin speed for selected SU-8 photoresist.

| Product Name | Viscosity (cSt) | Thickness (µms) | Spin Speed (rpm) |
|---|---|---|---|
|  |  | 1.5 | 3000 |
| SU-8 2 | 45 | 2 | 2000 |
|  |  | 5 | 1000 |
|  |  | 5 | 3000 |
| SU-8 5 | 290 | 7 | 2000 |
|  |  | 15 | 1000 |
|  |  | 10 | 3000 |
| SU-8 10 | 1050 | 15 | 2000 |
|  |  | 30 | 1000 |
|  |  | 15 | 3000 |
| SU-8 25 | 2500 | 25 | 2000 |
|  |  | 40 | 1000 |
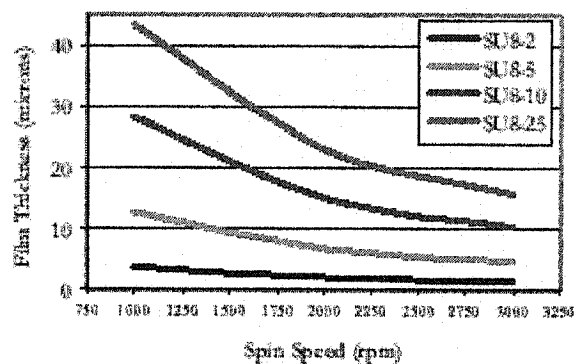


Figure 2-16 SU-8 thickness vs. spin speed for selected SU-8 photoresist.

Coat SU-8 resists are designed to produce low defect coatings over a very broad range of film thickness. The film thickness versus spin speed data displayed in Table 1 and Figure 2-17 provide the information required to select the appropriate SU-8 resist and spin conditions, to achieve the desired film thickness.

Soft Bake After the resist has been applied to the substrate, it must be soft baked to evaporate the solvent and densify the film. SU-8 is normally baked on a level hot plate,

although convection ovens may be used. The following bake times are based on contact hot plate processes. Bake times should be optimized for proximity and convection oven bake processes since solvent evaporation rate is influenced by the rate of heat transfer and ventilation. For best results, ramping or stepping the soft bake temperature is recommended. Lower initial bake temperatures allow the solvent to evaporate out of the film at a more controlled rate, which results in better coating fidelity, reduced edge bead and better resist-to-substrate adhesion. Spin coating refers to spread cycle: ramp to 500 rpm at 100 rpm/second acceleration for 5 seconds and spin cycle: ramp to final spin speed at an acceleration of 300 rpm/second and hold for a total of 30 seconds.

Table 2-2 Recommended softbake parameter.

| Product Name | Thickness (ums) | Pre-bake @ 65°C | Softbake @ 95°C |
|---|---|---|---|
|  | 1.5 | 1 | 1 |
| SU-8 2 | 2 | 1 | 3 |
|  | 5 | 1 | 3 |
|  | 5 | 1 | 3 |
| SU-8 5 | 7 | 2 | 5 |
|  | 15 | 2 | 5 |
|  | 10 | 2 | 5 |
| SU-8 10 | 15 | 2 | 5 |
|  | 30 | 3 | 7 |
|  | 15 | 2 | 5 |
| SU-8 25 | 25 | 3 | 7 |
|  | 40 | 5 | 15 |

Expose SU-8 is optimized for near UV (350-400nm) exposure. I-line exposure tools are recommended. SU-8 is virtually transparent and insensitive above 400nm but has high absorption below 350nm. Excessive dose below 350nm may, therefore, result in over exposure of the top portion of the resist film, resulting in exaggerated negative sidewall

profiles or T-topping. The optimal exposure dose will depend on film thickness (thicker films require higher dosage) and process parameters.

Post Exposure Bake Following exposure, a post expose bake (PEB) must be performed to selectively cross-link the exposed portions of the film. This bake can be performed either on a hot plate or in a convection oven. Optimum cross-link density is obtained through careful adjustments of the exposure and PEB process conditions. The bake recommendations below are based on results obtained with a contact hot plate.

Table 2-3 Recommended post exposure bake parameter

| Product Name | Thickness (µms) | PEB 1 @65°C | PEB 2 @95°C |
|---|---|---|---|
|  | 1.5 | 1 | 1 |
| SU-8 2 | 2 | 1 | 1 |
|  | 5 | 1 | 1 |
|  | 5 | 1 | 1 |
| SU-8 5 | 7 | 1 | 1 |
|  | 15 | 1 | 2 |
|  | 10 | 1 | 2 |
| SU-8 10 | 15 | 1 | 2 |
|  | 30 | 1 | 3 |
|  | 15 | 1 | 2 |
| SU-8 25 | 25 | 1 | 3 |
|  | 40 | 1 | 4 |

SU-8 is readily cross-linked and can result in a highly stressed film. To minimize stress, wafer bowing and resist cracking, a slow ramp or TWO STEP contact hot plate process, as shown in Table 2.3, is recommended. Rapid cooling after PEB should be avoided.

Develop SU-8 resists have been optimized for use with MicroChem's SU-8 Developer. Immersion, spray or spray- puddle processes can be used. Other solvent based developers such as ethyl lactate and diacetone alcohol may also be used. Strong agitation

by ultrosonication is recommended for high aspect ratio and/or thick film structures. Recommended develop times are given in Table 5. for immersion processes. These proposed develop times are approximate, since actual dissolution rates can vary widely as a function of agitation rate, temperature and resist processing parameters.

Rinse and Dry Following development, the substrate should be rinsed briefly with isopropyl alcohol (IPA), then dried with a gentle stream of air or nitrogen.

If a white film is produced during rinse, this is an indication that the substrate has been under developed. Simply immerse or spray the substrate with SU-8 developer to remove the film and complete the development process. Then repeat the rinse step

Hard Bake (cure) SU-8 has good mechanical properties; therefore, hard bakes are normally not required. For applications where the imaged resist is to be left as part of the final device, the resist may be ramp/step hard baked between 150-200°C on a hot plate or in a convection oven to further cross link the material. Bake times vary based on type of bake process and film thickness.

Remove SU-8 After expose and PEB, it is a highly cross-linked epoxy, which makes it extremely difficult to remove with conventional solvent.

<div align="center">

## 2.3 Microfabrication

</div>

## 2.3.1 Review of Microcantilever Fabrication

The manufacturing of microcantilevers is based on the micromanufacturing technologies used in the semiconductor industry. There are different ways to microfabricate a cantilever [9]. For $SiO_2$ or $Si_3N_4$ material, thin films of $SiO_2$ or $Si_3N_4$ are first deposited onto a silicon substrate, then the use of lithography and etching technology

(wet or dry etching) define the cantilever, and finally the silicon underneath the cantilever will be selectively removed and the cantilever has been demonstrated. For Si material, another microfabrication method is to bulk-micromachine out the silicon. The fabrication is processed separatedly in two directions. In the beginning the window for etching from the backside below the cantilever is generated, then one should use photolithography to pattern and define the cantilever on the front side. Finally, the backside etching is performed, and both etch fronts meet, and the cantilever is released.

Single crystal silicon, poly crystal silicon, silicon oxide, silicon nitride layers have been used to form microcantilever beams [44][2]. Meanwhile, microcantilever beams were also formed by particular materials, such as metal film, bimetallic films [50], piezoresistive or piezoelectric films [52-54], semiconductor materials and strained composite structure[58].

Among all the films to form microcantilever beams, silicon oxide, polysilicon and silicon nitride are grown or deposited on the surface of silicon wafer, while silicon film is SOI silicon film. Metal films are physically deposited on substrate. Semiconductor material is normally expitaxy layer grown on substrate [55-57]. All these layers are to define the thickness of fabricated microcantilevers. In fabrication, the cantilever thickness could also be defined by inducing etch stop region, for example, Cho et al. defined cantilever by selective etch stop by the heavily boron-doped region in an anisotropic silicon etchant.

Generally, microcantilever fabrication includes two main steps: first, microcantilever beams are patterned on a thin film layer by standard lithography procedure, and then, the microcantilever beams are released from substrate[45-47]. The silicon on insulator (SOI) wafer was typically used to fabricate the silicon cantilever, and wet etching was employed

to release the cantilever structure from the substrate wafer. Microcantilevers were patterned on silicon film, while the SOI insulator layer (normally oxide) provides a preventive method in wet etching to free the freestanding silicon cantilever from the substrate wafer [44-45]. Silicon cantilever structure was also defined in bulk silicon using heavily boron-doped silicon cantilever[50]. Expensive SOI wafer was not required for this process. Although multi-mask layouts and precise alignment are normally required in lithography processes [2], single mask fabricaticon processes were developed to avoid dependence on alignment[44,47,50].

While in most microcantilever fabrication process, silicon anisotropic wet etching is used to release microcantilever beams from substrate materials[45], dry etching is used to release the cantilever from the substrate wafer. Si cantilever[44] and $SiO_2$ cantilever [2] were released by $SF_6$ dry etching from silicon substrate.

Microcantilevers integrated with sharp tips have been used in atomic force microscopy (AFM). Imaging quality mostly depends on the quality of probe tips. There are different methods to fabricate these tips integrated with microcantilever beams. In Farooqui *et al.* [47]work , tip was formed by $SF_6$ dry etching using silicon oxide as masking and protected by local oxidation (LOCOS). Akamine *et al.* fabricated AFM tip of 220-400Å curvature to improve atomic force microscope images using microcantilevers with sharp tips. When imaging atomically flat samples using cantilevers with sharp protruding tips, atomic corrugations are observed more consistently and with a higher signal-to-noise ration than in the absence of tips.

Microcantilevers have long been fabricated for AFM probes[47], they have been recently used in physical, chemical, biological sensors. Harris et al. [57] fabricated 100-nm-thick GaAs cantilever for strain-sensitive force detection, the GaAs epilayer was grown by molecular beam epitaxy. Tang et. al. [2] design and fabricated 2μm silicon oxide microcantilevers for microsensor application. Jung et al.[51] fabricated bimetallic cantilevers for chemical sensor applications. Datskos et al.[55] fabricated quantum well microcantilevers to detect photons, the semiconductor material GaAs/GaAlAs used quantum well. Molecular beam epitaxy (MBE) used to grow quantum well. Single point diamond turning (SPDT) and ion beam milling were used to remove material and pattern microcantilevers. Different from traditional silicon-based microelectronic integrated circuit fabrication processes, it typically involves substantial wet and dry chemistry to create microstructures of interest. Mounaix et al.[90] fabricated GaInAs semiconductor matilever. GaInAs film was grown from InP layer by MBE. HCl-based etchants etches InP antisotropically due to the zinc-blends structure of InP and the cantilever was released from the InP substrate. Itoh et al. [0-52-54] used ZnO layer on SiO₂ film to fabricate new type of self-excited force-sensing microcantilever for dynamic scanning microscopy (SFM). Sones et al. [85] fabricated of piezoelectric micro-cantilevers in domain-engineered LiNbO₃ single crystals.

## 2.3.2 Microcantilever Fabrication

•Microcantilever design

Geometrical design of $SiO_2$ microcantilever is referred to the geometry of currently used Si microcantilever for the purpose of mechanical characterization. Since the

commercial Si microcantilever has been calibrated and all its mechanical properties are known, it can be used to calibrate fabricate $SiO_2$ microcantilever with close geometry dimensions. The mechanical properties of Si and $SiO_2$ microcantilevers are listed in Table 3-1 Comparison of $SiO_2$ cantilever and silicon cantilever. And the calibration of $SiO_2$ microcantilever is described in Chapter three of this dissertation.

But different from a typical V-shape cantilever, a round platform is put at the tip area of designed cantilever to make laser incidence much more convenient and increase sensitivity. 2 μm thickness was designed to give better mechanical strength. The sensitivity of chemical sensing can be improved by lowering the spring constant κ of the cantilever (thereby increasing the displacement per unit force). Cantilever geometry shape was designed, combined with the mechanical properties of $SiO_2$ material, to give much lower spring constant κ than commercialized silicon cantilevers. The length of cantilever is 200μm and the width at the root is 150μm.

●Material

The fabrication process began with 500 μm thick silicon wafer with 2μm thick layer of thermal silicon dioxide grown on both sides. (Figure 2-20 (a))
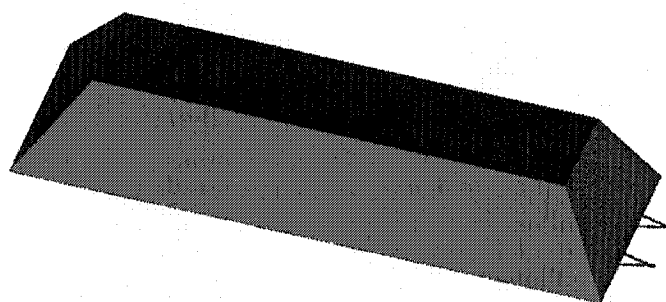


Figure 2-17 Designed microcantilever.
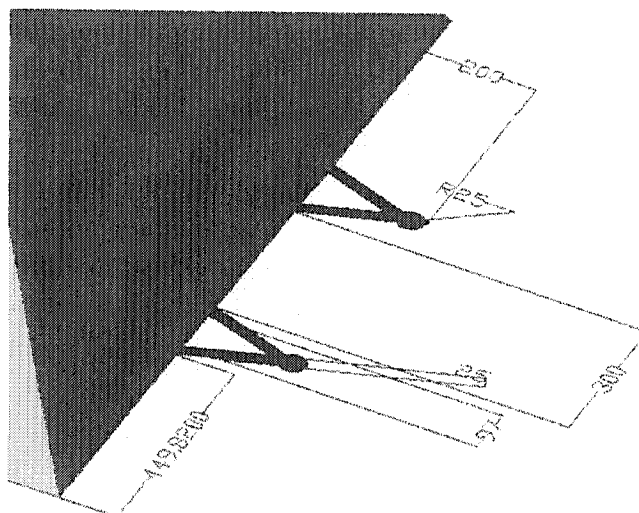
Figure 2-18 Dimensions of the designed microcantilever.

● Photoresist coating

The spin speed of 3000 rpm for 50 seconds. The thickness of coated Shipley 1813 photo resist layer was about 2μm (Figure 2-20 (b)).

● Alignment and Exposure

After soft baking at 110°C for 1 min., the wafer was UV exposed by EV Aligner for 4 seconds using the mask carrying cantilever beam pattern. The wafer was then developed with developer MF-319 to obtain a clear and clean cantilever beam pattern on photoresist layer. After hard baking also at 110°C for 1 min., the wafer was chemically wet etched using buffered oxidation etchant (BOE $HF:H_2NO_3$=1:6) for 18 minutes to form a cantilever beam on the $SiO_2$ layer on front side and to etch away the entire $SiO_2$ layers on back side (Figure 2-20 (c)). Afterwards, Shipley 1813 photo-resist was rinsed by acetone and DI water to get a clean surface on the cantilever beams (Figure2-20 (d)). Photo resist AZ9260 was coated on backside of the wafer by applying AZ9260 at the spin speed of 3000 rpm for 50 seconds. AZ9260 was applied twice to yield a total AZ9260 thickness

of 20 μm. The thick photo resist layer was needed for deep silicon plasma etching process (Figure 2-20(e)). After 1 minute soft baking at the temperature of 110°C, the wafer backside was exposed to a mask carrying the pattern of cantilever support. The photo resist was then developed using developer AZ400k to form the pattern of cantilever support on AZ9260 photo-resist layer (Figure 2.20(f)). After 15 minutes of hard baking at 110°C, wafer was dry etched by an ICP process using thick AZ9260 photo resists as masking to totally release the microcantilever beam from silicon (Figure 2-20(g)).

(a)

(b)

(c)

(d)

(e)

(f)

(g)
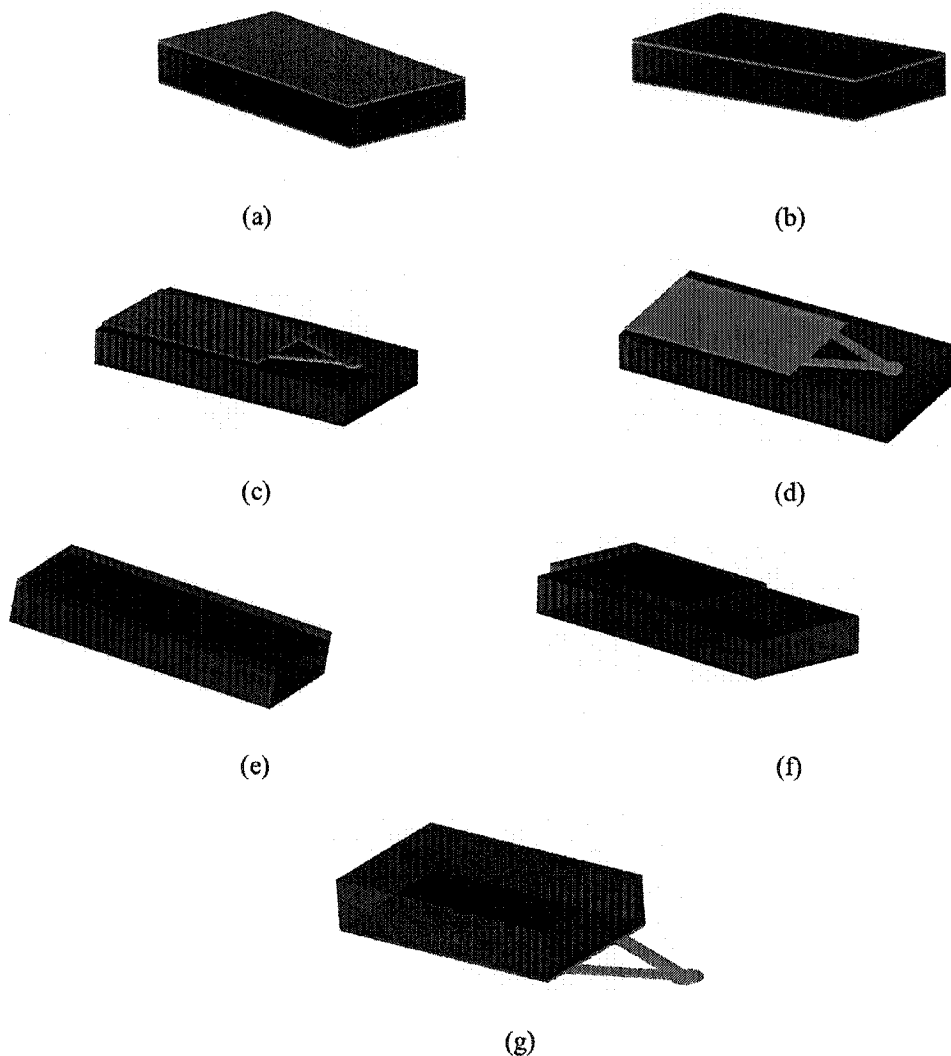
Figure 2-19 Microcantilever fabrication flow.

Results and Disscussion $SiO_2$ microcantilevers were successfully mass produced (Figure 2-20). The microscopy image of fabricated $SiO_2$ microcantilever is shown in Figure 2-21 and Figure 2-22.
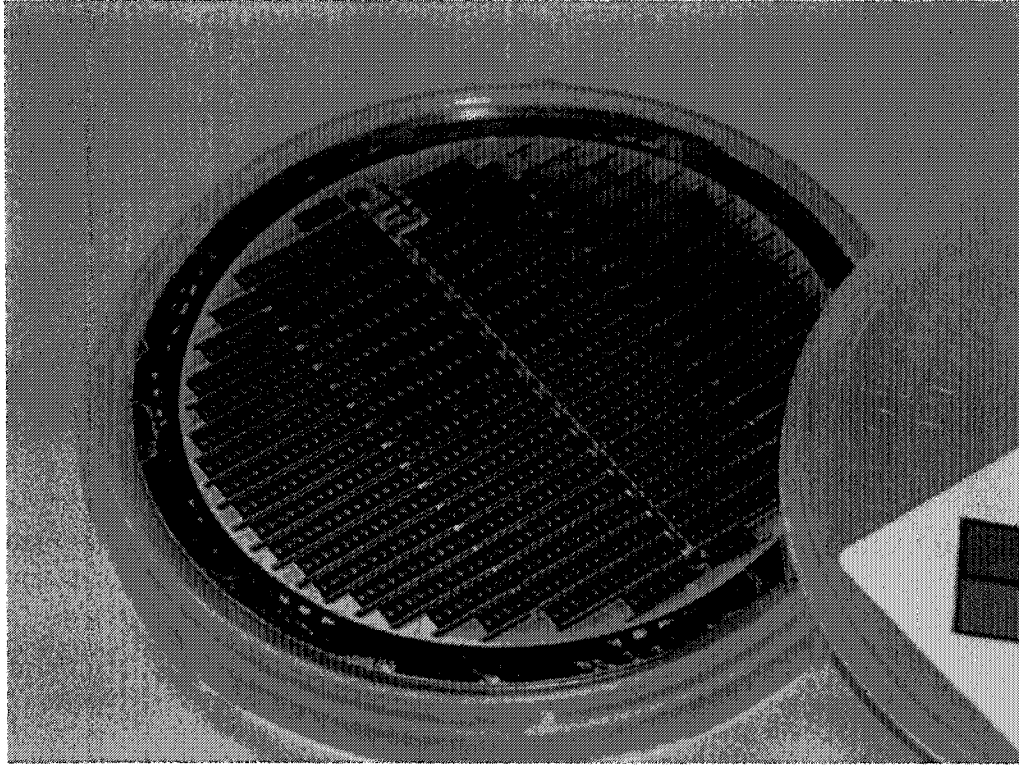


Figure 2-20 Picture of mass-produced $SiO_2$ microcantilevers taken by Olympus digital camera.
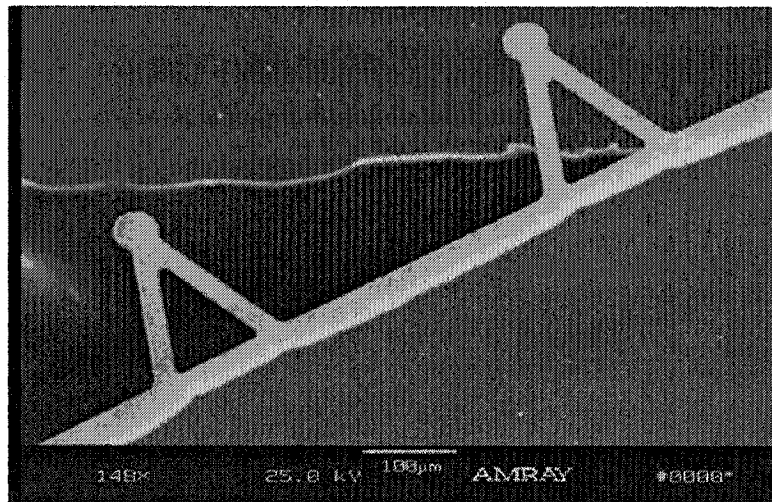


Figure 2-21 Scanning Electronic Microscopy image of fabricated $SiO_2$ microcantilevers taken by AMARY SEM.

A



B



C



D
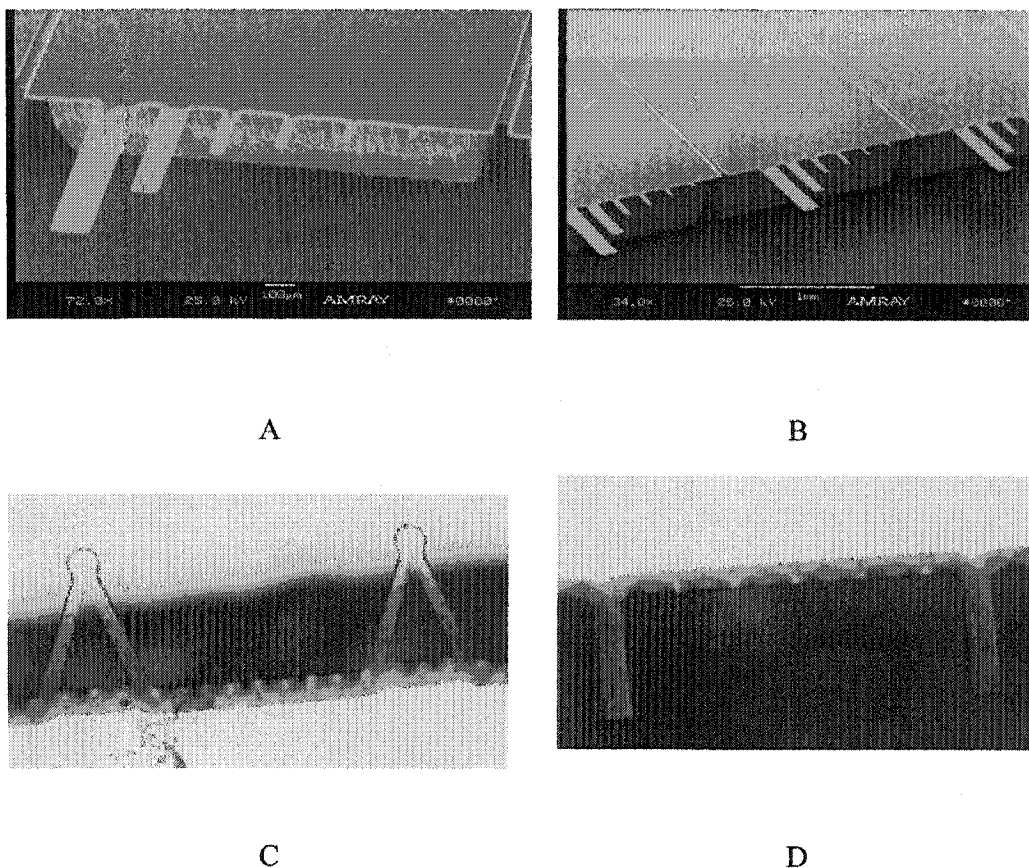
Figure 2-22(A), (B), Rectangular microcantilever array(C),
(D), Microcantilever images under optical microscopy.

Compared with many current silicon chemical etching methods, such as KOH or

EDP silicon wet etching, dry plasma etching can offer many advantages in the fabrication

of MEMS because of its anisotropic (i.e. independence of silicon crystal orientation)

etching behavior, high etch rate, and its compatibility with traditional IC processing. With

optimization, the etch uniformity would be better than +/- 5%. Si:Photoresist selectivity

was up to 50:1, which enabled 20μm photo resist AZ9260 to be the masking for silicon

deep dry etching. Si:SiO$_2$ selectivity was up to 350:1, which was a distinct advantage to

release clean and integrated SiO$_2$ cantilever beams from bulk silicon. In our process, flow

rate of etchant gas SF$_6$ was 300 sccm and that for passivation gas C$_4$F$_8$ was 200 sccm. The

silicon dry etching rate was about 5μm/min, and about 100 minutes were needed to released microcantilever beams from Si. The silicon-etching rate was nearly 10 times faster than wt. 40% KOH silicon wet chemical etching. In practice, we found wt. 40% KOH silicon wet chemical etching rate was 0.5 μm/min at the temperature of 80°C. In addition, silicon plasma dry etching gave much better control on the cantilever length since it produced deep vertical sidewall. While in a wet chemical anisotropic (i.e. dependence of silicon crystal orientation), the cantilever length varied due to the wafer thickness variation.

KOH wet etch of silicon was initially used to release $SiO_2$ microcantilevers from bulk silicon. Due to the low etch rate and low $Si/SiO_2$ selectivity of KOH silicon etch, the $SiO_2$ pattern was badly damaged when releasing $SiO_2$ microcantilever beams from bulk silicon (Figure 2-23)
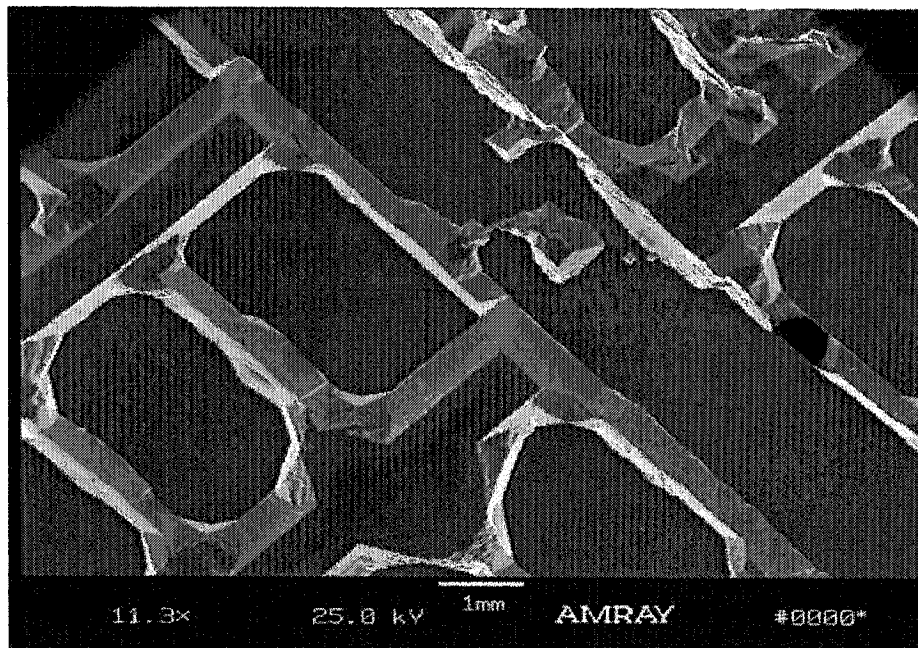


Figure 2-23 Damaged pattern in KOH silicon wet etching.

Figure 2-24 Damaged pattern in KOH silicon wet etching.

2.3.3 Fabrication of Piezoresistive Microcantilevers

The piezoresistive microcantilever was designed and fabricated to detect chemical and biological agents. 3μm wide and 400 μm thick Au resistor will be deposited and patterned on cantilever beam by LOR lift-off process. Also, Au resistor and metal wire process must be compatible with $SiO_2$ the cantilever process to produce piezoresistive $SiO_2$ cantilever.

●Designed piezoresistive microcantilever

The following figure (Figure 2-25) is the designed piezoresistive microcantilever. The microcantilever beam is made of $SiO_2$ material. Piezoresistive microcantilever fabrication is based on the previous $SiO_2$ microcantilever fabrication.

●Fabrication flow

The fabrication process started with 500 μm thick si wafer with 1 μm thick $SiO_2$ grown on both sides. (Figure 2-26) 2μm wide Au resistor was patterned on $SiO_2$ layer by LOR lift-off processing. (Figure 2-27) And, metal wire and electrodes were patterned by

LOR lift-off processing too. (Figure 2-28) Then, microcantilever pattern was transferred

to SiO₂ layer by standard lithography process. (Figure 2-29) Finally, microcantilever

support was patterned on back-side using AZ9260 photoresist, and piezoresistive

microcantilevers were released from bulk silicon wafer. (Figure 2-30)
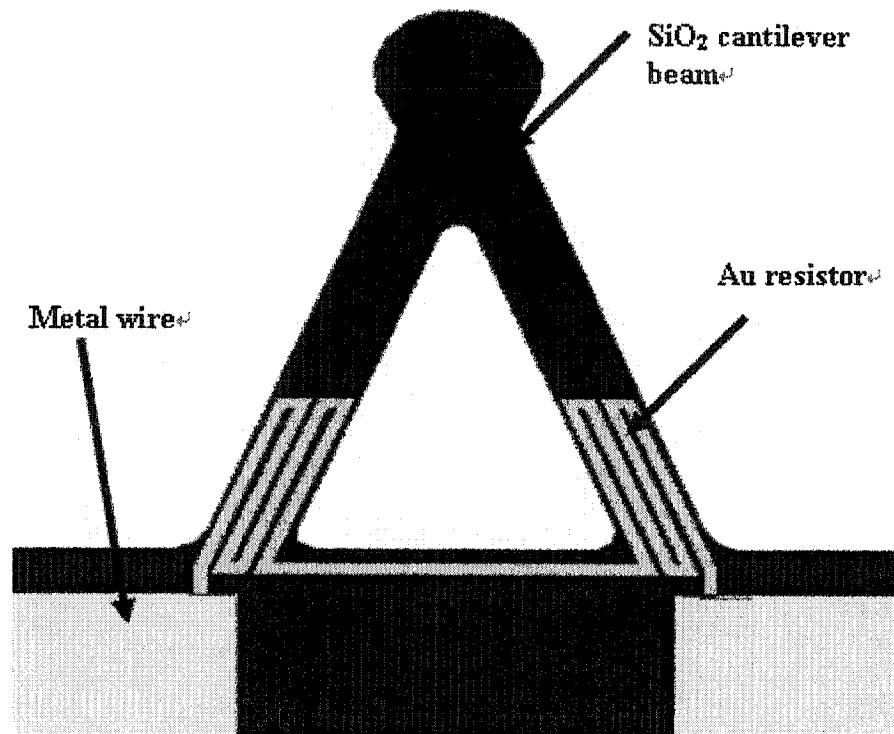
Figure 2-25 SiO₂ piezoresistive microcantilever.
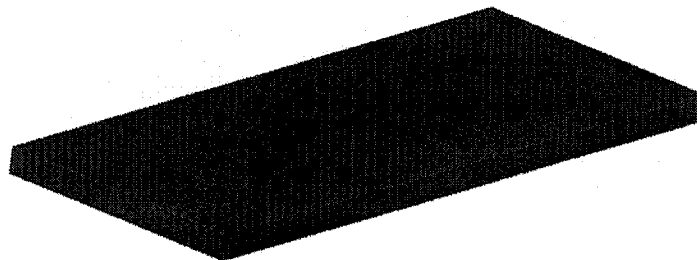
Figure 2-26 500μm thick silicon wafer with 1μm
SiO₂ film on both sides.
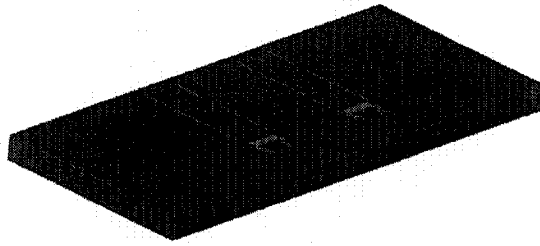
Figure 2-27 2μm Au resistor patterned by LOR lift off process.
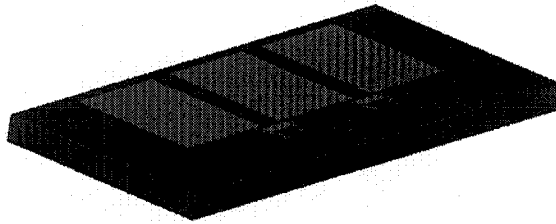


Figure 2-28 Chrome wire patterned by LOR loft off process.
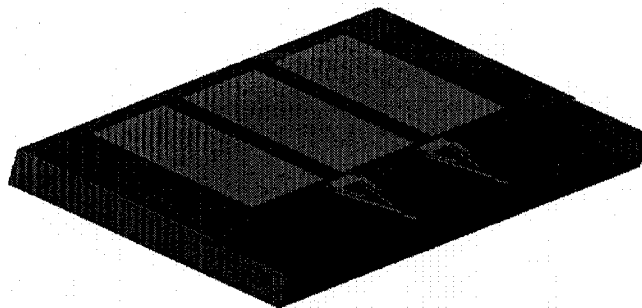


Figure 2-29 Microcantilever beams were patterned on SiO₂ layer
using lithography process.
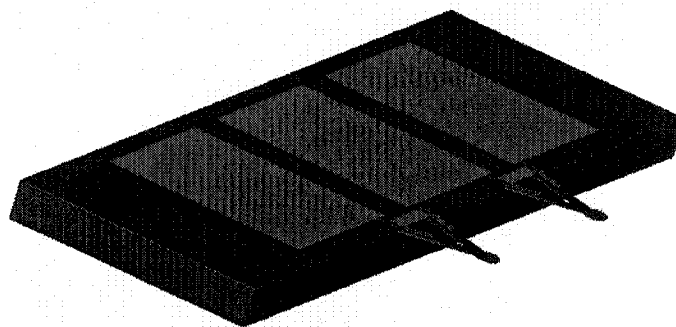


Figure 2-30 SiO₂ microcantilever beams were release by ICP
Silicon plasma dry etching process.

Result and Discussion. $SiO_2$ piezoresistive microcantilevers were successfully fabricated.
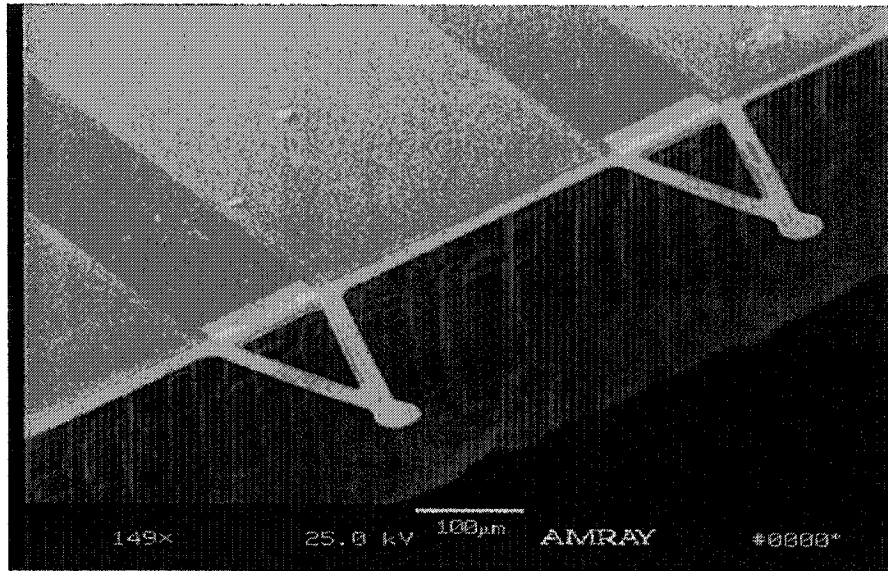


Figure 2-31 Scanning Electronic Microscopy (SEM) image
of fabricated $SiO_2$ piezoresistive microcantilevers.
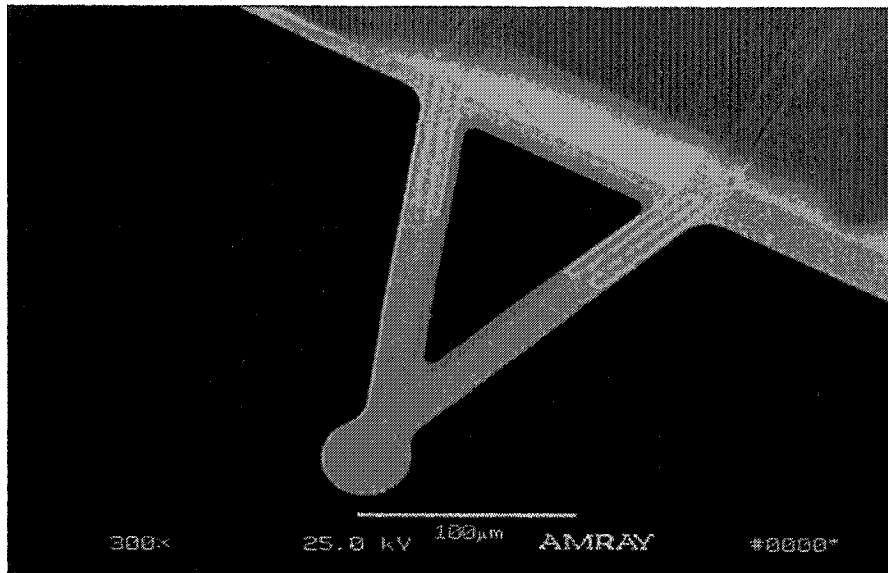


Figure 2-32 Scanning Electronic Microscopy (SEM) image
of fabricated $SiO_2$ piezoresistive microcantilevers.

Using LOR lift-off photoresist and the process described in Section 2.2.4.2, satisfactory undercut photoresist profile was developed (Figure 2-33) and Au resist pattern was obtained with satisfactory fidelity (Figure 2-34).
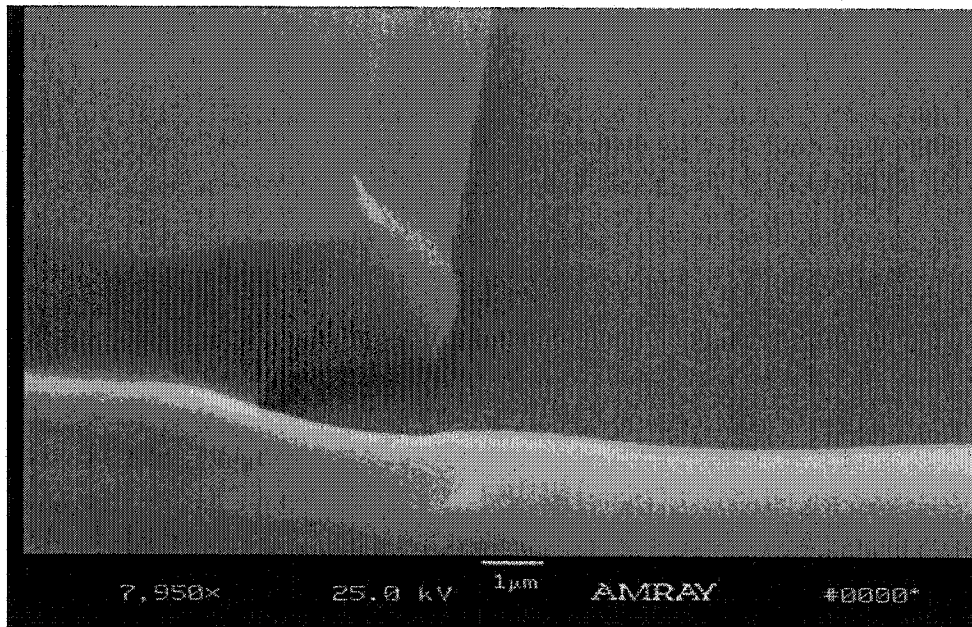
Figure 2-33 Undercut photoresist profile by using LOR lift-off photoresist.

Chlorobenzene lift-off process was initially used to pattern Au resist and thin layer of Ti was deposited underneath Au film to enhance adhesion of Au to substrate. Ti film is thought to give much stronger adhesion to thin film than chrome thin film does.

Chlorobenzenene lift-off process was used to pattern Au resistor. After coating with photo resist Shipley 1813 and exposed, the wafer is soaked in chlorobenzene for a while. Chlorobenzene leaches out low molecular weight polymers from the surface of the resist, thus hardening the material. The hardened material is less likely to be developed by developer. Undercutting profile is then formed in the photo resist layer. An undercutting profile is critical for the lift-off process.
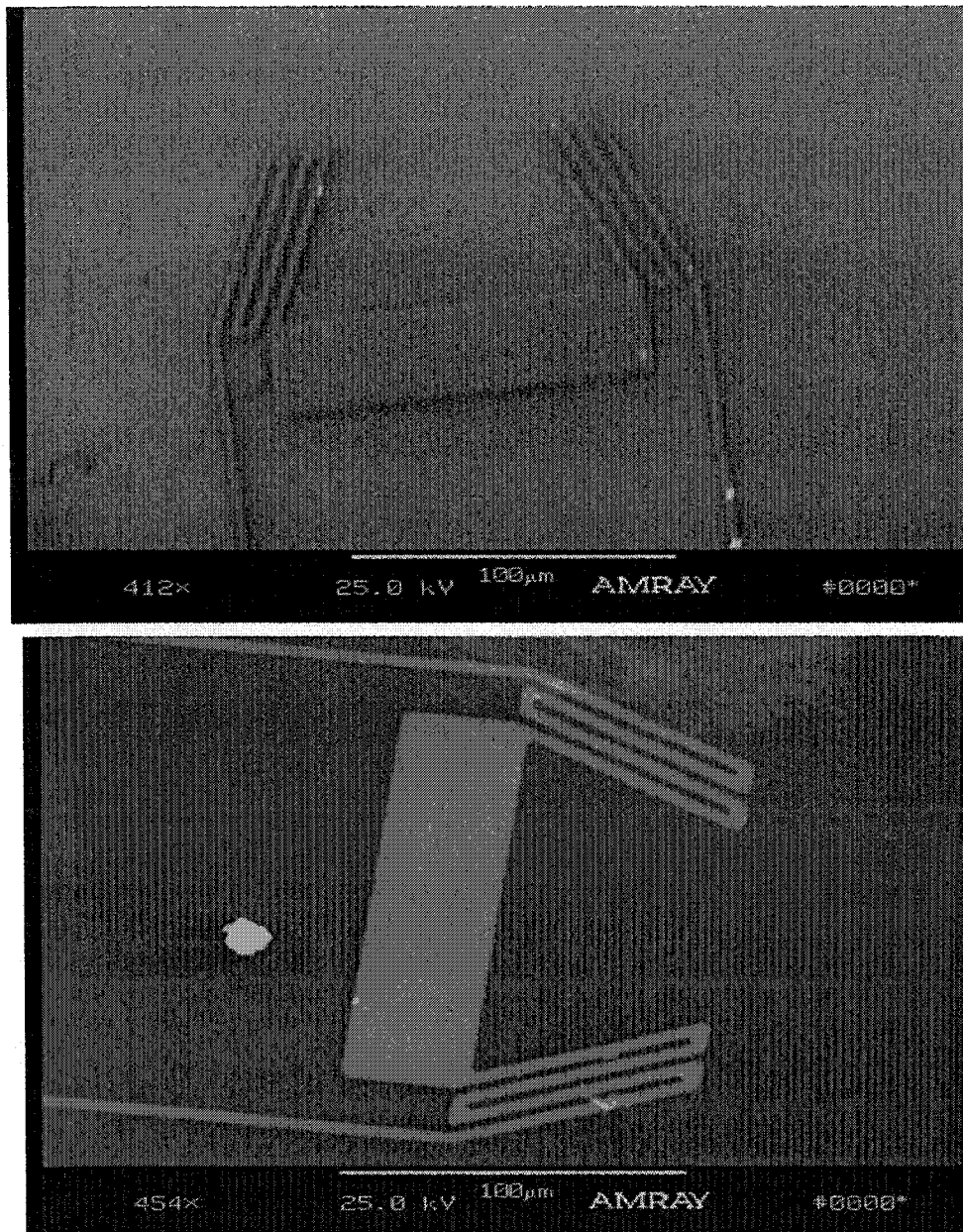
Figure 2-34 The Au resist pattern by using LOR lift-off photoresist processing.

In process, Au resist pattern was deposited and patterned by chlorobenzen lift-off process first and metal wire pattern was to be deposited and patterned by the same process. However, after the wafer coated with photo resist is soaked in chlorobenzene to obtain the undercut photoresist profile, Au resist was found peeled from substrate (Figure 2-35).
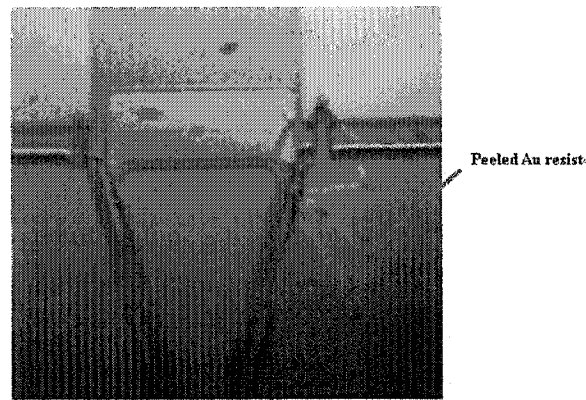
Figure 2-35 Peeling of Au resistor after soaking in chlorobenzene.

A 250 thick Ti layer is deposited underneath the Au thin layer to help Au adhere to

the wafer. (Figure 2-36) It is concluded from analysis that chlorobenzene corrodes Ti and

hence makes the Au resistor lose adhesion to the wafer and then distort the pattern.
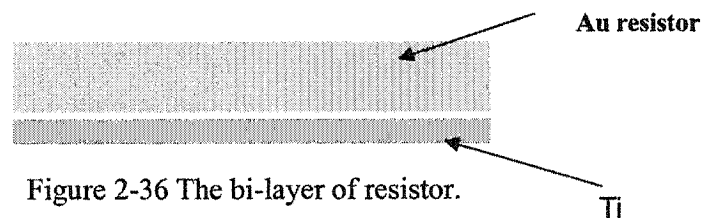


Figure 2-36 The bi-layer of resistor.

Detailed observation of the connection enhances the analysis. It can be seen that the

edge all around the connection has different color from the middle of connection. This

means that the Ti underneath the edge has been corroded by chlorobenzene (Figure 2-37).
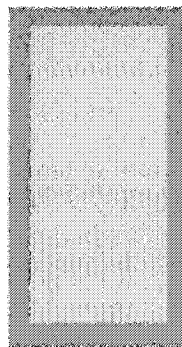


Figure 2-37 The corroded connection structure.

In the lift-off process, it was also found that ultra sonic vibration was helpful to completely and clearly release photoresist. Figure 2-38 shows the residual photoresist which is a common problem in the lift-off process.
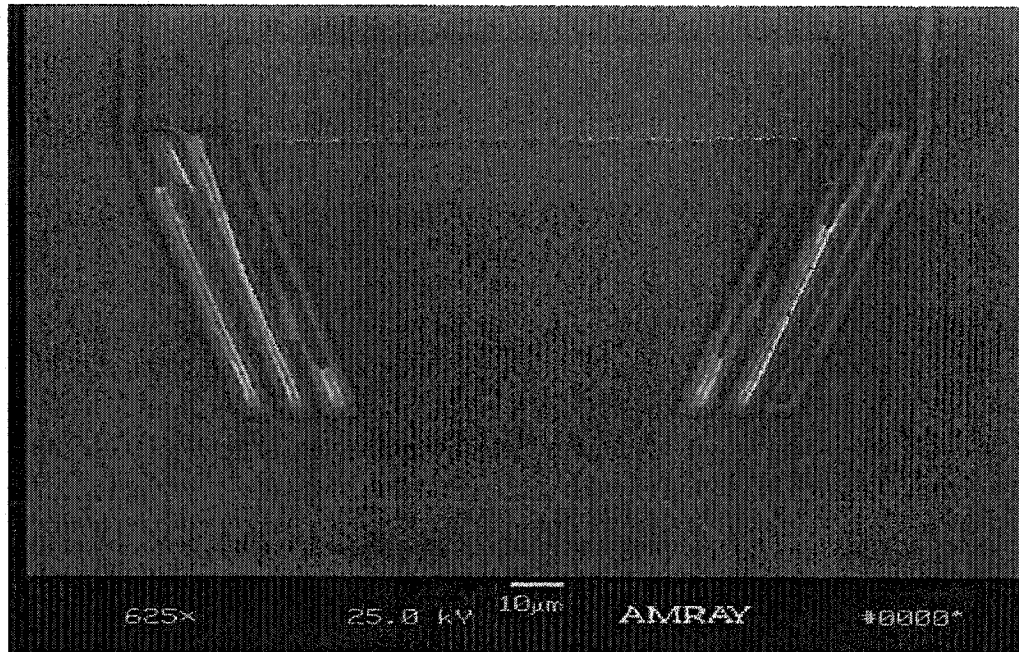


Figure 2-38 Residual photoresist in lift-off process.

## 2.3.4 Fabrication of Polymer Microcantilevers

SU-8 5 negative tone photoresist was used to fabricate polymer microcantilevers due to its ultra low Young's modulus. The fabrication process is compatible with that of $SiO_2$ microcantilever. Microcantilever beams were firstly patterned on SU-8 layer by standard photolithography process. Then, microcantilever support was patterned on AZ9260 photoresist layer on backside. Finally, polymer microcantilever beams were released from bulk silicon by ICP plasma silicon dry etching. Figure 2-39 shows fabricated SU-8 microcantilevers.
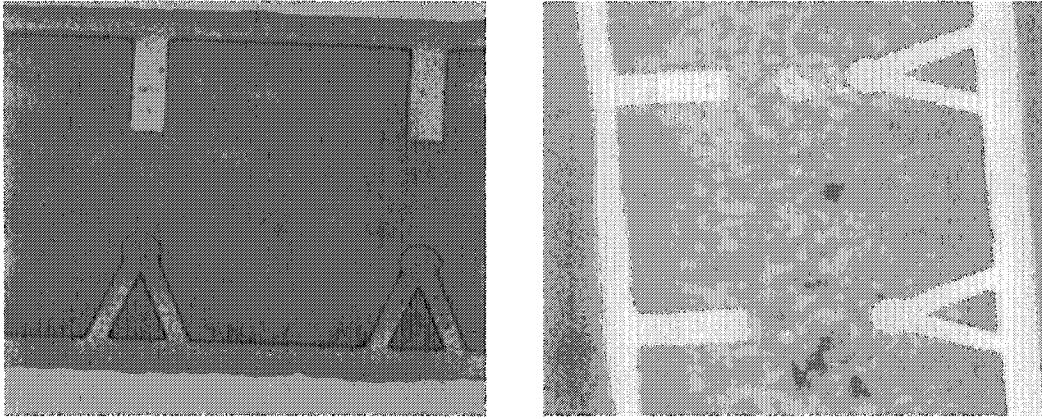
Figure 2-39 Fabricated SU-8 microcantilevers.

# CHAPTER THREE

# CHARACTERIZATION OF FABRICATED

# MICROCANTILEVERS

Whether microcantilevers perform either as AFM probes or sensors depends on their mechanical properties. Cantilever measurement or sensing both are reflected by its bending. The Cantilever's spring constant must be first characterized to assess cantilever bending. For a rectangular cantilever, its spring constant can be calculated by

$$\kappa = \frac{Ewt^3}{4L^3}$$

(3.1)

where t is thickness, w is width of cantilever, L is the length of microcantilever, $\kappa$ is spring constant, and E is the Young's modulus of cantilever material. For a V-shaped cantilever, the spring cantilever can be calculated by parallel beam approximation. It is also valid to assess cantilever's spring constant by comparing this cantilever with a cantilever of known force constant as a reference cantilever[46,48,2]. A $SiO_2$ microcantilever was measured as 0.104M/N [2]. Similarly, an atomic force microscopy probe was used to determine the micromechanical properties of thin films. Spring constant of microcantilever was also measured by thermal fluctuation method. The result has good agreement with that of the Sader method[49,57,58]. A nanoindentation system was also used to measure Young's modulus of the microcantilever[56].

70

Besides the characterization of normal spring constant, Feiler *et al.* used a direct one-step technique to measure the torsional spring constant of the cantilever used for lateral or friction measurement with the atomic force microscope. Sader[60] investigated the premise that V-shaped cantilevers are used widely due to their enhanced resistance to lateral forces in comparison to rectangular cantilevers. V-shaped AFM cantilevers are generally more prone to the effects of lateral forces than rectangular AFM cantilevers. This finding suggests that rectangular cantilevers should be used in place of V-shaped cantilevers in applications where the effects of lateral forces are minimized.

The microcantilever's mechanical properties such as dynamic character, Kundsen forces, resonance frequency, thermal vibration, and fatigue strength were investigated. Marinier *et al.*[60] used a Michelson interferometery to measure dynamic characterization of $SiO_2$-Au microcantilevers. Passian *et al.*[61] investigated the Knudsen forces on microcantilevers, which exists when two surfaces at two different temperatures are separated by a distance comparable to a mean-free path of the molecules of the ambient medium. Hirai *et al.*[64] studied microcantilever resonance frequencies in air, water, and acetone. It is demonstrated that the resonance frequencies in water decrease to about one-tenth of the values in air. The string of beads model is one of the popular models for analyzing the drag force of a vibrating microcantilever. Muralidharan *et al.*[64] investigated how to enhance the small amplitude of thermal vibration of cantilevers typically used for atomic force microscopy and sensor applications. The fatigue strength of Ni-P amorphous alloy microcantilever beams was determined to be approximately one-third of the static bending strength for the fatigue life curve[65]. Ding *et al.* [66]investigated the specimen size effect on mechanical properties of polysilicon microcantilever beams  measured by deflection using a nanoindenter. The rupture strength of each sample decreased with increasing the specimen effective volume and

surface area, but increased with increasing the surface-to-volume ration. Wilson *el al.* did

fracture testing of silicon microcantilever beams.    The fracture strength of the front side,

3.3GPa, is significantly greater than that of the backside 1.0GPa.

### 3.1 Characterization of Fabricated Microcantilever by Comparison with Calibrated Microcantilever

The spring constant of fabricated $SiO_2$ cantilever was measured to evaluate its

performance in chemical sensing.  Some method of cantilever spring constant

measurement was found in literature. The method of using a cantilever of known spring

constant as a reference cantilever to measure the spring constant of other cantilevers was

also commonly used. The silicon cantilever was taken as a reference cantilever, and its

spring constant was known as 0.26N/m. The silicon cantilever was horizontally placed on

a fixed substrate. Then, the fabricated $SiO_2$ cantilever was also horizontally placed on a

fixed substrate while it had a different altitude level from that of the silicon cantilever.

The $SiO_2$ cantilever beam was placed into contact with the tip of the silicon cantilever

beam. (Figure 3-1) Both cantilevers deflected due to the touch force between them. The

magnitude of forces applied on the two cantilever beams was the same while their

directions were opposite.    From the equation

$$Z = (1/\kappa)\,F \tag{3.2}$$

while Z is deflection of the cantilever at the end and F is the force applied at the end, we

can see that cantilever' deflection is inversely proportional with its spring constant.

From Figure 3-1, the deflection of the silicon cantilever tip is about 40μm. The deflection

of $SiO_2$ cantilever is 101μm. Therefore, the spring constant of the $SiO_2$ cantilever can be

approximated as

$$\frac{40\mu m}{101\mu m} \times 0.26 \,{}^{N}\!/\!_{m} = 0.104 \,{}^{N}\!/\!_{m} \tag{3.3}.$$

From this, we estimated the spring constant of the fabricated cantilever is 0.104N/m,

and it is about 1/2.5 that of reference silicon cantilevers.
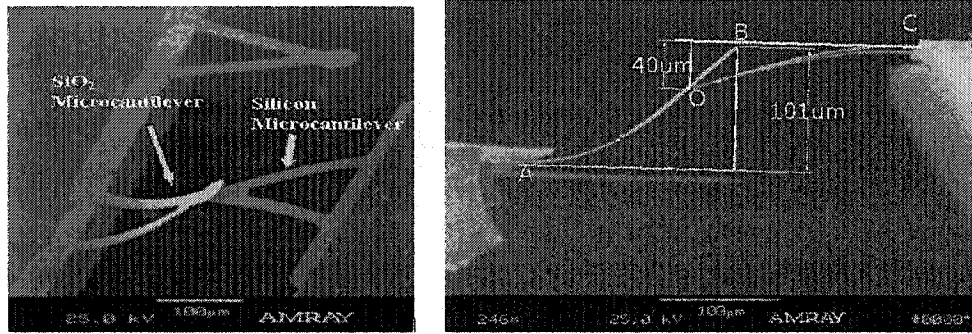


Figure 3-1 Measurement of SiO$_2$ cantilever spring constant.

To study the deflection of both cantilevers, we approximate the mechanical behavior

of the original V-shaped cantilever with a rectangular cantilever that has the same

cantilever length and its width is double the skewed arm width of original V-shaped

cantilever. The rectangular cantilever has the same thickness with the V-shaped cantilever.

The deflection at the end of the rectangular cantilever can be expressed as

$$\Delta Z = \left( \frac{3(1-\upsilon)L^2}{Et^2} \right) \delta s \tag{3.4}$$

where $\Delta Z$ is the observed deflection at the end of cantilever, $E$ is Young's modulus. $\upsilon$

is Poisson's ratio, t is the thickness of the cantilever, L is the length of the cantilever, and

$\delta s$ is the differential stress on the cantilever.

And, the spring constant for a rectangular cantilever is

$$\kappa = \frac{Ewt^3}{4L^3} \tag{3.5}$$
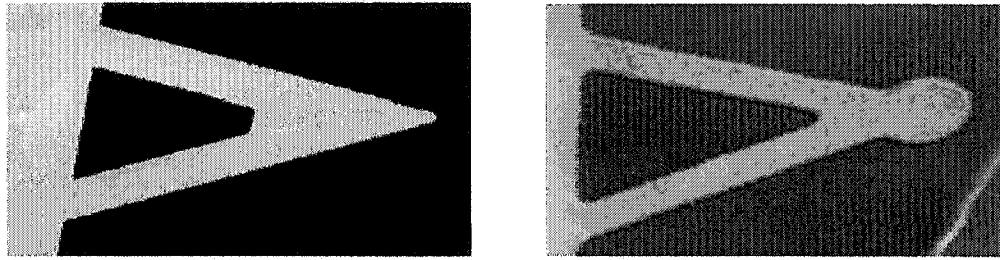
Figure 3-2 SiO$_2$ cantilever (left) and silicon cantilever (right).

The dimensions and mechanical properties of both cantilevers are shown in Figure

3.2 and Table 3-1.

Table 0-1 Comparison of SiO$_2$ cantilever and silicon cantilever

| Cantilever type | Cantilever length (μm) | Skewed cantilever arm width (μm) | Cantilever thickness (μm) | Cantilever spring constant (N/m) |
|---|---|---|---|---|
| SiO$_2$ cantilever | 200 | 25 | 2 | 0.104 |
| Silicon cantilever | 180 | 25 | 1 | 0.26 |

where $w$ is width of cantilever, and $\kappa$ is spring constant. The equation 3.5 is then derived

as

$$\Delta Z = \left( \frac{1}{\frac{Ewt^3}{4L^3}} \times \frac{3(1-\upsilon)wt}{4L} \right)\delta s = \frac{3(1-\upsilon)wt}{4L\kappa}\delta s \qquad (3.6)$$

From Table 3-1, the length ration of two cantilevers is 1.11. Poisson ratio of SiO$_2$ and

silicon ranges from 0.17 to 0.278. So the maximum ratio of item (1-v) between these two

.

cantilevers is 1.15. To simplify the analysis, we just assume these two ratios are 1's; i.e. both cantilevers have same values of lengths and Poisson ratios. Both cantilevers have very close geometry shapes and dimensions. In the following experiment, the differential surface stresses $\delta s$ were induced by chemical reaction between aminoethanethiol hydrochloride and the gold layer coated on one side of cantilevers. It is reasonable to assume that the surface stresses induced for both cantilevers are identical. Besides, both cantilevers have same width $w$ for skewed cantilever arms. Therefore, deflections of $SiO_2$ cantilever and silicon cantilever are only affected by their different spring constant $\kappa$ and thickness $t$. It is induced that cantilever deflection at the end is proportional with that ratio of cantilever thickness to cantilever spring constant

$$\Delta Z \propto \frac{t}{\kappa} \qquad (3.7)$$

From this relation, the relations of cantilever deflections in chemical sensing can be derived.

$$T_{SiO2} = 2T_{Si}$$

$$\kappa_{SiO2} = \frac{1}{2.5}\kappa_{Si}$$

$$\frac{\Delta Z_{SiO_2}}{\Delta Z_{Si}} = \frac{t_{SiO_2} \times \kappa_{Si}}{\kappa_{SiO_2} \times t_{Si}} = \frac{2t_{Si} \times \kappa_{Si}}{\frac{1}{2.5}\kappa_{Si} \times t_{Si}} \approx 5$$

It is expected that the deflection of $SiO_2$ cantilever is about 5 times of that of silicon cantilever in chemical sensing under identical conditions. Both $SiO_2$ cantilevers and silicon cantilevers were used to detect $10^{-5}M$ aminoethanethiol hydrochloride solutions.

Both cantilevers were coated with a thin layer of gold on one side to react with aminoethanethiol hydrochloride solution and reflect laser beams in the apparatus. From Figure3-3, the deflection of the silicon cantilever is about 90nm, while that for the $SiO_2$ cantilever is about 510nm. The deflection ratio of the $SiO_2$ cantilever to the silicon cantilever is about 5.6. The much bigger deflection of the SiO2 cantilever leads to much more sensitive detection in chemical sensing. The result shows the validity of proposed characterization.
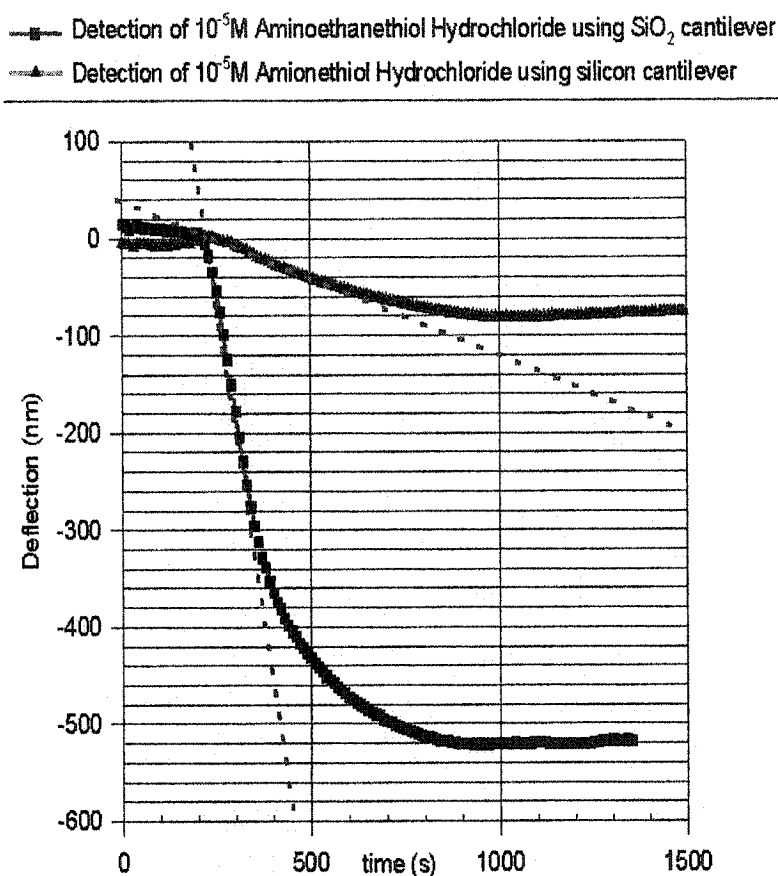


Figure 3-3 Bending comparison of $SiO_2$ and si microcantilevers.

## 3.2 Mechanical Characterization of Microcantilever by AFM Measurement

To test the validity of simulation, the spring constant of the fabricated microcantilever was also measured using an AFM probe. In the measurement, the probe

tip of the AFM was engaged onto the end of fabricated microcantilever (Figure 3-4). Further probe displacement caused the deflection of the probe tip. Both microcantilever and probe were end-loaded by some amplitude of forces, and the forces caused the deflections of probe and cantilever.
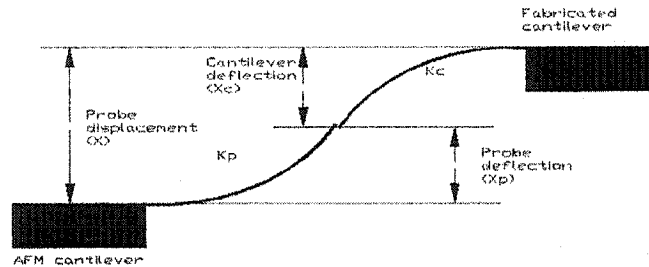


Figure 3-4 The deflections of AFM probe and fabricated
microcantilever when probe is engaged onto the end
of fabricated microcantilever.

It is assumed that the spring constant of probe is $K_P$, which is known as 0.25N/m, and that for fabricated is $K_C$. In Figure 3.4, the probe displacement is the summary of cantilever deflection $X_C$ and probe deflection $X_P$.

$$X = X_P + X_C \tag{3.8}$$

From the equation

$$X = (1/\kappa) F \tag{3.9}$$

Where X is deflection of cantilever or probe at the end, and F is the force applied at the end. The deflections are inversely proportional with spring constants. The following equation was then derived

$$X_P = \frac{K_C}{K_C + K_P} X \tag{3.10}$$

In the elastic part of AFM approach curve (Figure 3-5), when probe displacement is 0.8nm, the probe deflection is 0.23nm. Then from the equation 3.10, it was calculated that spring constant of fabricated microcantilever KC is 0.101N/m, which valid the comparison analysis of mechanical properties.
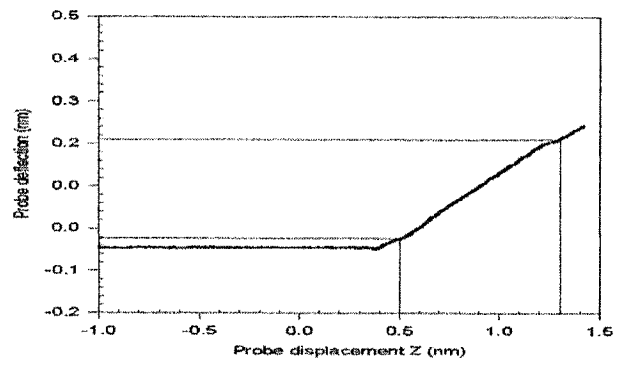
Figure 3-5 AFM approach curve.

# CHAPTER FOUR

# MEASUREMENT EQUIPMENT AND PROCEDURE

There are different methods to measure deflection of microcantilevers when microcantilevers are used as chemical and biological sensors. In this chapter, the equipments and procedures for optical is introduced.

## 4.1 Optical Method

### 4.1.1 Equipment

4.1.1.1 Microcantilever Detection Equipment Setup. A microcantilever is held in a flow-through glass cell. (Figure 3-1) The flow rate of the analyte solution can be controlled by a injection pump. The switch of the solution is realized by a six-port valve. The volume of the glass cell is small enough (0.3ml) to ensure fast replacement of the liquid in contact with cantilever. An optical detection unit is used for the measurement of the deflection of the microcantilever. A laser beam is reflected off the top of the microcantilever onto a four-quadrant photodiode. The position change of this laser beam can be measured sensitively(Figure 4-2).

79
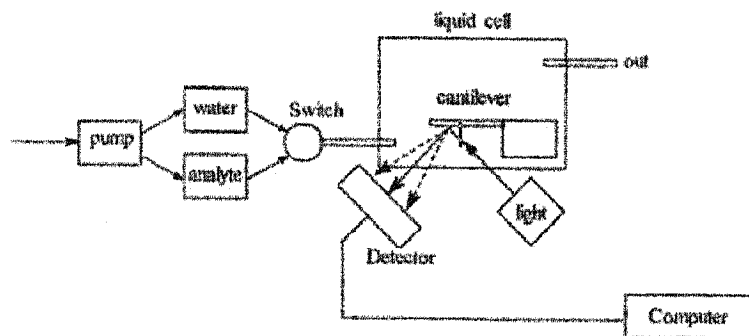
Figure 4-1 Schematic representation of the instrument showing
the method for measuring cantilever deflection and
the scheme for introducing solution into the cell.
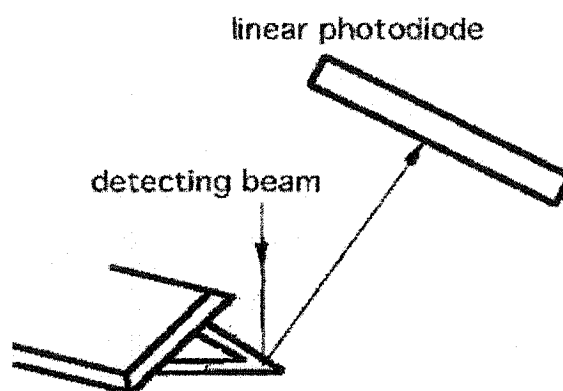


Figure 4-2 Optical measurement of microcantilever deflection.

The commercial unit that combines the laser system, microcantilever holder and optical detector was used for the experiment. The cantilever and the experimental setup were the same as those reported previously.

4.1.1.2 Microcantilevers The fabricated $SiO_2$ microcantilever and commercially available silicon microcantilever are used for the experiment. For commercial silicon microcantilever, the size is 200 μm long, 40 μm wide, and 1 μm thick. For fabricated microcantilevers, detailed mechanical characteristics can be found in Chapter 3 of this dissertation. A 20nm thin film of gold was coated on one side of the microcantilever.

## 4.1.2 Measurement Procedure

Once the cantilever was mounted into the liquid cell, it was initially exposed to a constant flow of buffer, and the cantilever was equilibrated until a stable baseline was obtained. The bending of microcantilever was read by the optical detection system.

# CHAPTER FIVE

# DETECTION OF FEMTOMOLAR

# CONCENTRATION OF HF USING

# THE FABRICATED SiO$_2$

# MICROCANTILEVERS

### 5.1 Introduction

The threat posed by nerve agents has made them important targets for detection.

Fluorine is a major component in many nerve agents, including sarin and soman. Nerve

agents decompose quickly in alkaline conditions. After decomposition, the nerve agents

release hydrogen fluoride (HF) or F$^-$ into the solution. Simultaneous identification of HF

or F$^-$ and organophosphorus is a very helpful and reliable way to detect the existence of

nerve agents. Furthermore, detection of HF is important itself because HF is highly toxic.

Exposure to HF can cause injury through inhalation, direct contact, or ingestion. Airborne

fluorides have caused more worldwide damage to domestic animals than any other air

pollutant. HF is used industrially in large quantities throughout the United States (over

200,000 tons per year) and in a great number of applications across a broad range of

industries (over 500 facilities) [114]. HF serves as a major feedstock and source of the

fluorine atom for the production.

82

Fluorocarbon manufacture consumes 63 percent of the total HF used. HF is also used as an alkylation catalyst for the production of gasoline blending components. Other uses include aluminum production and semiconductor applications.

Analytical methods employed currently to measure HF in the industrial environment include the infrared (IR) spectroscopic method [72-112], electrochemical methods[114], ion mobility spectrometry, interferometry, and solid state metal oxide or semiconductor gas sensors. The IR spectroscopic method requires instrumentation that is bulky, expensive, and complex, and therefore not suited to the *field* analysis of multiple samples. Other sensing devices are excellent for real-time, in-field analysis of HF at parts-per-million (ppm) level. They are appropriate for detection of leaking HF. However, the sensitivity of these systems is not sufficiently high for detecting and monitoring HF at part-per-billion or lower concentrations.

We have used fabricated $SiO_2$ microcantilever for the detection of HF because of the characteristic reaction of HF with $SiO_2$. HF selectively reacts with $SiO_2$ as shown in the following reaction, which has been widely used in the silicon industry.

$$\text{-O-Si-O- + 4HF} \rightarrow \text{SiF}_4 + 2\text{H}_2\text{O} \tag{5.1}$$
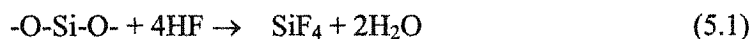
This is a very characteristic reaction. Several current devices, such as the Shur-Shot™ HF detection system (Molecular Analytics Inc.) and for HF measurement are also based on this reaction (either in air or solution). Other acids, such as HCl and $H_2SO_4$, do not react with $SiO_2$.

## 5.2 Experiment

### 5.2.1 Solvent and Materials

We used the fabricated $SiO_2$ microcantilever as well as commercially available silicon microcantilevers (Veeco Instruments, CA). The dimensions of the V-shaped silicon microcantilevers were 180 μm in length, 25 μm in leg width, and 1 μm in thickness. One side of these cantilevers was covered with a thin film of chromium (3 nm) followed by a 20-nm layer of gold, both deposited by e-beam evaporation. On the uncoated side of the commercial microcantilever was silicon with a 12-to-19-Å thick naturally grown $SiO_2$ layer, which is called "native oxide" [114]. The dimensions of the fabricated V-shaped $SiO_2$ microcantilevers were 200 μm in length, 25 μm in leg width, and 2 μm in thickness. One side of the $SiO_2$ cantilevers was covered with a 3-nm of chromium/20-nm of gold as well.

The chemicals used in these experiments, including HF, KF, and HCl, were used as received from Aldrich. High-purity deionized water was obtained with a Milli-Q water system (Millipore). The pH of the deionized water was 6.90.

### 5.2.2 Deflection Measurement

The deflection measurement is describe in Section 4.1 of Chapter 4. Because a change in the flow rate would have created turbulence and thus would have induced noise in the cantilever bending signal, a constant flow rate of 3 mL/h was maintained during the entire experiment. Experimental solutions containing different concentrations of HF and the analytes of interest were injected directly into the slowly flowing fluid stream via a low-pressure injection port sample loop arrangement. This arrangement allowed for continuous exposure of the cantilever to the desired solution without disturbing the flow cell or changing the flow rate. Since the volume of the glass cell, including the tubing, was only 0.3 mL, a relatively fast replacement of the liquid in contact with the cantilever was achieved.

A new cantilever was used for each deflection measurement. Measurements were carried out by the optical beam deflection method. Cantilever bending was measured by monitoring the position of a laser beam reflected from the gold-coated side of the cantilever onto a four-quadrant AFM photodiode. We refer to bending toward the gold side as "bending up"; "bending down" refers to bending toward the uncoated side. The cantilever was immersed in deionized water until a stable baseline was corresponding to 0 nm.

## 5.3 Results and Discussion

When solutions containing various concentrations of HF were injected into the fluid cell, the microcantilever bent down (towards the uncoated $SiO_2$ side) with different amplitudes as shown in Figure 5-1. Deflection increased as the concentration of HF increased. For each measurement, a 2.0-mL aliquot of HF solution was injected into the fluid cell. It took 40 minutes for the injected HF solution to flow through the fluid cell, and which time the deionized water was circulated back into it. While the concentration of HF was constant in this 40 minute window, the microcantilever deflection rate gradually decreased. This decrease may be due to the diffusion control of the reaction. Both HF consumption and $SiF_4$ accumulation near the $SiO_2$ surface could decrease the reaction rate.
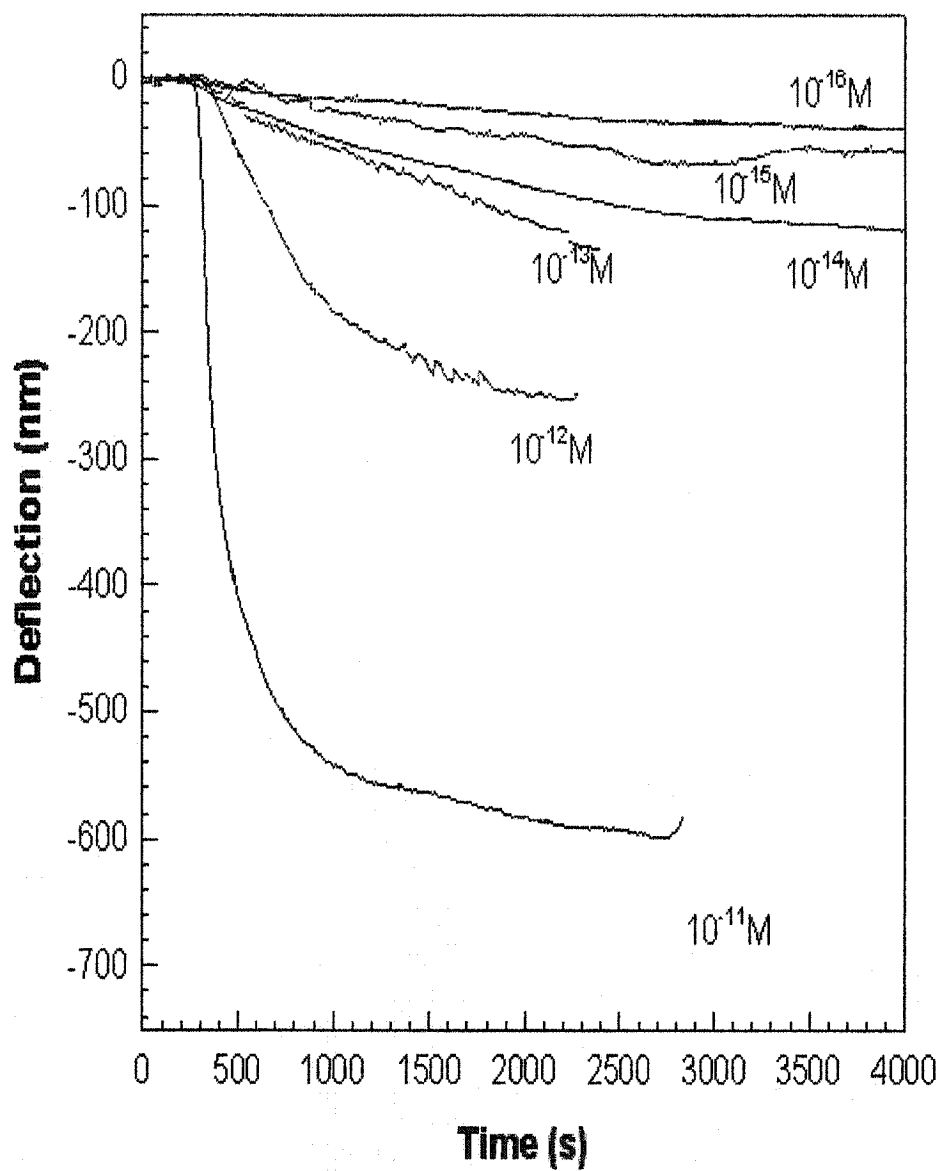
Figure 5-1 Bending response as a function of time, $t$,
for $SiO_2$ microcantilevers after injection of
different concentrations of HF solutions.

Figure 5-2 is a plot of the deflection rate in the first 5 minutes after injection of HF solutions versus HF concentration. The rate of bending was a function of the HF concentration. At higher HF concentration, the cantilever bent down faster. The increase in deflection rate of HF with $SiO_2$ can be accounted for by assuming a higher reaction rate at high HF concentrations.
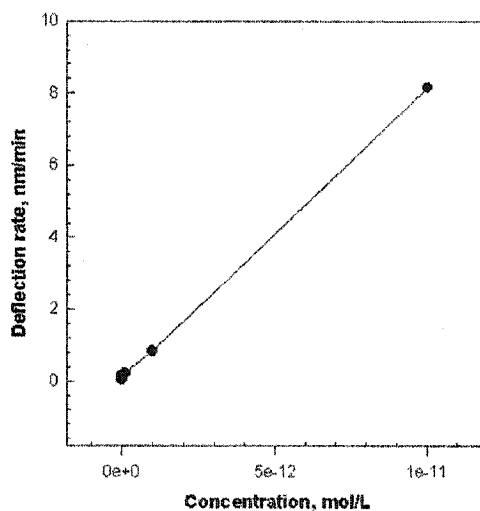
| M | -11 | -12 | -13 | -14 | -15 | -16 |
|---|---|---|---|---|---|---|
| Nm | 750 | 730 | 230 | 180 | 100 | 60 |
| min | 3.333 | 42.5 | 66.66 | 66.66 | 66.66 | 66.66 |
| Nm/min | 225 | 17.17 | 3.45 | 2.7 | 1.5 | 0.9 |

Figure 5-2 Deflection rate of a $SiO_2$ microcantilever
as a function of HF concentrations.

Exposure of the $10^{-11}$ M solution of HF to two new $SiO_2$ microcantilevers fabricated using the same procedure caused similar deflection amplitudes and bending rates, as shown in Figure 5-3. The standard error was within 5%, indicating good cantilever-to-cantilever reproducibility.
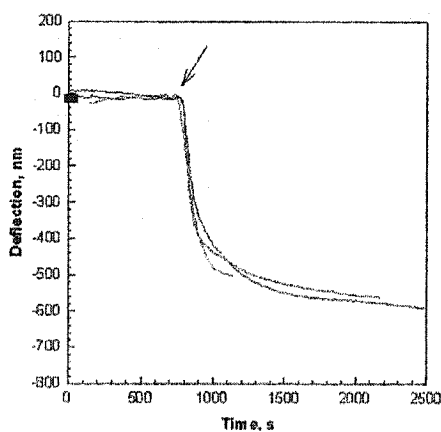


Figure 5-3 Reproducibility of the response of three
independent $SiO_2$ microcantilevers.

Repetitive injection of HF to the same cantileveralso showed reproducible cantilever deflections (Figure5-5).
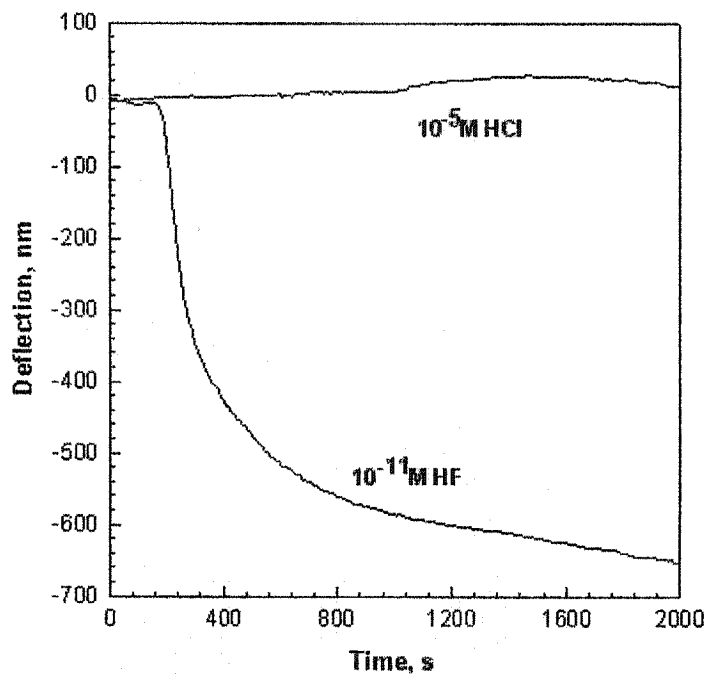


Figure 5-4 Bending responses as a function of time, $t$, for two $SiO_2$ microcantilevers.

Control experiments were performed by exposing a $SiO_2$ microcantilever to a $10^{-5}$ M solution of HCl. No deflection of the cantilever was observed (see Fig 5-4). In addition, stability experiments were conducted on microcantilevers after 5 months of storage in air. The deflection of the stored cantilevers showed a similar profile and bending amplitude as those in Figure 5-1

After injection of a $10^{-11}$ M HF solution and a $10^{-5}$ M HCl solution, respectively. The microcantilevers were pre-equilibrated in the water before injection of the HF and HCl solution.
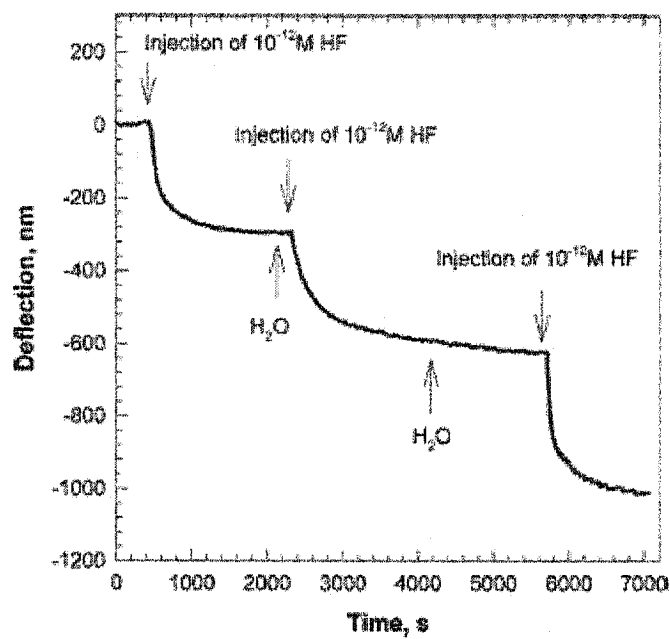
Figure 5-5 Reproducibility of the response of a SiO₂
microcantilever upon repetitive injection of a solution
of $10^{-12}$ M HF. The injection points are
indicated with arrows.

Figure 5-6 is a plot of the deflection amplitude recorded at specific times after

injection (300, 600, 1500, and 2700 s) versus the concentration of HF. The plot shows

that this microcantilever can be used for the detection of HF at concentrations as low

as $10^{-16}$ M. Better sensitivity can be achieved with increased exposure time after

injection. The maximum HF concentration in our experiments was at $10^{-11}$ M, the

effects of differences in ionic strength and pH at different HF concentrations can be

neglected.

Based on our observations, we concluded that the microcantilever deflection was

due to a reaction between the surface oxide layer and HF that induced a change in

cantilever surface stress. Because SiF₄ was soluble in water, it diffuses from cantilever

surface after the reaction.
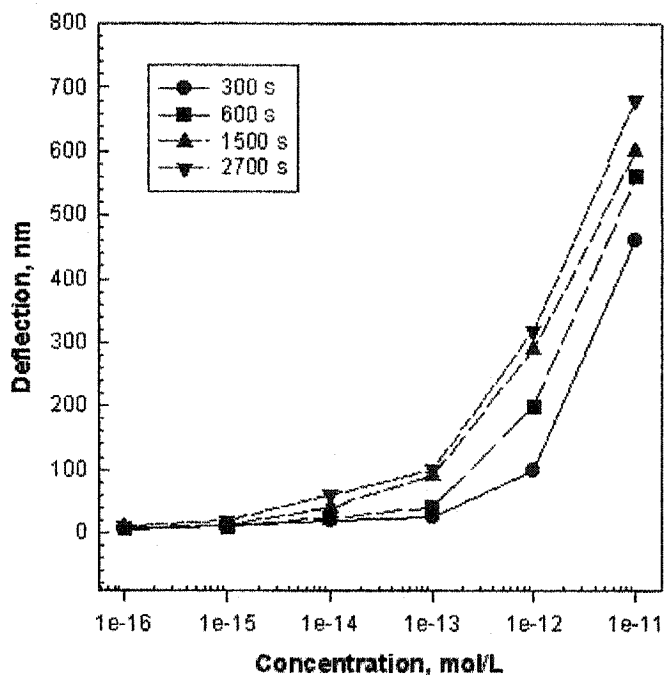
Figure 5-6 The deflection of an SiO$_2$ cantilever as a function of
the concentration of HF.

In silicon chemistry, it was widely understood, based on empirical results, that the

SiO$_2$ etching rate is direct proportional to the concentration of HF.

$$\text{Etching rate} = \text{k [HF]} \tag{5.2}$$

When a 49% HF solution is used, the etching rate of silicon oxide is 165 nm/min.

According to Equation 5.2, at the highest HF concentration ($10^{-11}$ M) used in our

experiments, the etching rate was $7 \times 10^{-11}$ nm/min. After 30-min exposure to HF, 2

$\times 10^{-9}$ nm of SiO$_2$ layer of the cantilever was etched off; i.e., only a small amount of

surface SiO$_2$ reacted with HF. It is noted that these calculated results may not be

accurate because of the lack of literature reports on the etching rate at low HF

concentrations. However, in general, these data suggested that the HF/SiO2 reaction

on the microcantilever surface occurred at the molecular level, and the intermediate

reaction played major roles in microcantilever bending in our experimental conditions.

The initiating reaction is the fluoride absorption at the surface silicon atom: through a

process of inner sphere surface complexation (equation 5.3), and the Si-F bond polarizes the underlying Si-O bonds, leading to the release of silicon atoms from the surface (equation 5.4)..

$$\text{OH} \quad \text{Si} \quad + \text{ HF} \longrightarrow \text{Si} \quad + \text{ H}_2\text{O}$$

$$(5.3)$$

$$+ 3\text{H}_2\text{O} \longrightarrow + \text{Si(OH)}_3\text{F}$$

$$(5.4)$$
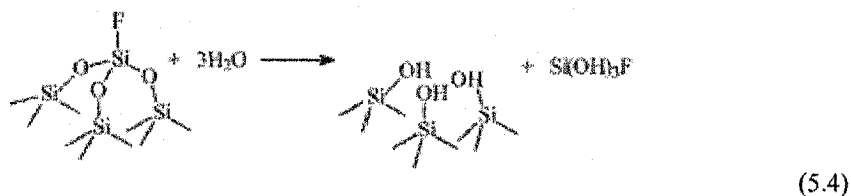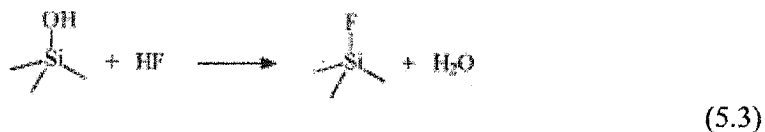
Based on these reaction models, the microcantilever downward bending is due to the replacement of Si-OH by Si-F (the Si-F moiety is smaller than Si-OH group) and the detachment of Si atoms from the surface that shrank the silicon surface of the microcantilevers after HF exposure. It is noteworthy to discuss the temperature effect on microcantilever bending. Based on our experiences, in general, the temperature changes due to chemical interactions between analytes in solutions and molecules on the microcantilevers can be neglected. This is mainly because the local heat generated by interactions can be quickly released in solutions, especially in a continuous flow system. Furthermore, the chemical interactions on the cantilever surface normally do not cause enough heat to bend the cantilever. For the first $SiO_2$ etching step, the reaction is endothermic. Since only a small amount of -Si-OH on the surface reacted with HF, the heat absorbed from the environment was negligible.

The deflection response to HF of commercially available silicon cantilevers was also studied and was compared with that of the $SiO_2$ cantilevers. Normally, a 12-to-19-Å thickness of $SiO_2$ grows naturally on the silicon surface and thus provide a reactant for HF. However, much less bending amplitude and sensitivity were observed

for the silicon cantilevers, as shown in Figure 5.7. These results may mainly be because of the higher spring constants of the silicon material (155.8 GPa) than that of $SiO_2$ (76.5-97.2 GPa).
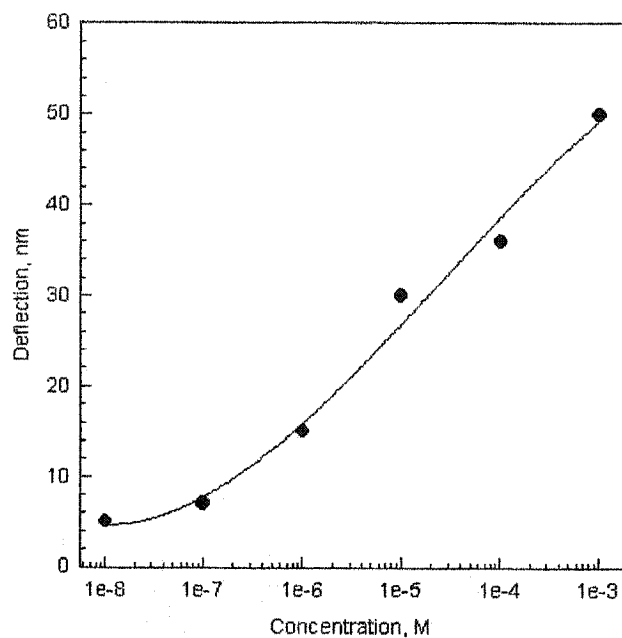


Figure 5-7 The deflection amplitude of a silicon cantilever
as a function of the concentration of HF.

## 5.4 Conclusion

Our results showed that molecular-level chemical reaction or etching can be converted into nanoscale micromechanical bending. Based on this concept, an $SiO_2$ cantilever can be used to selectively detect HF at a concentrations as low as $10^{-16}$ M because of the reaction of HF with $SiO_2$. The sensitivity for detection of HF using a simple $SiO_2$ cantilever was much higher than that of any current detection methods.

# CHAPTER SIX

# IMPULSE MONITORING USING

# A MICROCANTILEVER

## 6.1 Introduction

Cantilever modified with a monolayer of cystein and 11-mercaptoudecanoic acid were found sensitive to pulse in saline solutions. The quick down-and-up deflection of the microcantilever matched well the profile or pattern of the pulse generated in the system. The possible mechanism is the disruption and restoration of the electric double layer on the monolayer surface. A device constructed with such microcantilever sensors may be used for impulse monitoring.

Advances in the field of micro/nano-electro-mechanical systems (MEMS and NEMS) now offer unique opportunities in the design of ultrasensitive analytical methods. MEMS/NEMS have demonstrated their unique advantages when they are combined with chemistry and biology, including fast, real-time responses. In addition, MEMS and NEMS are small enough to be integrated into other devices. One of the most sophisticated and important MEMS/NEMS tasks is to develop an implanted or skin-attached chip with integrated wireless circuit that can transmit the signals to a remote receiver. A successful system would be an array of chips-base device that could monitor a person's body functions all at once, including pH, pulse rate, temperature, $pCD_2$, $pO_2$, $Na^+$, $Ca^{2+}$, etc.

93

Recording these vital physiological changes is critically important in the health care and combat field where a patient's vital signs must be constantly monitored. These devices could also provide valuable information on the physiological condition of high-risk outpatients, infants at risk of suffering sudden infant death syndrome, police, firefighting and construction personnel in hazardous situations, etc.

Microcantilevers have proven to be an outstanding platform for chemical and biological sensors. The unique characteristic of microcantilevers is their ability to undergo bending due to molecular adsorption or binding-induced changes in surface tension. This is achieved by confining the adsorption on one side of the cantilever. The key to microcantilever sensor developments is to choose appropriate coatings for identification of chemically specific species. One significant advantage of microcantilever based sensors is that they have excellent dynamic response in a small package, with the opportunity to have integration of micromechanical components with on-chip electronic circuitry. Integrated circuits of microcantilever-based chips have also developed for processing the data and transmitting it as radio signals to a remote receiver. Recently, we reported several microcantilever-based sensors for the detection of several physiological vital components detection, including pH, and Ca. These studies and other microcantilever sensor work have laid a ground for a possible implanted or skin-attached microcantilever-based chip that may obtain and send physiological information to an intelligent monitor.

In our previously experiments, we recognized that some microcantilevers (such as a monolayer of cysteine modified microcantilevers) were extremely sensitive to a disturbance of the tubing connected to the flow system where the microcantilever stays.

A gentle touch or squeeze of the tubing would disturb the deflection of the microcantilever. On the other hand, some other cantilevers (such as a nonmodified

cantilever or a cantilever covered by a monolayer of 1-dodecanethiol) were less sensitive to outside disturbance.

These experiments implied that some cantilevers may be used for the monitoring of pulse rate. In this chapter, we report the response of a monolayer of crystein covered cantilever to mimicked pulses. The cause of the microcantilever response is also discussed.

## 6.2 Experiment

We used commercially available silicon microcantilevers (Veeco Instruments, CA) in all of our experiments. The dimensions of the V-shaped microcantilevers were 180 μm in length, 25 μm in leg width, and 1 μm in thickness. One side of the cantilever was covered with a thin film of chromium (3nm) followed by a 20-nm layer of gold, both deposited by e-beam evaporation. The other side of the microcantilever was silicon with a thin naturally grown oxide layer.

The chemicals used in these experiments including cyteine, 11-mercaptoundecanoic acid, and 1-dodecanethiol were used as received for Aldrich. High-purity deionized water was obtained with a Milli-Q water system (Millipore). The $10^{-2}$M NaCl solutions used in our microcantilever deflection experiments were prepared in deionized water. The pH of all these solutions was $7.0 \pm 0.1$.

The formation of L-cystein SAM on the gold coated cantilever was conducted by immersing the cantilever into $10^{-3}$M solution of L-crystein in $10^{-2}$M sodium phosphate buffer (pH=5) for 2 hours. then rinsing with phosphate buffer three times. The formation of monolayers of other compounds was accomplished by immersing the cantilevers into $10^{-3}$ M solutions of various compounds in EtOH for 12 hours, followed by rinsing with EtOH.

The deflection experiments were performed in a flow-through glass cell (Digital Instruments, CA). The V-shaped microcantilever was immersed in the deionized water. Initially, water was circulated through the cell using a syringe pump. Schematic diagram of the apparatus used in this study was reported in Chapter 4 in this dissertation.
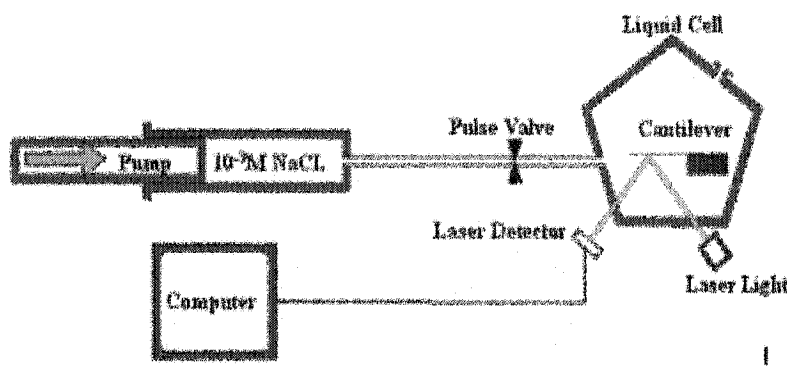


Figure 6-1 Experiment setup for impulse monitoring using microcantilever.

Microcantilever deflection measurements by the optical beam deflection method were carried out with an AFM photodiode. The bending of the cantilever was measured by monitoring the position of a laser beam reflected form the cantilever onto a four-quadrant photodiode. The cantilever was immersed in the electrolyte solution until a stable baseline was obtained and the voltage of the position-sensitive detector was set as background corresponding to 0nm.

A flow system was used to circulated a $10^{-2}$ M NaCl solution through the fluid cell that holds the cantilever. A constant flow (13.3mL/min) similar to that in a human body was driven by a syringe pump. The pulse similar to the impulse in the human body was mimicked by a flow control system (Burket product # 6013) at a frequency of 60 Hz. The fluid control system opens and closes a gate every 0.5 seconds cyclically. As a result of the gate opening and closing, a pulse was generated.

A microcantilever covered by a monolayer of cystein was initially exposed to a constant flow of the NaCl solution. When the flow control system was in function, the microcantilever bent down and up in one second as shown in Figure 6-2. The

microcantilever's reponse is fast and reliable, and the plot suggests that this microcantilever can used for monitoring the pulse rate. The maximum deflection amplitude can be used for monitoring the pulse rate. The maximum deflection amplitude of the cantilever was 0.9±0.3V with a standard errorness of 20% according to the data shown in Figure 6-2.
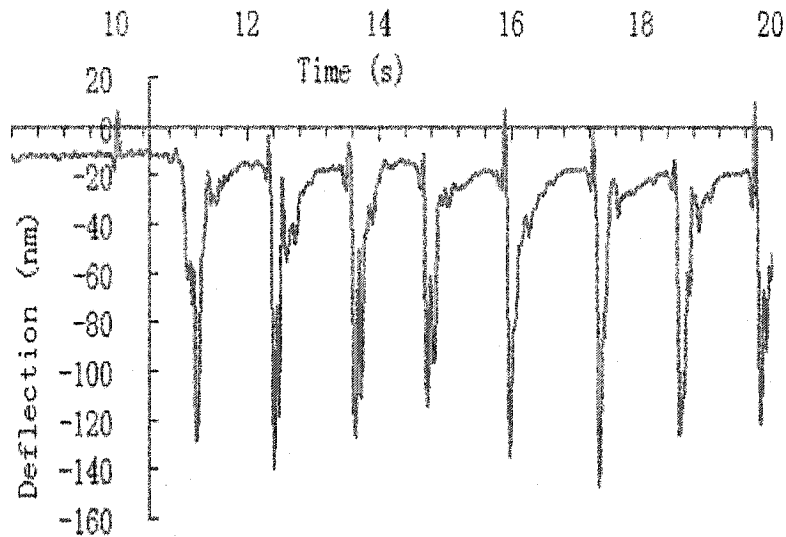


Figure 6-2 Modified microcantilever's responses to the mimicked impulse.



Figure 6-3 Unmodified microcantilever's response to the pulse
by the fluid control system.

## 6.3 Results and Discussion

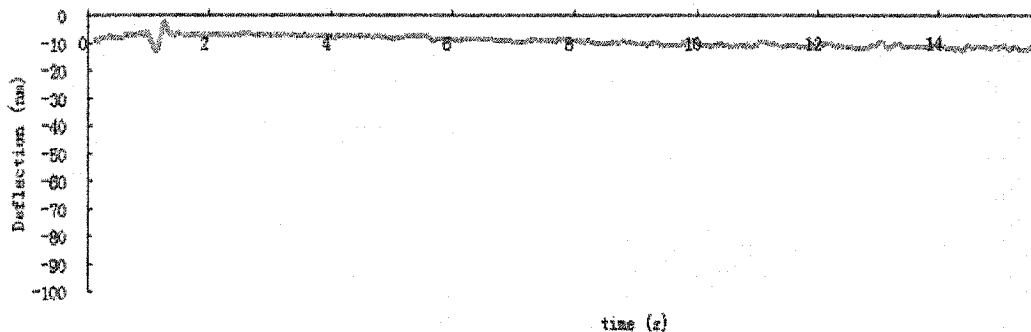Figure 6-2 also shows the response of an unmodified microcantilever to the pulse generated by the fluid control system. No significant deflection of the cantilever was observed. The small peaks in this figure was from instrument. The response of a

monolayer of 1-dodecanethiol covered microcantilever to the pulse was similar to that of an unmodified cantilever. Except for the flow rate change, all other solution conditions, including pH, ionic strength, and temperature, kept unchanged in these experiments. The difference between a monolayer of long chain 1-dodecanethiol compound and a monolayer of crysteine molecule is the surface charge. Since the isoelectric point of cysteine is 5.0, in the pH=7 environment, the COOH group of cysteine on the monolayer surface was in the form of COO⁻. On The contrary, there is no surface charge on the 1-dodecanethiol monolayer surface. Given this, the peak induced by the pulse was most likely due to the hydrodynamic disruption of the electric double layer on the microcantilever surface.

In a double layer, the counter-ions are influenced by two equal but opposing forces the electrical force attracting the positive ion to the negative COO⁻ surface, and the diffusive or thermal forces (responsible for Brownian motion) which tend to move the cations away from the surface. The balance between these two forces gives rise to distribution of cations in water adjacent to the cantilever surface. This distribution, described as a diffuse electrical double layer, could be distrupted by the flow rate change; i.e. the disruption of the double layer is proportional to the velocity of the flow. Since the double layer can be disrupted and restored quickly, the microcantilever bending is reversible and reproducible. The flow rate changes can convert electrical energy into mechanical energy. For the 90 nm deflection, the surface stress change was only 0.21 N/m.

$$\Delta Z = \left( \frac{3(1-v)L_2}{Et^2} \right) \delta s \qquad\qquad (6.3)$$

Where $\Delta Z$ is the observed deflection at the end of the cantilever, $v$ and $E$ are Poisson's ratio (0.2152) and Young's modulus (155.8GPa) for the silicon substrate, respectively, $t$ is

the thickness of the thickness (1 μm), L is the length of cantilever (180 μm), and δs is the differential stress on the cantilever.

The hypothesis of double layer disturbance is under investigation, and the detailed results will be published.

# CHAPTER SEVEN

# NEAR ZERO SURFACE ENERGY SUPER

# HYDROPHOBICITY OF PERFLUORO

# CARBON NANONEEDLE SURFACE

In the research of microcantilever sensor, surface modification by self-assembled monolayer (SAM) has prove to be a successful method for surface modification of microcantilever for sensing applications. In these microcantilever sensors, molecular recognition agents containing thiol compounds or silanes have been synthesized for the preparation of SAM on the microcantilever. In microcantilever sensing, the self-assembled monolayer (SAM) induces surface tension due to molecular adsorption which causes the bending of microcantilevers. In many cases, while one surface needs to be fully modified, another side surface needs to be kept integrated during the modification. These unbalanced surfaces maximize differential surface stress and enhances cantilever bending in chemical or biological sensing. Because the surface modification is normally proceeded in solution, microcantilever surface covered by stable hydrophobic film will keep integrated when micantilever is immersed into solution. In this research, superhydrophobic perfluorocarbon nanoneedle film was developed for this purpose.

100

Materials with nanometer-scale structures hold the promise of providing unique optical, electrical, magnetic or mechanical properties. While carbon, silicon, gold, and other metal or nonmetal materials are still emphasized, nanostructures made of polymer materials have drawn more and more attention. Polymer nano-composite materials are now created that include nanoclusters, nanofilms, nanorods, and networks of nanometer sized materials. Polymer nanostructures are normally synthesized using polymerization, self-assembly, and nanolithography methods. In our experiment, a blue-grayish coverage on the surface was developed (Figure 7-1). Scanning electron microscope (SEM) analysis revealed that this grayish material was made of a nanoneedle array (Figure 7-2). The SEM image of a sweep-broken nanoneedle laying on a surface is shown in Figure 7-3.
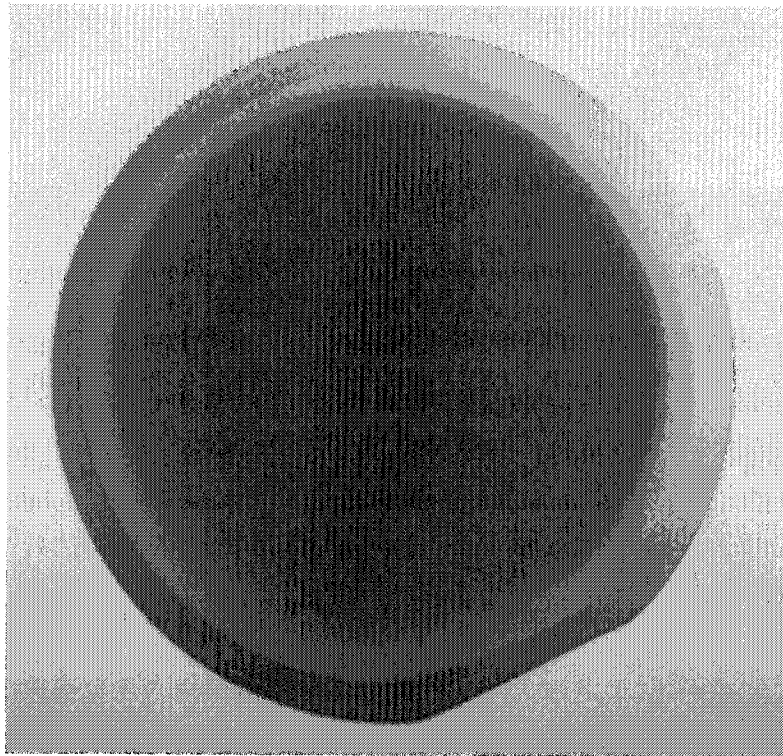


Figure 7-1 Macroscopic grayish coverage on wafer.
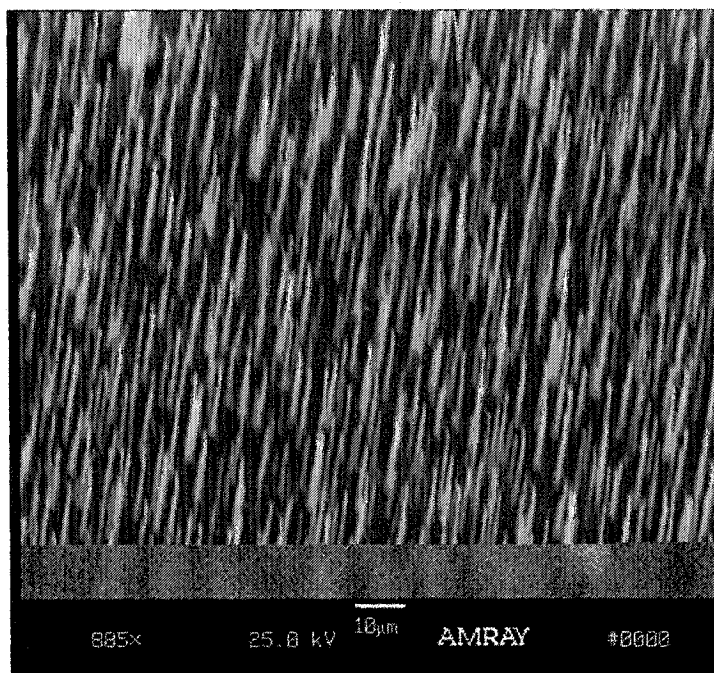
Figure 7-2 SEM image of nanoneedle array.



Figure 7-3 A SEM image of a laying nanoneedle
that was deliberately broken from the root.

X-ray photoelectron spectroscopy (XPS) (Figure7-4) and reflective IR show (Figure

7-5) that the nanofilament was composed of perfluorocarbon material, with a formula of

$(CF_2)_n$. These nanofilaments were fairly stable in air and did not react with 1M HCl and

1M KOH, respectively.
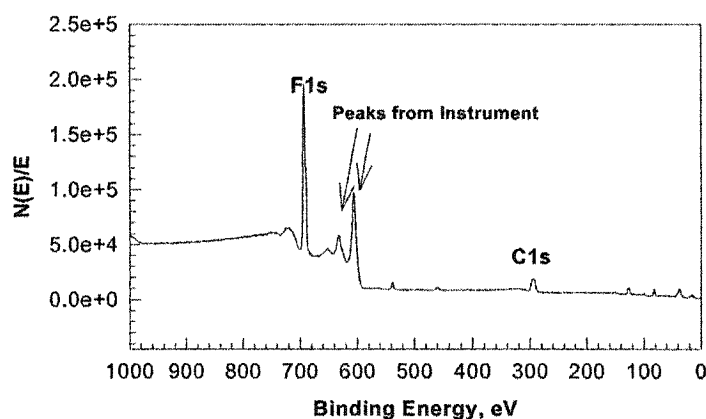
Figure 7-4 X-ray photoelectronic spectrum of nanoneedle array.

Figure 7-5. XPS spectrum of a nanofilament covered $SiO_2$ substrate. Atomic % of C and F is 29.04 and 70.95, respectively, in corresponding to $CF_2$ formula. The XPS spectrum was taken from X-ray photoelectron spectrometer Electronics 5802.
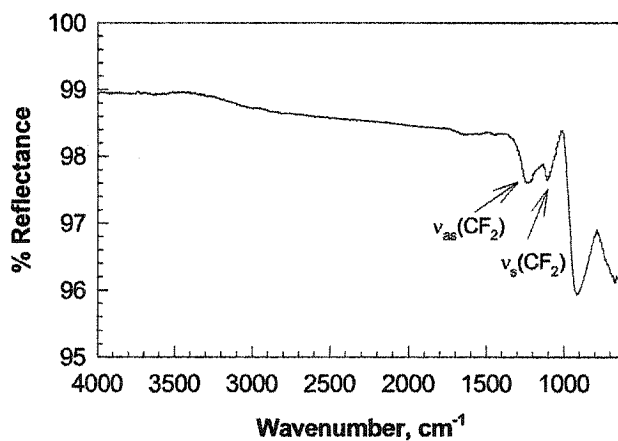


Figure 7-5 Reflectance FT-IR spectrum of perfluorocarbon nanofilaments.

No Si-OH stretching mode (3500cm-1) or Si-O-Si stretching modes (1060 cm$^{-1}$) were observed. The IR peaks were identified according to previous publications [12]. The IR was taken from Thermo Nicolet Nexus 470.

Water contact angle experiments of the nanofilament surface (Figure 7-6) unveiled a record-high water contact angle at 179.8 °, which is close to the maximum of 180°. The hyperhydrophic property of such nanofilament surface is caused from the large air-liquid contact area on the nanofilament surface and the natural hydrophobic property of perfluorocarbons.
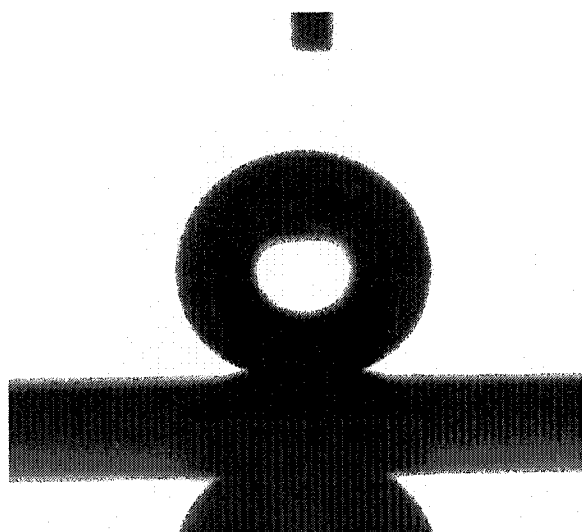
Figure 7-6 The profile of a water droplet on a nanoneedle surface.

The contact angle measurements were taken by OCA15 contact angle meter (Future Digital Scientific). The OCA software provided a pre-set ellipse fitting software for accurate contact angle calculation once the image was taken.

# CHAPTER EIGHT

# CONCLUSIONS AND FUTURE WORK

## 8.1 Conclusions

In this research, $SiO_2$ microcantilevers were successfully fabricated and characterized for chemical sensing. Due to its low spring constants, a $SiO_2$ microcantilever displays greater deflection and thus better sensitivity in chemical sensing compared to current commercially available microcantilevers. $SiO_2$ microcantilevers were also found to be an ideal HF sensor due to the chemically specific reaction between $SiO_2$ and HF. Microcantilevers made of other materials, such as SU-8 and piezoresistive materials were also fabricated. Microcantilevers were also used to monitor impulses for potential clinical and military applications. In addition to these cantilever studies, a perfluorocarbon nanoneedle array surface was developed. The surface has a hyperhydrophobic property with a record-high water contact angle of 179.8.°

## 8.2 Advantages and Future Works

Microcantilever biologic and chemical sensors have the following overwhelming advantages over other biologic and chemical sensors:

(1) Low cost and simple process;

(2) Low power;

(3) High sensitivity;

105

(4) High selectivity.

For a microcantilever sensor to be commercialized to practical applications, some future research work is needed:

• Piezoresistive and Piezoelectical Measurement of Microcantilever Bending.

Currently, microcantilever bending is measured by an optical method in the lab. To develop portable microcantilever sensor devices, more attention should be paid to piezoresistive and piezoelectrical measurement of microcantilever bending. This work involves proper microcantilever design and choosing suitable piezoresistive material. Preliminary work has been done in this disseration. Gold has been used as piezoresistive material. More work needs to be done to design proper piezoresistive microcantilever structures, and to employ doped silicon as piezoresistve material.

• New Material Cantilever and Calibration

Besides traditional microcantilever materials such as silicon and silicon nitride, other materials are developed to fabricate microcantilevers. In this research, polymer SU-8 has been used to fabricate microcantilevers. The SU-8 was calibrated so as to be used for chemical and biologic sensing. The polymer is an attractive candidate material for microcantilever fabrication for its ultra low Young's modulus and thus low spring constant. Much larger cantilever bending and higher sensitivity will occur in polymer microcantilevers.

• Implanted Chip in Human Body and New Structure Design

In addition, MEMS and NEMS are small enough to be integrated into other devices. One of the most sophisticated and important MEMS/NEMS tasks is to develop an implanted or skin-attached chip with an integrated wireless circuit that can transmit the signals to a remote receiver. A successful system would be an array of chips-based devices that could monitor a person's body functions all at once, including pH, pulse rate,

temperature, $pCO_2$, $pO_2$, $Na^+$ $Ca^{2+}$, and glucose. Monitoring these vital physiological changes is critically important in health care and the combat field where a patient's vital signs must be constantly checked. These devices could also provide valuable information on the physiological condition of high-risk outpatients, infants at risk of suffering sudden infant death syndrome, police, firefighting and construction personnel in hazardous situations.

# REFERENCES

1.  Chen, G. Y., *et al.*, Adsorption-unduced Surface Stress and Its Effects on Resonance Frequency of Microcantilevers, *Journal of Applied Physics,* 1995. 77, 3618-3622

2.  Tang, Y., Fang, J., Yan, X. and Ji, H.-F., "Fabrication and characterization of $SiO_2$ microcantilever for microsensor application", To be appeared in *Sensors and Actuators*

3.  Piner, R.D., et al., "Din-Pen" Nanolithography, *Science,* 1999, 283, 661-663

4.  Brugger, J., et al., Microfabricated Ultrasensive Piezoresistive Cantilevers for Torque Magnetometry, Sensors and Actuators, 1999, 73, 235-242

5.  Vecco Corporation

6.  Binning, G., et al., Atomic Resolution with Atomic Force Microscopy, *Phys. Rev. Lett.,,* 1986, 56, 930-933

7.  Binning, G., et al., Atomic Resolution with Atomic Force Microscope, Surface, 1987, 189-190, 1-6

8.  Watch, E. A.; Thundat, T., Micromechanical Sensors for Chemical and Physical Measurements, Rev. Sci. Instrum., 1995, 66, 3662-3667

9.  Jung, M. -Y.; Choi, S. S., Fabrication of Bimetallic Cantilevers and Its Characterization, Surface Review and Letters, 1999, Vol. 6, No. 6, 1195-1199

10. Barnes, J. R., *et al. Rev. Sci, Instrum,* 1994, 65, 3793-3798

11. Thundat, T.; Oden, P. I.; Warmack, R. J., Microcantilever Sensor, *Microscale Thermophysical Engineering,* 1997, 1, 185-199

12. Jensenius, H.; /thaysen, J.; Rasmussen, A. A., Veje, L. H.; Hansen, O.; Boisen, A., A Microcantilever-based Alcohol Vapor Sensor-Application and Response Model, Appl. Phys. Lett., 2000, 76, 2615-2617

13. Thundat, T.; Wachter, E. A.; Sharp, S. L.; Warmach, R. J., Detection of Mercury Vapor Using Resonating Cantilevers, Appl. Phys. Lett., 1995, 66, 1695-1697

14. Thundat, T.; Wachter, E. A.; Sharp, S. L.; Warmack, R. J., Detection of Mercury Vapor Using Resonating Cantilevers, Appl. Phys. Lett., 1995, 66, 1695-1697

15. Thundat, T.; Chen, G. Y.; Warmack, R. J.; Allison, D. P.; Wachter, E. A., Vapor Detection Using Resonating Microcantilevers, Annal. Chem., 1995, 67, 519-521

16. Baller, M. K.; et al. Ultramicroscopy 2000, 82, 1-9

17. Ji, H. –F.; Dabestani, R.; Finot, E.; Thundat, T.; Brown, G. M.; Britt, P. F., A Novel Self-Assembled Monolayer Coated Microcantilever for low Level Cesium Detection, chem.. Commun., 2000, 457-458

18. Hansen, K. M.; Ji, H. –F.; Wuy, G.; Datar, R.; Cote, R; Majumdar, A.; Thundat, T., Cantilever-based optical deflection assay for discrimination of DNA single nucleotide mismatches, Anal. Chem., 2001, 73, 1567-1571

19. Lang, H. P., et al., A Chemical Sensor Based on a Micromechanical Cantilever Array for the Identification of Gases and Vapor, Appl. Phys. A, 1998, 66, 61-64

20. Thundat, T.; Maya, L. Monitoring chemical and physical changes on sub-nanogram quantities of platinum dioxide. Surface Science (1999), 430(1-3), L546-L552.

21. T. Thundat, G. Y. Chen, R. J. Warmack, D. P. Allison, and E. A. Wachter, "Vapor Detection Using Resonating Microcantilevers," Anal. Chem. 1995, 67, 519-21

22. Porter, Timothy L.; Eastman, Michael P.; Macomber, Clay; Delinger, William G.; Zhine, Rosalie. An Embedded polymer piezoresistive microcantilever sensor. Ultramicroscopy (2003), 97(1-4), 365-369.

23. Fagan, B. C.; Tipple, C. A.; Xue, Z.; Sepaniak, M. J.; Datskos, P. G. Modification of micro-cantilever sensors with sol-gels to enhance performance and immobilize chemically selective phases. Talanta (2000), 53(3), 599-608.

24. Zhou, J.; Li, P.; Zhang, S.; Long, Y.; Zhou, F.; Huang, Y.; Yang, P.; Bao, M.. Zeolite modified microcantilever gas sensor for indoor air quality control. Sensors and Actuators, B: Chemical (2003), 94(3), 337-342.

25. Muralidharan, G.; Wig, A.; Pinnaduwage, L. A.; Hedden, D.; Thundat, T.; Lareau, Richard T. Adsorption-Desorption characteristics of explosive vapors investigated with microcantilevers. Ultramicroscopy (2003), 97(1-4), 433-439.

26. Pinnaduwage, L. A.; Gehl, A.; Hedden, D. L.; Muralidharan, G.; Thundat, T.; Lareau, R. T.; Sulchek, T.; Manning, L.; Rogers, B.; Jones, M.; Adams, J. D. Explosives: A microsensor for trinitrotoluene vapor. Nature (2003), 425(6957), 474

27. Ji, H.-F.; Dabestani, R.; Brown, G. M. and Britt, P. F. A novel self-assembled monolayer (SAM) coated microcantilever for low level caesium detection. Chemical Communications (Cambridge), 2000, (6), 457-458.

28. Ji, H.-F.; Thundat, T.; Dabestani, R.; Brown, G. M.; Britt, P. F. and Bonnesen, P. V. Ultrasensitive detection of $CrO_4^{2-}$ Using a microcantilever sensor. Analytical Chemistry 2001a, 73(7), 1572-1576.

29. Ji, H.-F. and Thundat, T. In situ detection of calcium ions with chemically modified micocantilevers Biosensors & Bioelectronics (2002), 17(4), 337-343.

30. Xu, X.; Thundat, T. G.; Brown, G. M; Ji, H.-F. Detection of $Hg^{2+}$ Using microcantilever sensors. Analytical Chemistry (2002), 74(15), 3611-5.

31. Butt, H.-J. A sensitive method to measure changes in the surface stress of solid, J. Colloid Interface Sci. 1996, 180, 251-260

32. McKendry, R.; Zhang, J.; Arntz, Y.; Strunz, T.; Hegner, M.; Lang, H. P.; Baller, M. K.; Certa, U.; Meyer, E.; Guntherodt, H. J. and Gerber, C. 2002. Multiple label-free biodetection and quantitative DNA-binding assays on a nanomechanical cantilever array. Proceedings of the National Academy of Sciences, 99(15), 9783-9788

33. Yan, X.; Tang, Y.; Ji, H.-F.; Lvov, Y. and Thundat, T. 2003a. Detection of organophosphates using an acetyl cholinesterase(AChE) coated microcantilever, Instrument Science & Technology, in press.

34. Sarid, D., Scanning Force Microscopy: with application to Electric, Magnetic and Atomic Force. Rev. ed., New York: Oxford University Press, 1994

35. Paz, M., Structure Dynamics, Theory and Computation. 4th ed. New York: Chapman & Hall; International Thomson Publishing, 1997

36. Rossow, E. C., Analysis and Behavior of Structure, Upper Saddle River, 1996, New Jersey; Prentice Hall.

37. Watcher, E. A.; Thundat, T., Micromechanical Sensors for Chemical and Physical Measurments, Rev. Sci. Instrum., 1995, 66, 3662-3667

38. Stoney, G. G. *Proc. Roy. Soc. (London)* **1909**, *82*, 172-177

39. Von Preissig, F. J., applicability of the classical curvature-stress relation for thin films on plate substrates, J. Appl. Phys., 1989, 66, 4264.

40. Adopted from the following URL
   http://www.ensc.sfu.ca/people/faculty/chapman/e495/e495l3j.pdf

41. Photos adapted from Bornside et al. J. Imaging Technology 13, 122, (1987)
42. J. Bhardwaj, H. Ashraf, A. McQuarrie Dry silicon etching for MEMS

43. S. M. SZE. VLSI Technology, Second edition

44. Saya, D., Fukushima, K., Toshiyoshi, H., Hashiguchi, G. Fujita, H., Kawakatsu, H. Fabrication of singule-crystal Si cantilever array

45. Tortonese, M., Kirk, M., "Characterization of application specific probe for SPMs", SPIE Vol.3009

46. Chatzandroulis, S., Tserepi, A., Goustouridis, D., Normand, P., Tsoukalas, D. 2002. Fabrication of single crystal Si cantilever using a dry release process and application in a capacitive-type humidity sensor. Microelectronic Engineering 61-62 (2002) 955-961

47. Farooqui, M., Evans, A. Silicon sensors with integral tips for atomic force microscopy: a novel single-mask fabrication process. J. Micromech. Microeng. 3 (1993) 8-12

48. Comella, B., Scanlon,M., The determination of the elastic modulus of microcantilever beams using atomic force microscopy. Materials Science 35 (2000) 567-572

49. Walters, D., Cleveland, J., Thomson,N., and Hansma, P., Short cantilevers for atomic force microscopy. Rev. Sci. Instrum. 67 (10), October 1996

50. Cho,I., Park, E., Hong, S., and Yoon, E., Atomic Force Microscope probe tips using heavily boron-doped silicon cantilevers realized in a <110> bulk silicon wafer. Jpn. J. Appl. Phys. Vol. 39 (2000) pp. 7103-7107

51. Jung, M., Kim, D., Choi, S., Kang, C. and Kuk, Y., Characterization of bimetallic cantilever for chemical sensor application. Jpn. J. Appl. Phys. Vol. 38 (1999) pp.6555-6557 Part 1, No. 11, November 1999

52. Itoh, T., Suga, T. Self-excited force-sensing microcantilevers with piezoelectric thin film for dynamic scanning force microscopy. Sensors and Actuators A 54 (1996) 477-481

53. Itoh, T., Suga, T. Force sensing microcantilever using sputtered zinc oxide thin film. Appl. Phys. Lett. 64 (1), 3 January 1994

54. Sones, C., Mailis, S., Apostolopoulos, V., Barry, I., Gawith, C., Smith, P., and Eason, R. Fabrication of piezoelectric microcantilevers in domain-engineered LiNbO$_3$ single crystals    J. Micromech. Microeng. 11(2002) 53-57

55. Datskos, P., Rajic, S., Senesac, L., Datskou, I. Fabrication of quantum well microcantilever photon detectors. Ultramicroscopy 86 (2001) 191-206

56. Mounaix, P., Delobelle, P., Melique, X., Bornier, L., Lippens, D. Micromachining and mechanical properties of GaInAs/InP microcantilevers

57. Harris, J., Awschalom, D. Fabrication and characterization of 100-nm-thick GaAs cantilevers. Rev. Sci. Instrum. 67 (10), October 1996

58. Grützmacher, D., David, C., Deckardt, E., Kirfel, O., Mentese, S., Ketterer, B., Golod, S., Wägli, P. Fabrication of SiGe/Si/Cr bent cantilevers based on self-rolling of epitaxial films. PSI scientific report, 2002, Vol.VII, Switzerland

59. Levy, R., Maaloum, M., Measuring the spring constant of atomic force miscroscope cantilevers: thermal fluctuations and other methods Nanotechnology 13 ( 2002) 33-37

60. Sader, J. Susceptibility of atomic force microscope cantilevers to lateral forces. Review of Scientific Instruments Vol.74 No.4

61. Passian, A., Warmack, R., Ferrell, T., and Thundat, T. Thermakl transpiration at the microscale: a crookes cantilever. Physical Review Letters Vo.90, No.12, Mar.28, 2003

62. Passian, A., Wig, A., Meriaudeau, F., Ferrell, T., and Thundat, T. Knudsen forces on microcantilever. Journal of Applied physics Vo.92 No.10

63. Hirai, Y., Mori, R., Kiruta, H., Kato, N., Inoue, K., and Tananka, Y. Resonance characteristics of microcantilever in liquid. Jpn. J. Appl. Phys. Vol.37 (1998) pp. 7064-7069 Part 1, No.12B, December 1998

64. Muralidharan, G., Mehta, A., Cherian, S., and Thundat, T. Analysis of amplification of thermal vibration of a microcantilever. Journal of Applied Physics Vol.89 No.8 Apr.15, 2001

65. Maekawa, S., Takashima, K., Shimojo, M., Higo, Y., Sugiur, S., Pfister, b. and Swain, M. Fatigue test of Ni-P amorphous alloy microcantilever beams. Jpn. J. Apppl. Phys. Vol.38 (1999) pp. 7194-7198

66. Ding, J., Meng, Y., Wen, S. Specimen size effect on mechanical properties of polysilicon microcantilever beams measured by deflection using a nanoindentor. Materials Science and Engineering B83 (2001) 42-47

67. Pressing, F. J. J. Appl. Phys. 1989, 66. 4262. (b) Muller, P. R.. Kern, R. Surf. Sci. 1994, 301, 386

68. J. E. Sader, Parallel beam approximation for V-shaped atomic force microscope cantilevers, Rev. Sci. Instr. 66 (1995) 4583-4587

69. Thin Solid Films, 283(1996), p.15

70. Most of the information can be found from EPA reports "Hazardous Air Pollutant Emissions from Electric Utility Steam Generating Units" on the internet at http://www.epa.gov/ttn/oarpg/t3rc.html

71. R. L. Vander Wal, B. E. Holmes, J. B. Jeffries, P. M. Danehy, R. L. Farrow, D. J. Rakestraw "Detection of hydrogen fluoride using infrared

72. R. L. Vander Wal, B. E. Holmes, J. B. Jeffries, P.M. Danehy, R.. L. Farrow, D. J. Rakestraw " Detection of hydrogen fluoride using infrared degenerate four-wave mixing" Chemical Physics Letters, 1992, 191, 251-258

73. D. Richter, A. Fried, G. Tyndall, E. Oteiza, M. Erdelyi, and F. K. Tittel, "All-Telecom Diode Laser Based Mid-IR Source for Spectroscopic Detection of HF, $H_2O$ and HDO", *Trends in Optics and Photonics*, 2002, 69

74. T. Ishiji "A study on the Amperometric Gas Sensor Using Electrolytic Solution" Chemical Sensors, 1999, 15, 56-64

75. R. Heger, A. Abbe, J. T. Pisano, and M. Frfanz "Intercomparision of Three Separate Technologies for the Measurement of HF Stack Emission from the HAW Primary Aluminum Smelter" *Light Metals*, 2000, *373-376*

76. J. W. Leonhardt " A new ppb-gas analyzer by means of GC-ion mobility spectrometry (GC-IMS)" *J. Radioanal. Nucl. Chem.* 2003, *257*, 133-139

77. Z. –M. Qi, K. Itoh, M. Murabayashi and N. Matsuda "Monitoring of interaction on the solid-liquid interface by use of composite optical waveguide polarimetric interferometers" *Chemical Sensors*, 2001, *17* (Supplement A), 76-78

78. S. E. Letant, M. J. Sailor "Detection of HF gas with a porous silicon interferometer" *Advanced Materials*, 2000, *12*, 355-359